



NERSC Technical Report no. 310

MONRUK SAR data analysis report

Monitoring the marine environment in Russia, Ukraine and Kazakhstan
using Synthetic Aperture Radar

A project supported by European Commission under FP6, Aeronautics and Space Programme
2005 - 2007


A report by Nansen Environmental and Remote Sensing Centre (NERSC) and Nansen International Environmental and Remote Sensing Center (NIERSC) with support from Marine Hydrophysical Institute (MHI), Centre for Earth Operative Remote Sensing (NTsOMZ) and Centre of Astrophysical Research (CAR)



Map of the study areas in MONRUK

Prepared by

S. Sandven, T. Hamre, M. Babiker, K. Kloster, M. Hansen, J. Wåhlin, V. Kudriavtsev, A. Myasoedov, V. Y. Alexandrov, V. V. Melentyev, N. Y. Zakhvatkina, A. O. Yarygina, A. A. Feoktistov, N. N. Novikova, P. V. Denisov, V. V. Malinovsky and L. Spivak

 <p>NERSC</p>	<p>Nansen Environmental and Remote Sensing Centre (NERSC) Thormøhlensgate 47 N-5006Bergen, Norway Phone: + 47 55 20 58 00 Fax: + 47 55 20 58 01 E-Mail: Stein.Sandven@nersc.no http://www.nersc.no</p>
---	--

<p>TITLE MONRUK SAR data analysis report Part 1: SAR analysis of open ocean Part 2: SAR analysis of sea ice</p>	<p>REPORT IDENTIFICATION NERSC Technical Report no. 310</p>
<p>CLIENT European Commission, FP6, Aeronautics and Space</p>	<p>CONTRACT Contract No. 031001</p>
<p>CLIENT REFERENCE Hartwig Bischof, E-mail: Hartwig.Bischoff@ec.europa.eu Space Research and Development DG Enterprise and Industry.</p>	<p>AVAILABILITY Public</p>
<p>INVESTIGATORS S. Sandven, T. Hamre, M. Babiker, K. Kloster, M. Hansen, and J. Wåhlin (NERSC) V. Kudriavtsev, A. Myasoedov, V.Y. Alexandrov, V. V. Melentyev, N.Y. Zakhvatkina, and A.O. Yarigina (NIERSC) A.A. Feoktistov, N.N. Novikova, and P.V. Denisov (NTs OMZ). V. V Malinovsky MHI) and L. Spivak (CAR)</p>	<p>AUTHORISATION Bergen, December 2009 Stein Sandven</p>

Contents

EXECUTIVE SUMMARY	4
PART 1: SAR ANALYSIS OF OPEN OCEAN	6
1. INTRODUCTION.....	6
2. BARENTS AND KARA SEAS: SAR OBSERVATIONS OF OCEAN FEATURES	7
2.1 MESO-SCALE CURRENTS.....	7
2.1.1 Coastal meandering current.....	7
2.1.2 Current temperature front.....	8
2.1.3 Open ocean eddies and meanders.....	10
2.1.4 Comparison of SAR analysis with ocean model output.....	12
2.1.5 Towards synergy of SAR and optical images.....	13
2.2 INTERNAL WAVES	14
2.2.1 Mapping of IW distribution	14
2.2.2 Analysis with use of RIM model.....	15
2.3 WIND SPEED FIELD OVER BARENTS SEA	17
3. SARTOOL: INSTRUMENT FOR SAR ANALYSIS WITH FOCUS ON OIL SPILLS	20
3.1 BLACK SEA	20
3.2 CASPIAN SEA	21
3.3 OTHER AREAS	23
3.3.1 Norwegian Sea	23
3.3.2 Head of Kinsale, Ireland	24
4. BLACK SEA: SAR MONITORING OF OIL SPILLS.....	25
5. CASPIAN SEA: SAR MONITORING OF OIL SPILLS.....	28
5.1 MONITORING STUDIES IN SUMMER 2007	28
5.1.1 Oil producing area near Apsheron.....	28
5.1.2 Southwestern part of Caspian sea water area	31
5.2 MONITORING STUDIES IN SUMMER 2008	33
5.3 RESULTS.....	35
6. RETRIEVAL OF SURFACE VELOCITY USING SAR DOPPLER SIGNAL.....	36
6.1 SYSTEMATIC DOPPLER MONITORING OF SEA AREAS	36
7. CONCLUSIONS	39
8. REFERENCES.....	40
PART 2: SAR DATA ANALYSIS OF SEA ICE.....	42
1. INTRODUCTION.....	42
2. ICE CLASSIFICATION/CONCENTRATION IN THE BARENTS AND KARA SEAS.....	44
2.1 EXPERT ANALYSIS AND INTERPRETATION OF SAR SEA ICE IMAGES	44
2.2 PRE-PROCESSING OF SAR IMAGES.....	46
2.3 SAR ICE CLASSIFICATION AND ICE CONCENTRATION - NEURAL NETWORK APPROACH.....	47
2.3.1 Algorithm description.....	47
2.3.2 Examples of sea ice classification.....	49
2.3.3 Status of the NN algorithm.....	51
2.4 SAR ICE CLASSIFICATION/MY-ICE CONCENTRATION - BAYESIAN APPROACH	51
2.4.1 Algorithm description.....	51
2.4.2 Examples of sea ice classification using Bayesian algorithm.....	52
2.4.3 Status of the algorithm.....	53

2.5 ICE DRIFT RETRIEVAL	54
2.5.1 Algorithms description	54
2.5.2 Examples of ice drift retrieval.....	55
2.5.3 Status of the algorithm.....	56
3. SEA ICE ANALYSIS IN STORFJORDEN.....	57
3.1 TIME SERIES OF SAR AND OPTICAL IMAGES.....	57
3.2 COMBINED ANALYSIS OF SAR, OPTICAL AND IR DATA.....	57
3.3 SEA ICE THICKNESS.....	60
4. ICEBERG DETECTION IN FRANZ JOSEPH LAND.....	62
4.1 INTRODUCTION	62
4.2 DATA AND METHODS	64
4.3 DATA ANALYSIS.....	65
4.4 ICEBERG DETECTION FROM TERRA SAR-X.....	65
5. SEA ICE MONITORING IN THE CASPIAN SEA	69
5.1 INTERPRETATION OF ENVISAT ASAR IMAGES.....	69
5.2 DETAILED ANALYSIS OF SEA ICE IN THE SAR IMAGE FROM 16 JANUARY 2006.....	70
5.3 COMPARISON OF SAR IMAGES AND SEA ICE CONCENTRATION MAPS	72
6. SUMMARY AND CONCLUSIONS	74
7. REFERENCES.....	75

EXECUTIVE SUMMARY

Part 1: SAR data analysis for open ocean

ENVISAT ASAR images for the three study areas, Barents and Kara Seas, Black Sea and Caspian Sea, are collected to investigate the most important oceanographic phenomena with use of existing and newly developed retrieval algorithms. ASAR data were received from the ESA rolling archive, stored at NERSC and NIERSC servers, and then distributed among the project partners. In most of the cases the set of ASAR images is analysed in combination with accompanying metocean data, supplemented with IR and optical satellite data, and data from oceanic numerical models. The main tools implemented for the SAR analysis is SARTool provided by BOOST Technologies and the Radar Imaging Model (RIM) developed at NIERSC.

The SAR studies the Barents and Kara seas were mainly focused on sub-mesoscale ocean currents and fronts, internal waves and wind field. The studies are motivated by the need to understand features such as convergence and divergence zones, fronts, eddies and internal waves. Fronts are potential accumulation zones of nutrients and therefore important for fishery. Internal waves and their energy is important for navy operations and ocean mixing processes. Monitoring of wind field with emphasis to polar lows is needed for better weather forecasting. The studies show that current features, fronts and internal waves can routinely be observed by SAR. These oceanic phenomena were classified, analyzed, mapped and interpreted with combine use of SARTool and RIM model. The SAR analysis were supplemented by output from the operational ocean current model HYCOM, as well as IR and optical satellite images. The supplementary information was important for interpretation of the observed SAR signatures.

The work in the Black and Caspian Sea study areas was focused on oil spill detection by SAR. The SARTool provided by BOOST Technologies was chosen as software for processing and analysis of the SAR data. A number of SAR images were processed in order to establish the quantitative level of pollution of the seas by oil spills, statistical parameters of observed oil spills events, and to establish the origin and sources of the oil spills. In total 258 oil spills events were revealed on 367 analyzed SAR images over the Black Sea. The spatial distribution of the spills showed that the most frequent occurrence of oil spills takes place along the main tanker routes, near offshore oil platform positions, and in the large ports. A map of oil spills distribution was produced, showing similar results to previous studies obtained in the ESA-IAF OSCSAR project (Sandven et al., 2006). In the Caspian sea, the main contribution to oil spills is not only industrial activities (oil platform, tankers and pipelines), but also from natural sources such as hydrocarbon leakage from griffons (natural hydrocarbon containers under a sea-bottom). The analysis of SAR images in the northern Caspian Sea is particular difficult in the coastal zones due to varying sea level and very complicated configuration of the coastline.

The retrieval of Doppler surface velocity from SAR data is new perspective approach that has been demonstrated in the project. The Doppler velocity field contains both wind-driven and wave generated surface motion. Surface current is an important oceanographic parameter which could be derived from the total velocity if wind dependence of the Doppler velocity is established (analogy to CMOD4).

Part 2: SAR data analysis for sea ice

A series of ENVISAT ASAR WS images, covering the western part of the Barents and Kara seas, including the Barents and Kara Seas in the period from autumn of 2007 until May 2009 have been analyzed and visually interpreted. The following procedures of ENVISAT ASAR image preliminary processing were elaborated in order to improve and simplify their visual interpretation: recalculation of the backscatter coefficient to pre-defined incidence angle and automated processing of SAR mosaics. A neural network algorithm of sea ice classification was developed and tested for the images over the Central Arctic. The algorithm of multiyear ice concentration retrieval consisted of sea ice classification using Bayesian approach, interactive delineation of zones of different partial concentration of multiyear ice and calculation of multiyear ice concentration within the boundaries of delineated areas. An algorithm of ice drift, based on cross-correlation technique, was developed and tested using a series of ENVISAT ASAR images.

As part of the Barents Sea studies, the polynya in Storfjorden, Svalbard, has been observed through several winter seasons using SAR images from ENVISAT. The images were downloaded from the ESA SAR archive, calibrated and transformed into a polar stereographic projection. Studies of the data sets showed that in 2007 a stable ice cover formed in mid February. In general over the season from January to June a southward ice movement is present, with a polynya forming on the west coast of Edgeøya and in the mouth of the strait between Spitsbergen and Barentsøya. The prevailing conditions in year 2008 were the same as in 2007 with a southward movement of ice, resulting in polynyas in the same areas with refreezing and southward transport of the new ice. The ice in Storfjorden was also studied by using MODIS SST data in 2008. A method for ice thickness retrieval using thermodynamic balance between air, snow cover, ice and ocean was tested. The SST data from MODIS were used as input to an algorithm calculating the thickness of thin (< 0.5 m) ice. This method was a useful supplement to the SAR analysis.

The capability of ENVISAT Alternating Polarization data (AP) to classify sea ice types was investigated. Preliminary results show that sea ice type classification can be improved by use of polarization data, but more studies are needed to establish which combination of co- and cross-polarization are optimal for specific ice types. ENVISAT AP and TerraSAR-X images were also studied for iceberg detection. Preliminary results show that the TerraSAR-X images have promising capability for detection of icebergs, at least in the Franz Josef Land area. Comparison between TerraSAR and ENVISAT AP images showed that the higher resolution provided by TerraSAR-X images can improve the detection of icebergs considerably.

Sea ice monitoring in the northern part of the Caspian Sea was conducted in 2007 and 2008 using ENVISAT ASAR images and SSM/I data. ASAR images were received from NIERSC and RADARSAT images were received from CAR. Selected images were analysed for detailed characterisation of the sea ice in the area.

Development of SAR ice monitoring methodology will be important activity under GMES in the coming years, as new SAR systems such as RADARSAT-2, CosmoSkymed, and Sentinel-1 will be available. The possibility to use SAR with different modes and resolution will improve the resolution and accuracy of sea ice and iceberg observations from satellites

PART 1: SAR ANALYSIS OF OPEN OCEAN

1. INTRODUCTION

The most recent state-of-the-art review of SAR observation of the marine environment is *Synthetic Aperture Radar Marine User's Manual*, (eds. Jackson and Apel) issued by NOAA, September 2004. Based on several decades of studies, it demonstrates the powerful capabilities of spaceborne SAR systems to observe and quantify a number of oceanographic, atmospheric boundary layer and sea ice processes.

Existing SAR system from ERS-2 (C-band, VV), RADARSAT-1 (C-band, HH) and ENVISAT (C-band, VV/HH/VH/HV) providing high resolution images have already demonstrated their capability to detect oil spills in many sea areas, as reported by e.g. Alpers and Espedal (2004). In addition to oil spills, there are many others surface features (such as current features, natural films, surface temperature patterns, rain cells) that provide similar radar signatures as oil, as shown by e.g. Beal et al., (1997) and Espedal (2001). Many studies have pointed out that the distinction between oil spills and their look-alikes can be done by means of synergetic analysis of radar images in different bands and polarizations. However, the access to such images has been very limited.

Most of the efforts to detect and classify oil spills in SAR images have focused on analysis of images only. This means that it is difficult to identify and classify real oil slicks from many types of natural slicks which can be very similar to oil slicks ("look-alikes"). Operational oil spill monitoring systems using SAR data have therefore a problem with identification of many false positives. Presently, little efforts have been devoted to study the physical properties of various slick types and how these properties have impact on the SAR signature. In two recent projects, OSCSAR and SIMP¹, there are efforts to investigate the physical processes responsible for generating slicks in SAR images. In MONRUK, further studies have been undertaken using air-sea interaction models and radar scattering models in combination with field experiments to improve the knowledge of the mechanisms responsible for slick signatures.

This report presents results of the second analyzed data set for open ocean studies using SAR. ENVISAT ASAR images for the three study areas, Barents and Kara Seas, Black Sea and Caspian Sea, were collected in order to investigate the most important oceanographic phenomena with use of existing and newly developed retrieval algorithms. ASAR data were received from the ESA rolling archive, stored at NERSC and NIERSC servers, and then distributed among the project partners. In most of the cases the set of ASAR images is analyzed in combination with accompanying metocean data, supplemented with IR and optical satellite data, and data from oceanic numerical models. The main tools implemented for the SAR analysis is SARTool provided by BOOST Technologies and the Radar Imaging Model (RIM) developed at NIERSC.

SARTool is software package to process SAR images from ERS, ENVISAT and RADARSAT for retrieval of oceanographic parameters: surface wind and waves, ship and oil spill detection. SARTool uses a number of auxiliary data files providing bathymetry, shoreline, wind data, SST, surface currents from models and others. It also contains a number of image processing and statistical tools. SARTool is developed by BOOST Technologies.

¹ SIMP: Slicks as Indicators for Marine Processes, INTAS contr. 03-51-4987 (<http://www.soton.ac.uk/iso/simp>)

NIERSC has recently developed an advanced Radar Imaging Model (RIM) which predicts background radar scattering from the sea surface at arbitrary atmospheric stratification, wind and wave conditions (including cases of limited fetch relevant to coastal zone and marginal ice/water region), as well as radar signature of current features, surface temperature fronts and natural slicks or oil spills (Kudryavtsev et al., 2005; Johannessen et al., 2005). This model has been used in the work for the Barents and Kara Seas.

2. BARENTS AND KARA SEAS: SAR OBSERVATIONS OF OCEAN FEATURES

ASAR data obtained from ESA rolling-archive were used for detection and analysis of the main geophysical parameters in the ice-free areas of the Barents and Kara Seas. The following geophysical parameters were investigated:

- Meso-scale current features (convergence/divergence zones and fronts);
- Internal waves;
- Oil slicks;
- Wind field;

The pre-processing and analysis of the SAR data, including retrieval of the geophysical parameters, were performed using the SARTool and the RIM model.

In this report we do not show results of SAR observations of oil slicks over the Barents Sea, because the sea is very clean. During 2007 we were able to detect “only” 22 slicks associated with oil spills on 230 analyzed images.

2.1 Meso-scale currents

Observation of meso-scale currents has several important practical applications, such as detection of eddies and fronts with zones of high biological productivity. By use of the RIM model (see e.g. Kudryavtsev et al., 2005; Johannessen et al., 2005) bright/dark linear features can be detected in the SAR images, These features are associated with convergent/divergent zones, which provide favorable conditions for fish accumulation. Thus, SAR monitoring of such of the zones has clear application for the fishery.

Monitoring of meso-scale current features in SAR images has been done by NIERSC quite regularly since summer 2007. In the period from June to October 2007 about 230 images were investigated and about 100 images were analyzed and processed. More than 300 examples of mesoscale features and phenomena (internal waves, current fronts, eddies, etc.) were detected, analyzed and classified. Approximately the similar amount of SAR images and the similar amount of dynamical features were detected and analyzed for the summer period 2008. Some examples of analysis are presented below.

2.1.1 Coastal meandering current

In Figure 2-1 an example of SAR signature of coastal current near the Kola Bay (14 October 2007) is shown. The total length of observed current feature is about 80 km. On this figure we can clearly identify sinus-like structure (meander) with alternating dark and bright parts what can be associated with convergence and divergence zones correspondingly.

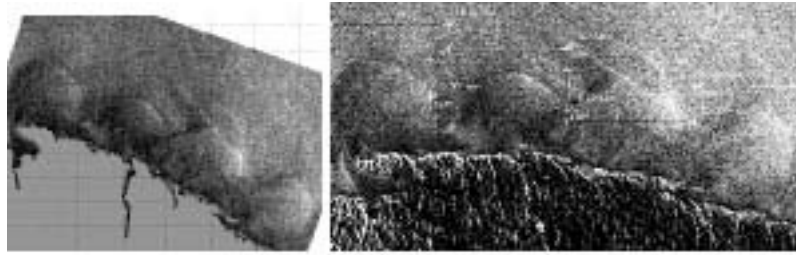


Figure 2-1 SAR signature of the coastal current with meanders and eddies near Kola Bay, observed in SAR image from 14 October 2007.

2.1.2 Current temperature front

The next example is taken from a long SAR stripe covering part of Franz Josef Land. A sub-image is extracted where the signature of a current front near the archipelago is visible (Figure 2-2).

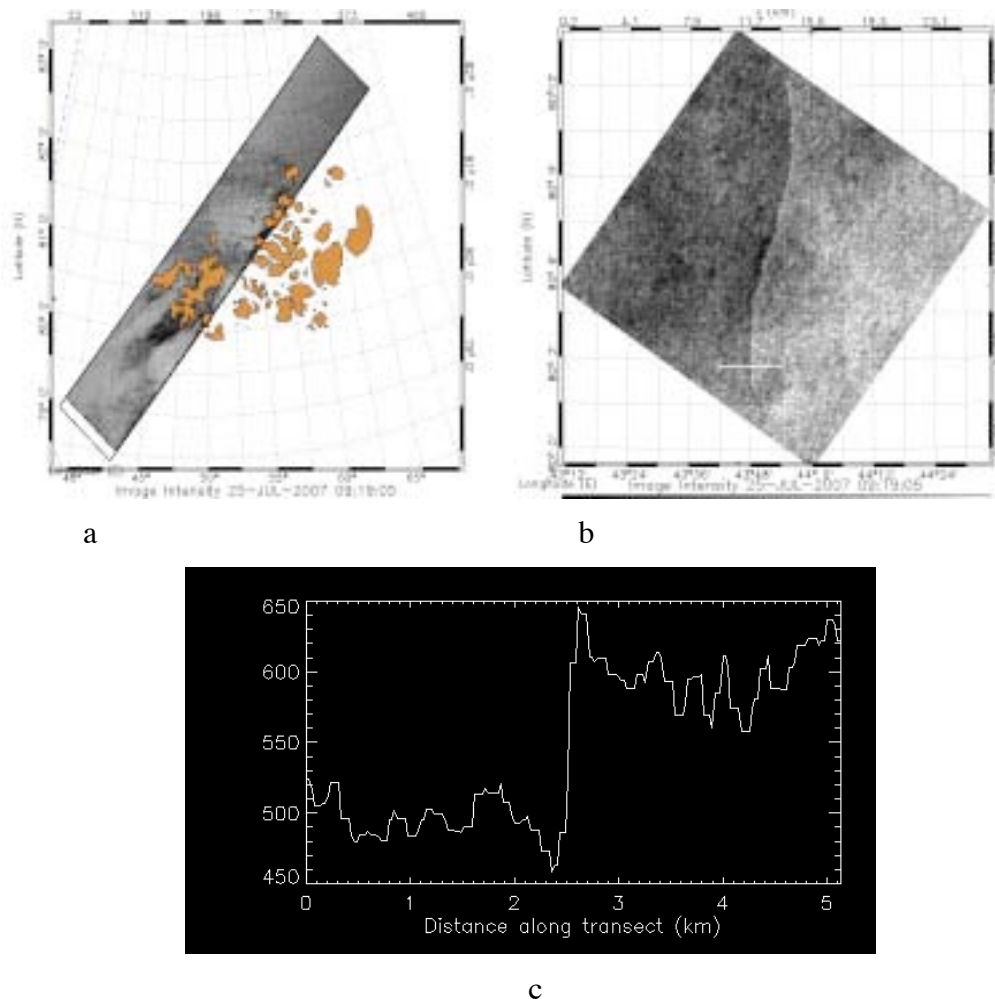


Figure 2-2. Current front near Franz Josef Land, observed on 25 July 2007. The lower graph is the backscatter (NRCS) profile across the front, indicated by the white line in (b).

The upper right plot shows subset of the ASAR image where the linear feature presumably corresponding to an oceanic temperature front is well expressed. The lower plot shows transect of SAR image (shown by line in the upper right plot). This transection shows the NRCS variations caused by wind field transformation due to the effect of atmospheric boundary layer stratification (Kudryavtsev et al., 2005). Left side of the transection corresponds to the cold side of the front and the right side is the warm side of the front.

Another example of a frontal zone observed in a SAR image close to Novaya Zemlya is shown in Figure 2-3.

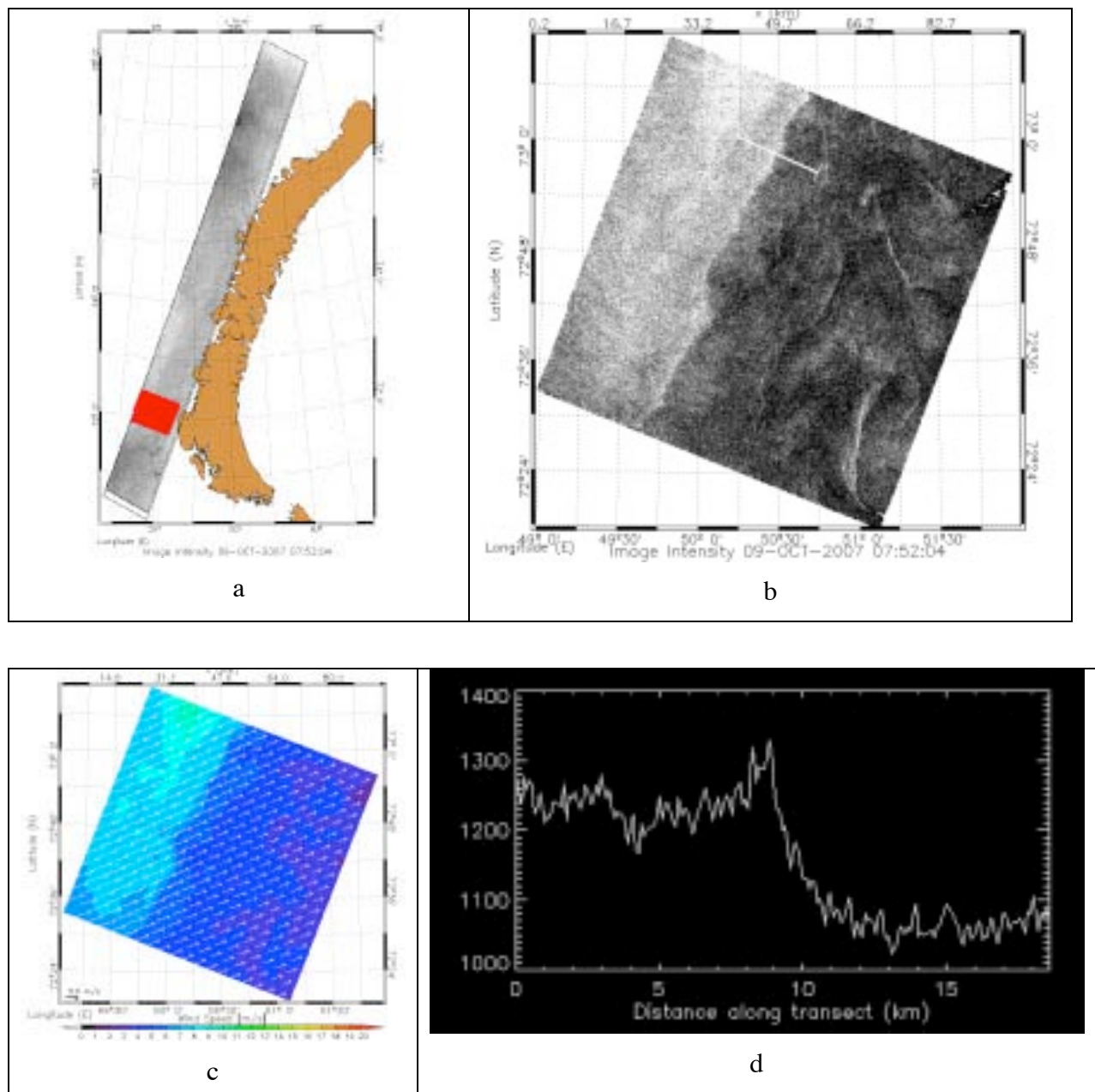


Figure 2-3 Frontal zone west of Novaya Zemlya observed in SAR image of 9 October 2007

The upper left image (a) is the full image stripe, where the red box shows the location the subimage analysed in (c) and (d). The upper right image (b) is a sub-image with frontal zone and transect in northern part. The lower left image (c) is the wind field retrieved by SARtool and in the lower right plot (d) is the NRCS profile across the profile. There is a strong gradient in the change of NRCS values across the frontal zone and wind speed values can explain the physics leading to this signature. As we know from the Barents Sea, present current maps in this area show strong frontal zone with warmer water masses from the left (northern branch of Northcape current coming from south) and colder water from the right (cold water masses from Arctic coming from north). The atmospheric stratification above warm water becomes unstable, leads to wind speed increase. Increased wind speed increases sea surface roughness that leading in turn to the stronger microwave backscatter (increased NRCS values in the NRCS profile graph). The opposite is found in the right part of the frontal zone. This physical scheme was predicted by RIM (see Kudryavtsev et al., 2005; Johannessen et al., 2005).

2.1.3 Open ocean eddies and meanders

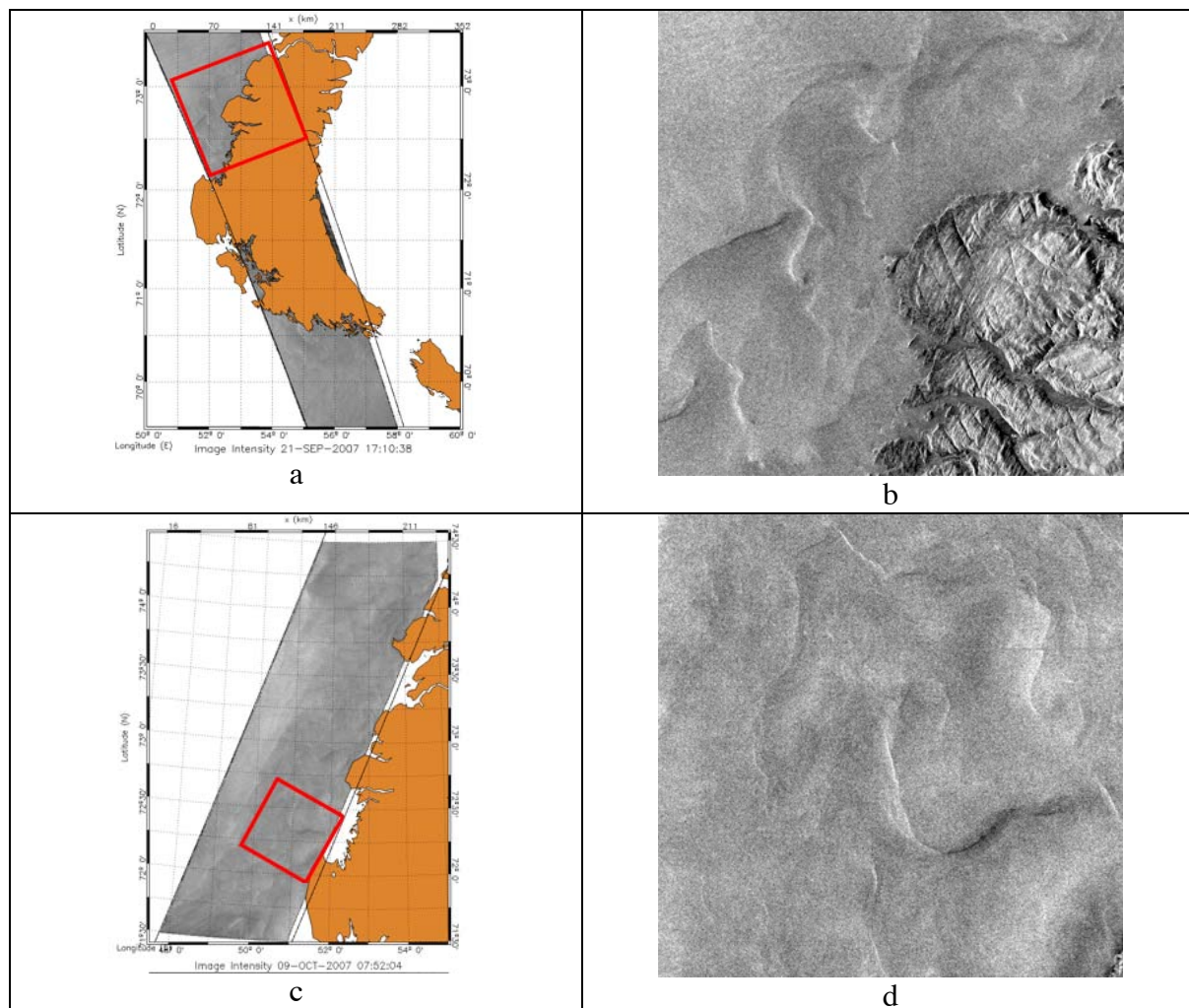


Figure 2-4. Current features' examples near Novaya Zemlya in Envisat ASAR images from 21 September 2007 (a and b) and 9 October 2007 (c and d).

Analysis of about 100 SAR images in the Barents and Kara Seas shows that manifestation of the open ocean eddies and meanders in SAR images occurs quite frequently. These SAR signatures have been classified and mapped as shown in Figure 2-4. We have also investigated the shape of some remarkable meandering current and eddy's features (diameter, characteristic length, etc. as shown in Figure 2-5.

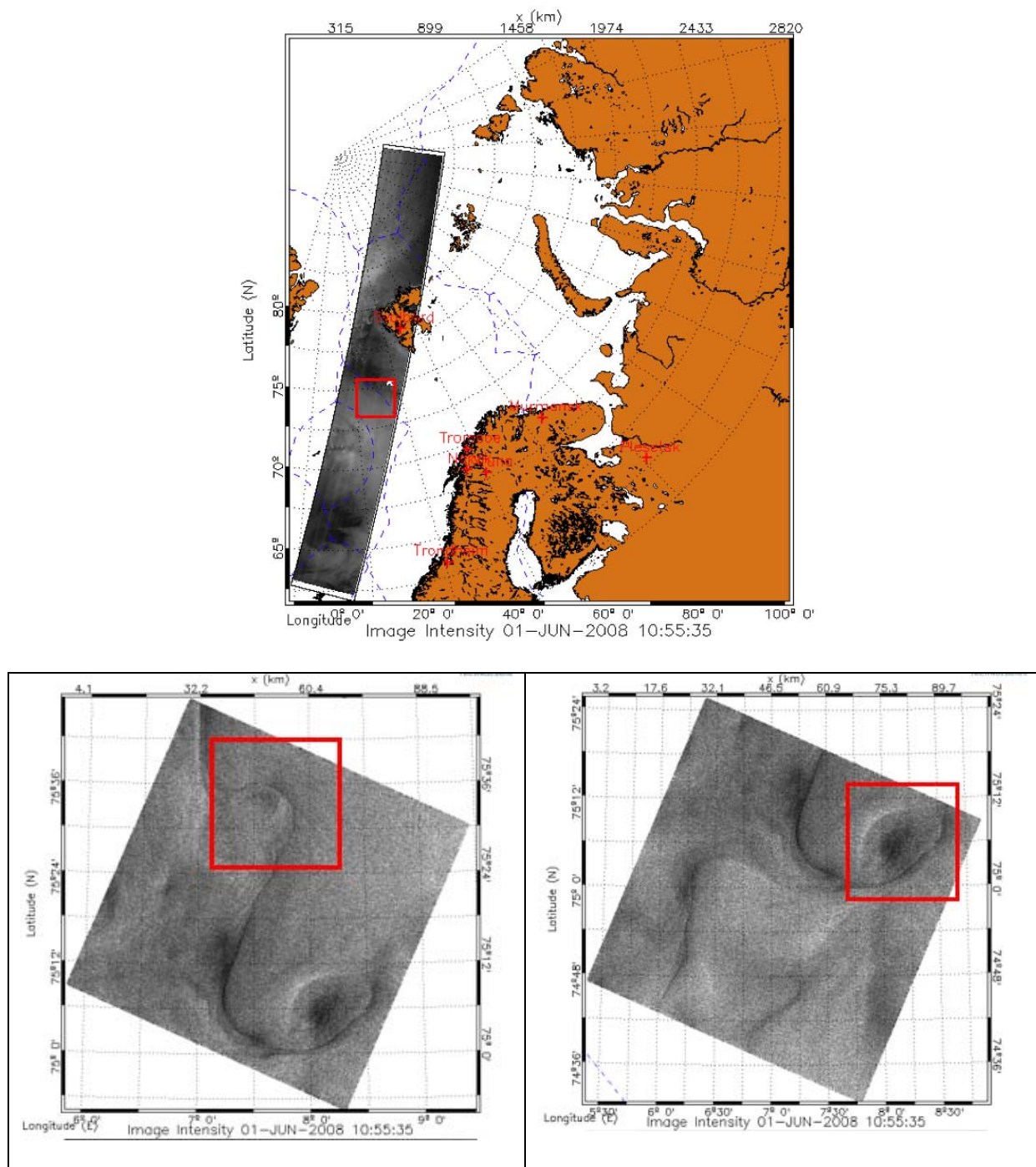


Figure 2-5. Example of eddies and meanders in Envisat ASAR image from 1 June 2008.

Figure 2-5 shows an example of meandering current signature observed to the south-west of Svalbard. A remarkable feature of this signature is that we can simultaneously observe two stages of meanders and eddies – meander itself (the lower left image) and eddy (the lower right image). The eddy's characteristic size is about 24×14 km and meander size is about 20×20 km, which corresponds to sub-meso-scales eddies.

2.1.4 Comparison of SAR analysis with ocean model output

In order to analyze and interpret SAR signature with use of RIM simulations one needs to specify surface current as input for the RIM model. An interesting example of a possible polar current front observed in an Envisat ASAR image from 4 January 2007 is shown in Fig. 2-6. The front is located in the Fram Strait outside the ice edge. The front extends several hundred km from south-west to north-east. The SAR analysis is compared to results of a high-resolution model simulation provided by NERSC. The tree upper graphs in Fig. 2.6 show the SAR image with front signature (left picture) and corresponding sea surface temperature (SST) from the model simulation (middle) and the Laplacian field of the SST field (right). The temperature front in model SST field is easily observed as the transition between warm water shown in red and cold water shown in blue in the middle. It demonstrates well-defined eddies and meanders. The Laplacian SST field from the model can be used for qualitative estimates of position of frontal features which are linked to current convergent or divergent zones.

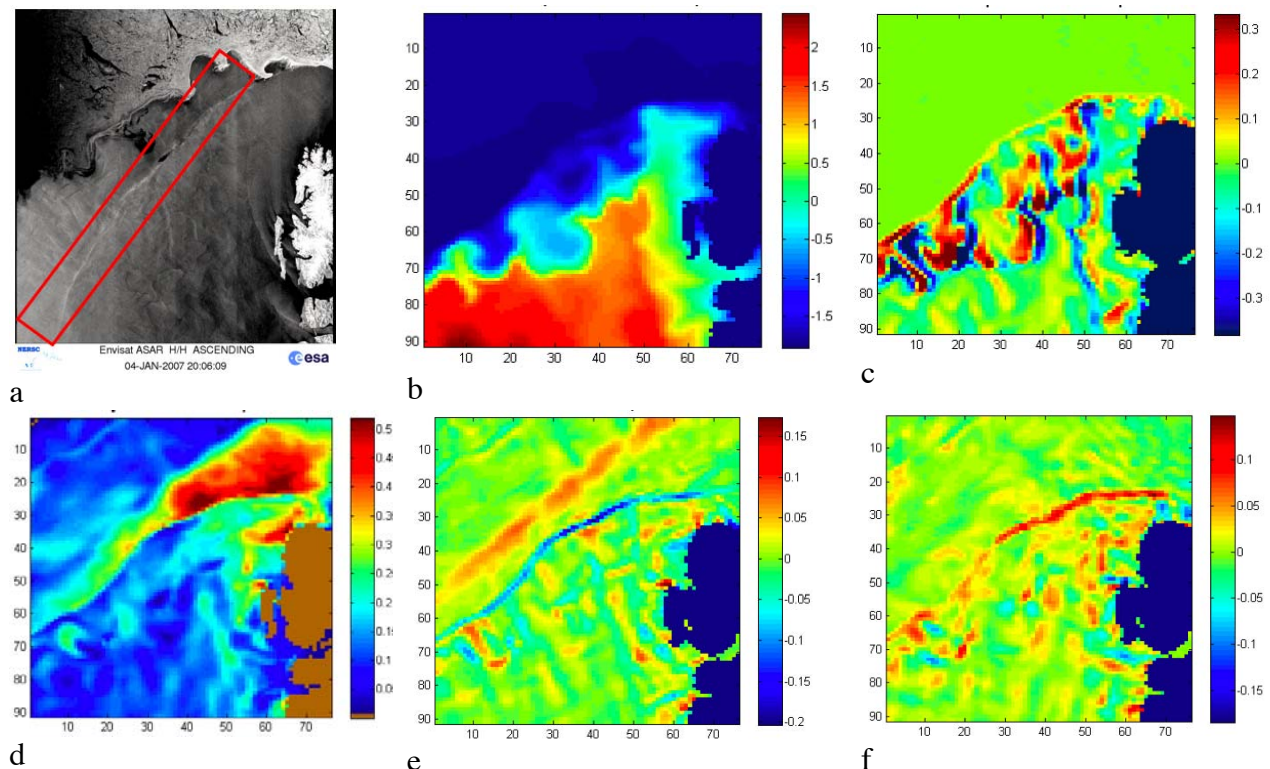


Figure 2-6. Polar front signatures on Envisat ASAR image from 4 January 2007 and coincident model simulation of current and temperature: (a) SAR image, (b) SST at 3 m depth from model, (c) SST Laplacian, (d) current speed at 3 m, (e) $\text{div}U$ at 3 m, and (f) vorticity field at 3 m.

The lower panel in Fig. 2-6 shows the model current speed (left), the velocity divergence field (middle) and the vorticity field (right) for the surface layer at mean depth of 3 m. There is a good correlation between the SAR signature of the front and the velocity parameters from the model, such as the divergence field (blue linear feature) and the vorticity field (red linear feature). Negative values of divergence means convergence of the surface current which, according to the RIM model, has to be manifested in SAR images as bright area (Kudryavtsev et al., 2005, Johannessen et al., 2005). The bright line feature in SAR image corresponds to convergence zone of the model current field.

2.1.5 Towards synergy of SAR and optical images

By combining SAR images and infrared (IR) images it is possible to obtain more information about processes at the sea surface. In the example below we have used a Landsat image taken on 16 August 2008 with 60 m spatial resolution and an ASAR Wide Swath image taken on 18 August 2008 with a resolution of 150 m. The results of the SAR and IR image comparison are shown in Figure 2-7.

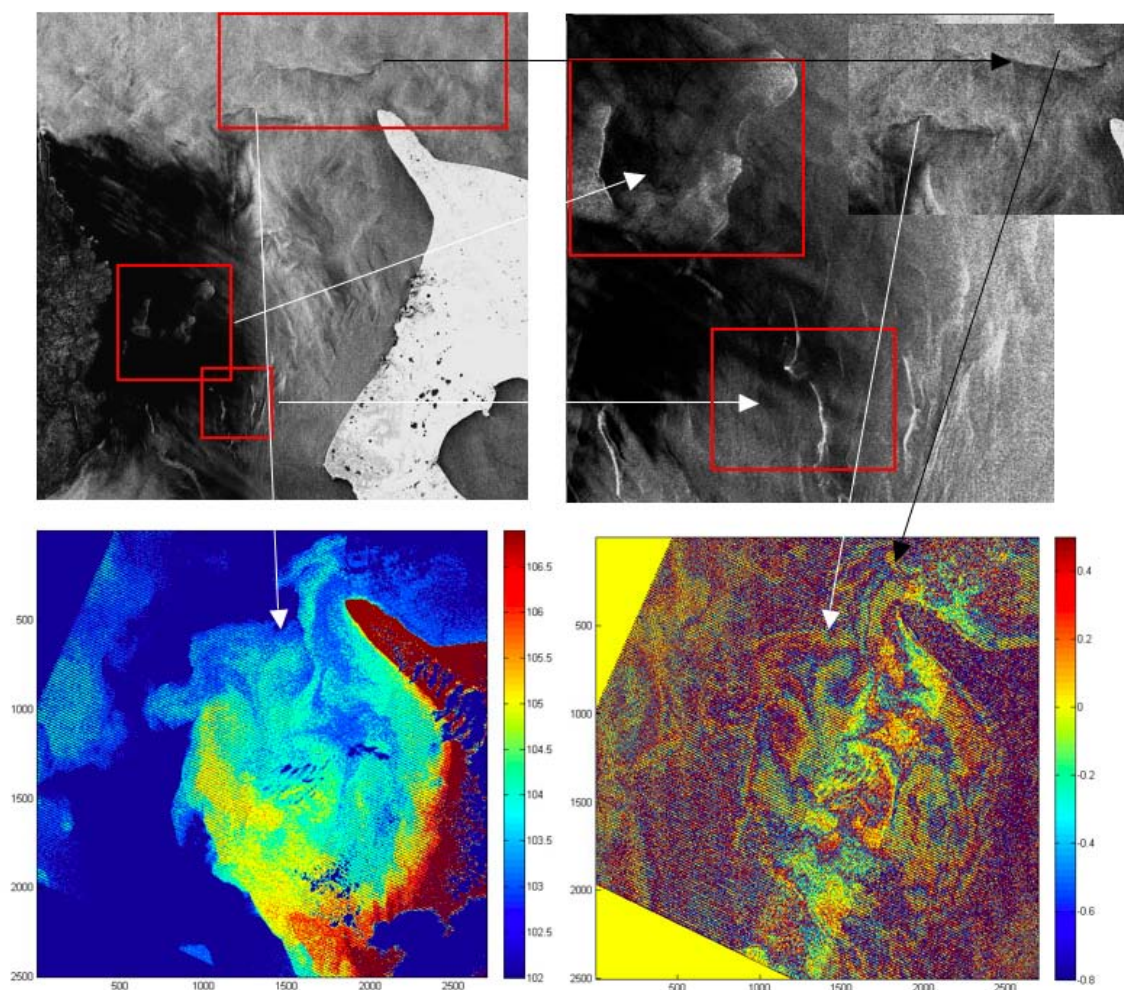


Figure 2-7. Mesoscale dynamics on Envisat ASAR image (upper pictures) and corresponding SST (bottom left) and SST Laplacian field (bottom right) fields.

The SAR image shows very complicated signature with fronts and meanders (the upper panel). The SST map (the bottom left picture) shows that temperature fronts are coinciding with SAR fronts caused by convergence or divergence in the current field. The SST Laplacian field (bottom right picture) presents a more detailed picture of the dynamic processes in this area. The Laplacian field shows several corresponding features between the SST field and the SAR image structure.

2.2 Internal waves

SAR observation of internal waves (IW) has important applications for studies of oceanographical processes and in practical operations of navy vessels. In the Barents Sea regular observations of IW has not been done and there are few publications available on the internal wave climate in the region.

2.2.1 Mapping of IW distribution

In this report we show internal wave observations for the summer period 2007 when 250 cases of IW events were registered. Figure 2-8 shows some examples of ASAR signatures of internal waves observed in the Franz Josef Land area, where most of the IW were found.

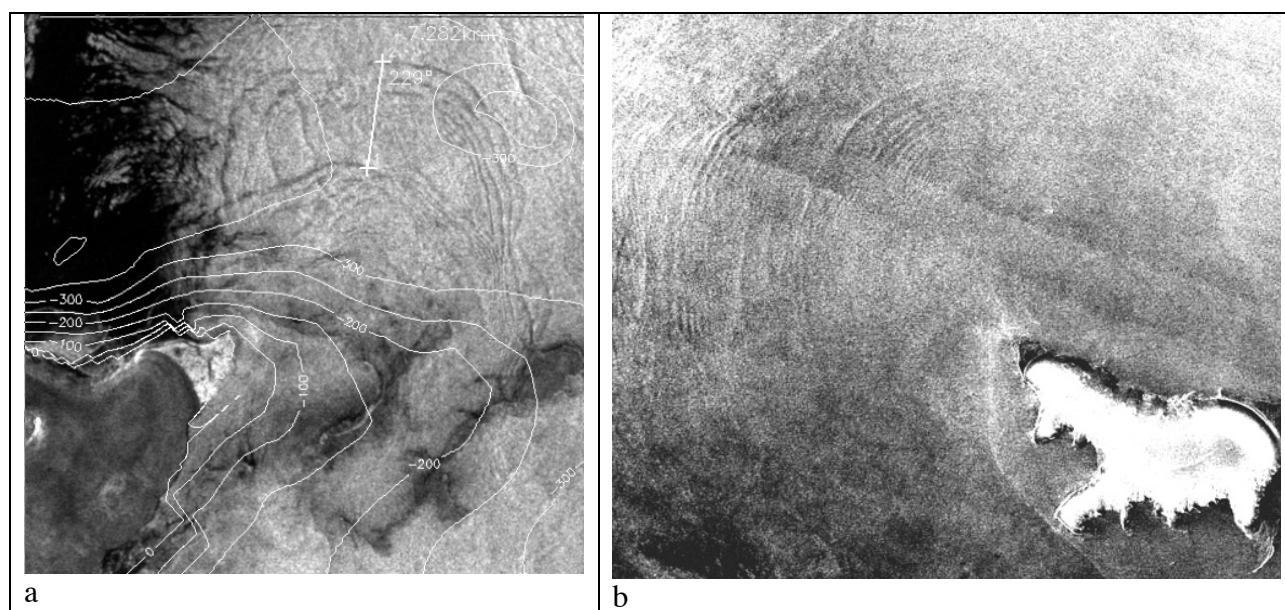


Figure 2-8. Examples of ASAR signatures of IW observed northwest of Franz Josef Land. The white line in (a) shows that repeated trains of IW are generated in the same location with 12 hours interval.

It was found that bottom topography features and tidal currents play an important role in generation of the internal waves. By superimposing isobaths from digital bathymetry database it was possible to correlate the generation of internal wave trains to changes in bottom depth, as shown in Fig. 8-2a. Analysis of the SAR images shows that internal wave trains are produced at 12 hours interval in specific locations. A 12 hour interval is near the period of the M2 tide which is a main tidal component in the Barents Sea.

A map of the location of the observed IW is shown in Figure 2-9. The geographical distribution of IW SAR signatures shows that there are specific generation zones for internal waves. The most dominant area was found to be north-west of Franz Josef Land. A total of 250 cases of IW signatures were found in 59 SAR images for period from June to August 2007.

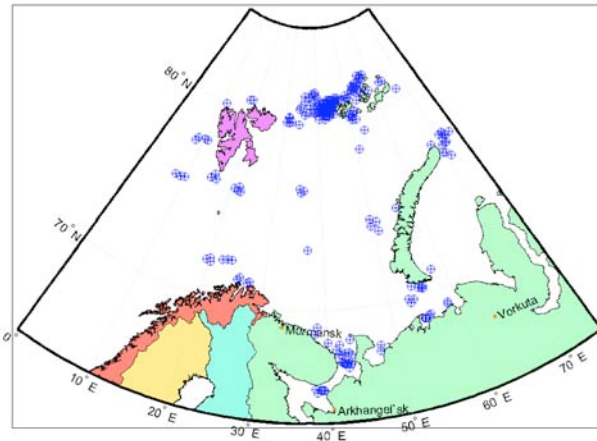


Figure 2-9. Map of location of IW trains observed by ASAR for the period from June to August 2007.

2.2.2 Analysis with use of RIM model

The RIM model was used to analyze internal waves observed in SAR images to the west of Franz Josef Land (Kozlov, 2008). In this region IW trains are imaged in wide variety of near-surface wind conditions and are assumed to be generated near the shelf-break at every tidal period. A subset of a SAR images from 16 September 2007 containing several IW train is shown in Figure 2-10.

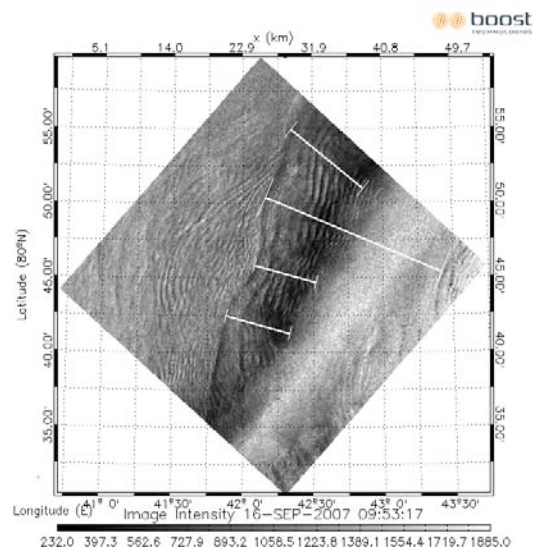


Figure 2-10. Several internal wave trains observed in the SAR image of 16 September 2007. The white lines mark the distance between repeated wave trains.

To understand the imaging mechanism of IW in the calm area observed IW signatures were compared with model calculations in the RIM. First, we obtained the main IW characteristics – wavelength in different parts of IW train, propagation direction and phase speed. The wavelengths in different parts of IW train were estimated using SARtool software. The IW phase speed was estimated by knowing a distance between two consequent IW trains propagating in the same direction and a tidal period. Geometry of SAR observations was specified from the images.

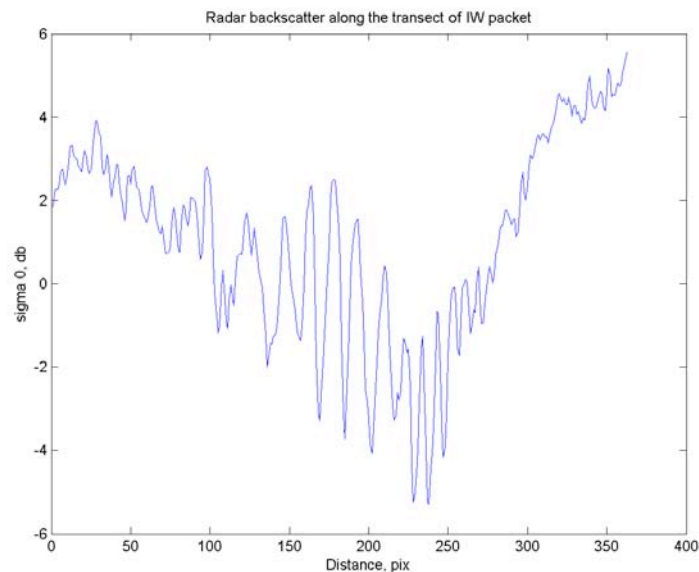


Figure 2-11. Cross-section of ASAR image in Figure 2-10. The distance of 400 pixels is equivalent to 3.5 kilometer

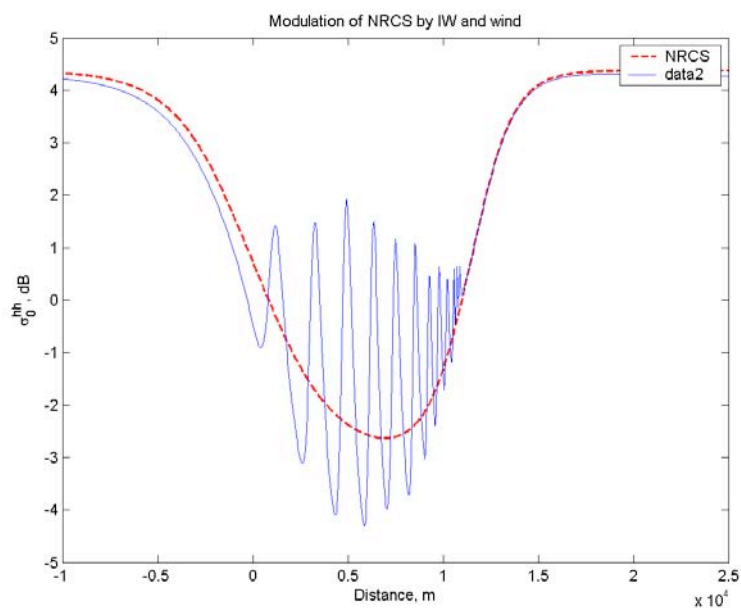


Figure 2-12. RIM simulated cross-section of ASAR signature of IW shown in Figure 2-11

Figure 2-11 shows observed SAR signature of IW train and its simulation by RIM model is presented in Figure 2-12. Comparing these figures one may conclude that RIM reproduces observation on a quantitative level, giving right NRCS contrasts caused by both mean wind speed variations and IW modulations of the sea roughness.

Figure 2-13 shows contribution of different scattering mechanisms to C-band SAR signatures of IW.

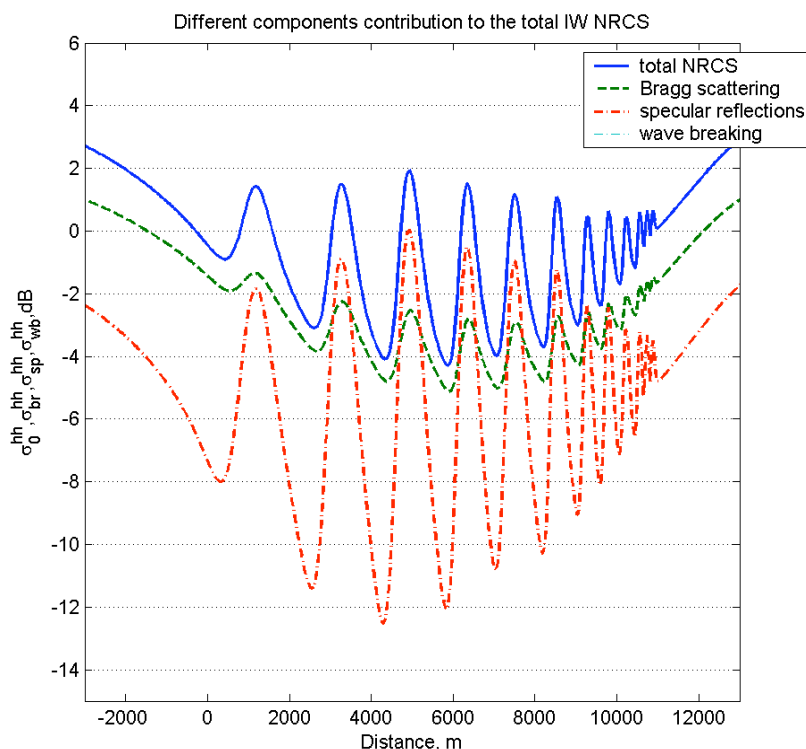


Figure 2-13. Modulation of the C-band NRCS: solid line is total NRCS, dashed line is contribution of Bragg waves and dashed-dotted line is contribution of specular reflection.

As can be seen, wave breaking contribution is so small, that even not shown in Fig. 2-13. The Bragg scattering contributes mainly to the background NRCS, i.e. its contribution decrease inside the calm area. On the other hand specular reflections give a small contribution to the background NRCS, while they significantly contribute inside the calm area. This can be explained as a result of a strong enhancement of mean square slope above IW troughs in calm area which result in dramatic increase of specular reflection of radar signal.

2.3 Wind Speed field over Barents Sea

Wind speed retrieval from ASAR images has been done on NIERSC server during the project. One of the main applications of this data is monitoring of wind patterns and events over the northern seas. Monitoring of extreme wind events (associated with polar lows) with use MONRUK facilities is now implemented in Russian federal programme “World Ocean”

focusing in particular on investigation of statistics of appearance of polar lows, their trajectories, and characteristics. In this section we describe the analysis method and illustrate some wind situations in the Svalbard area.

Wind speed is estimated from the calibrated quick-looks, which have a resolution of about 550 meters.

- The algorithm used is CMOD-4.
- Wind direction is taken from the 0.5 degree NCEP GFS model. These forecast data are available in near-real time from http://nomad3.ncep.noaa.gov/pub/gfs_master/. The GFS model is initialized at 0, 6, 12 and 18 UTC; the 00 or 03 hour forecast field, whichever is closest in time to the ASAR scene, is used as input to the CMOD-4 algorithm. Hence, the maximum timing difference between the ASAR σ^0 values and the wind direction is 1.5 hours.
- Ice mask is taken from AMSR-E products created and disseminated in near real time by the Institute of Environmental Physics, University of Bremen: http://iup.physik.uni-bremen.de:8084/amsrdata/asi_daygrid_swath/11a/n6250/. Ice concentration is given on a 6.25 km grid, although the sensor has a resolution of 12.5 km. An ice mask is created on the ASAR-scenes (wind product only) where the ice concentration is above 0%. The daily ice concentration is available the following day, so since most ASAR scenes are available within 3-10 hours, normally the ice mask from the previous day is used.

All the processing is done in near-real time mode on the server at NIERSC using rolling archives, and is available for project members. An example of the products processing is shown in Figs 2-14 and 2-15.

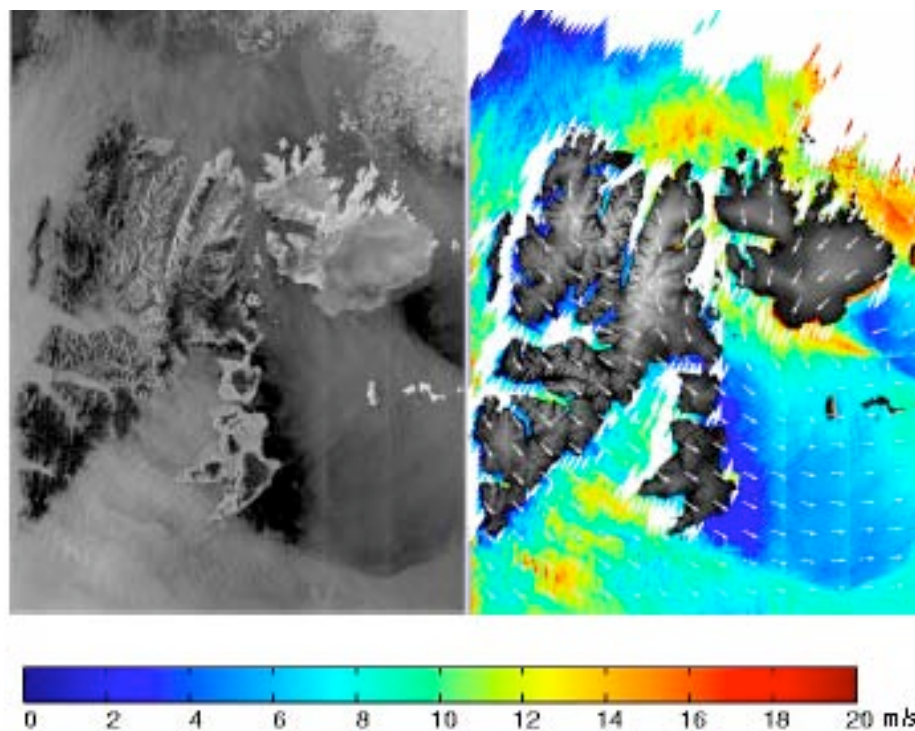


Figure 2-14. Left: Envisat ASAR WSM quicklook from 20 August 2007 covering the Svalbard area. Right: Wind speed retrieved from the SAR image using CMOD-4. The wind pattern is westerly. The sea ice cover is masked by white using passive microwave data.

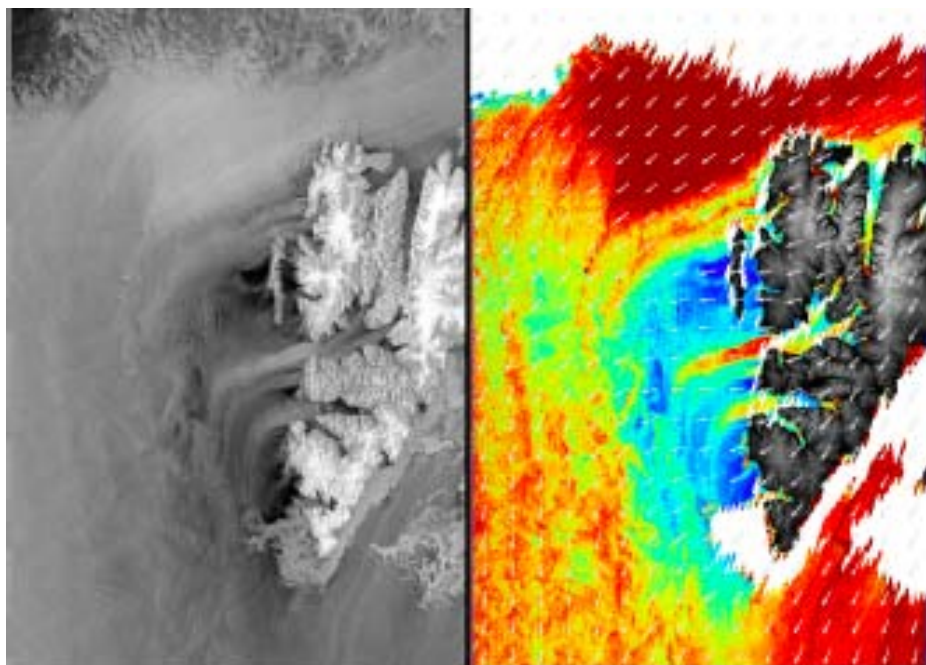


Figure 2-15. Left: Envisat ASAR WSM quicklook from 31 January 2008 covering the Svalbard area. Right: Wind speed retrieved from the SAR image using CMOD-4. The wind pattern is northeasterly with characteristic jet winds out of the fjords on the western side of Svalbard.

3. SARTOOL: INSTRUMENT FOR SAR ANALYSIS WITH FOCUS ON OIL SPILLS

SARTool is a software tool to read and process SAR images from Envisat, ERS and Radarsat for oceanographic applications such as surface wind and waves, ship and oil spill detection. SARTool uses a number of auxiliary data files providing bathymetry, shoreline, wind data, SST, surface currents from models and others. It also contains a number of image processing and statistical tools. The tool is used for research and analysis purposes. It enables to quickly produce outputs on marine applications. This IDL-based user-friendly software integrates a GUI which enables to read, visualize and process any type of path-oriented SAR images. The SARTool provided by BOOST Technologies has been distributed and installed among the MONRUK partners. The SARTool has been used for retrieval of surface wind and for identification of surface slicks that include potential oil spills.

Surface slicks, such as biogenic films and oil spills, cause a dampening of surface waves seen by the radar instrument, resulting in a decrease in backscatter. These characteristic dark features in SAR images allow detection and mapping of potential oil spills. However, dampening of small wave visible by the SAR instrument may also arise due to various effects leading to ambiguous slick detection such as low wind conditions. In such cases multi-sensor merging is required to refine the analysis and reduces the probability of false oil spill detection.

When a potential oil pollution area is detected, SARTool can be used to identify current dynamic features in SAR images. In addition currents from numerical models (see surface currents), can be used to predict the drift of an oil spill. In this report, several examples of oil spill detection from different areas are presented, where SARTool has been used to analyze the images.

3.1 *Black Sea*

An example of a SAR image with oil spill in the western Black Sea is presented in Fig. 3-1. Three potential oil spills were detected with the SARTool. The oil spill is also visible in a Landsat image obtained on the same day as the SAR image. An oil spill shape file produced in the SARTool is projected and opened on the top of the image in ArcGIS. Then the oil spill parameters are calculated and presented as shown in Table 3-1.

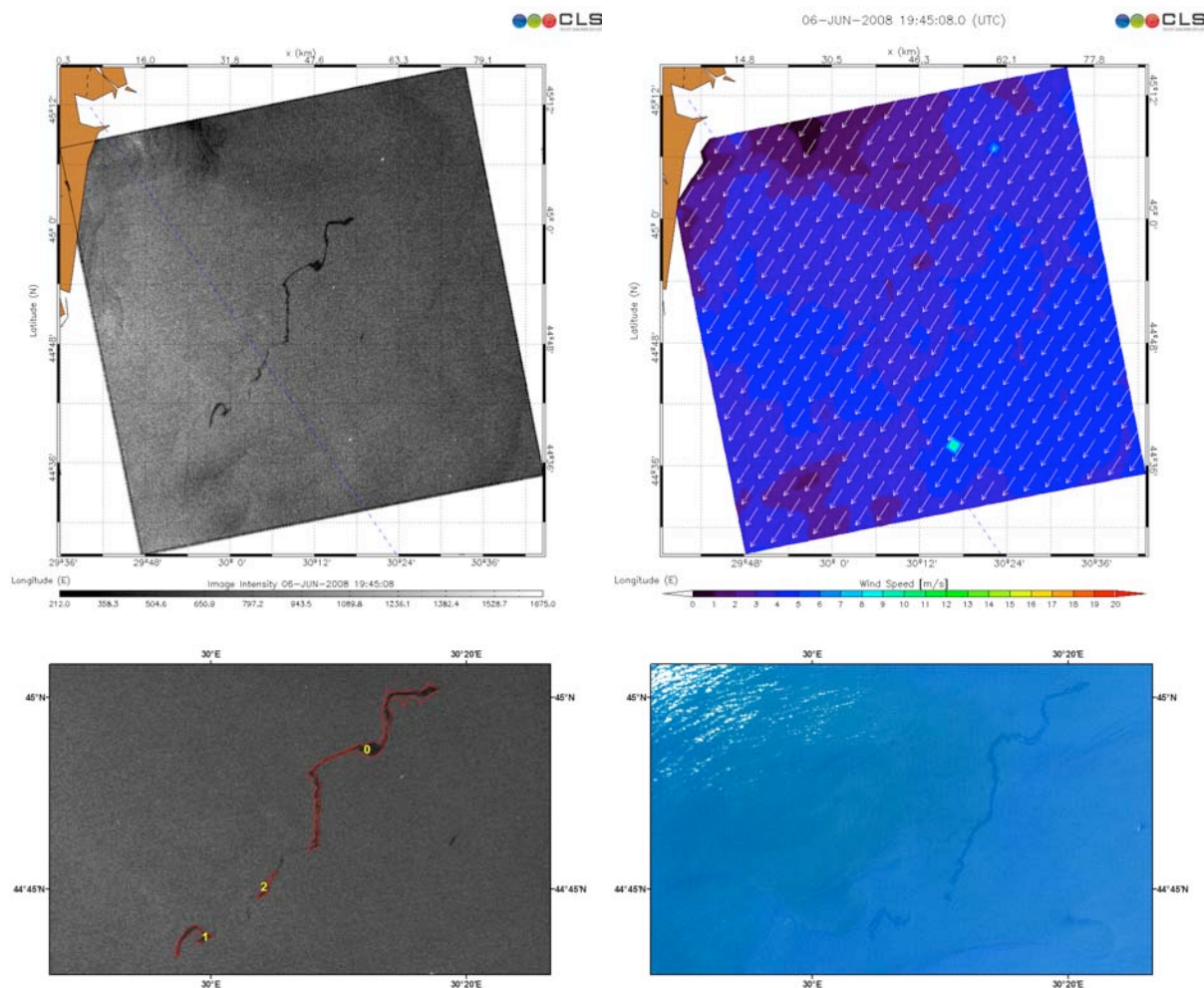


Figure 3-1. The upper left panel is a ASAR wide swath image covering the western part of the Black Sea on 06 June 2008. The upper right panel shows wind speed and direction produced from the SAR image. The lower left subset image showing the detected oil spills marked by red. The lower right panel is a subset of a Landsat image covering the same area and on the same date showing the same oil spills as dark features.

Table 3-1 Parameters of the oil spill presented on figure 3-1

Oil spill area	Wind	Length	Perimeter	Area	Complexity	Contrast	PMR	B Gradient	Mean Out	PMR2	Spread	Slendernes	direction
0	6,14	27,28	85,46	24,43	23,79	1,47	0,26	685,97	759,51	0,12	707,97	661,87	85,65
2	5,36	5,25	18,55	4,82	5,68	1,52	0,23	917,47	904,07	0,13	95,65	39,22	69,64
1	5,36	4,47	11,15	2,18	4,54	1,39	0,17	880,32	838,54	0,13	49,82	46,81	96,45

3.2 Caspian Sea

In many cases the analysis of a SAR image can be very complicated, and use of the SARTool to detect the oil spills can difficult, especially when the wind speed is low. An example from

the southern part of the Caspian Sea is presented in Fig. 3-2 where the wind speed is from 0 – 2 m/s. By using the algorithm for oil spill detection, many objects can be detected, depending on the setting of the detection parameters. The low wind speed causes many dark areas to be detected by the SARTool, but these are not oil spills, and even if oil spills are present they will be hard to detect. Most of the features in the SAR image are dark stripes depicting the current patterns such as eddies and meanders.

A Landsat optical image covering the same area on 20 July 2007 has been obtained, showing similar features as in the SAR image, where dark stripes depict current patterns. In addition, the Landsat optical image identifies water masses with different colours, such as sediments in river runoff. (Figure 3-3).

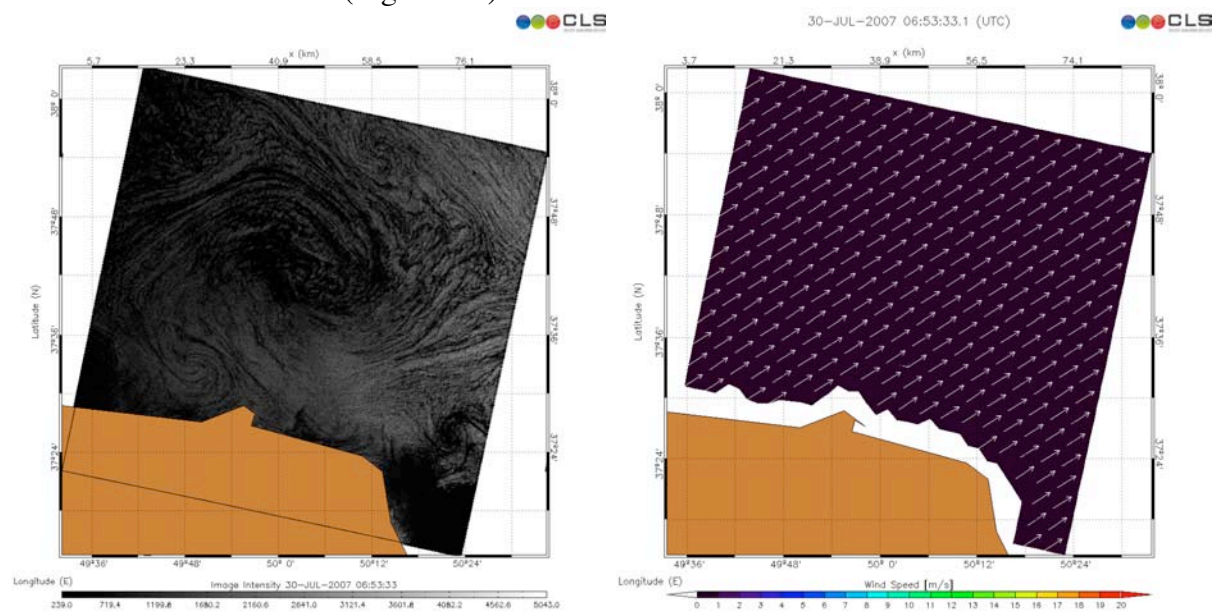


Figure 3-2. Left: ASAR image covering the southern part of the Caspian Sea: Right panel: wind speed produced from the left image, showing speeds below 2 m/s. .

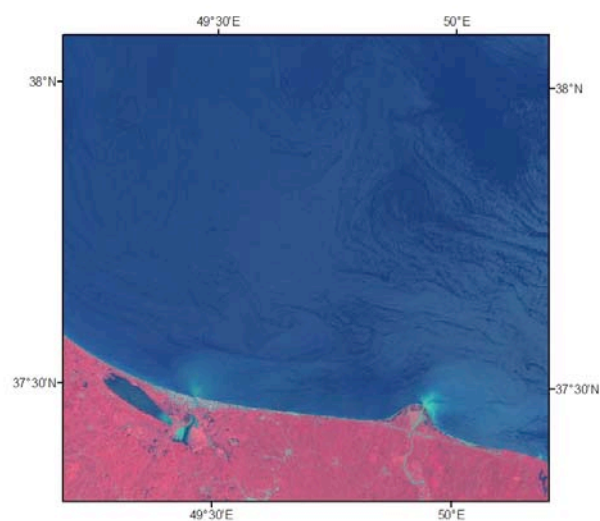


Figure 3-3. Landsat image covering the same area in the southern Caspian Sea.

3.3 Other areas

3.3.1 Norwegian Sea

An example of oil spill detection in the Norwegian Sea is shown in Fig 3-4. The spills are most probably released by ships leaving a long stripe of pollution. The stripe is spread by wind and currents, indicated by the curved nature of the stripes. In this case the SARTool identified 9 objects as oil spills. When these objects are joined together, they cover the two dark stripes in the image.

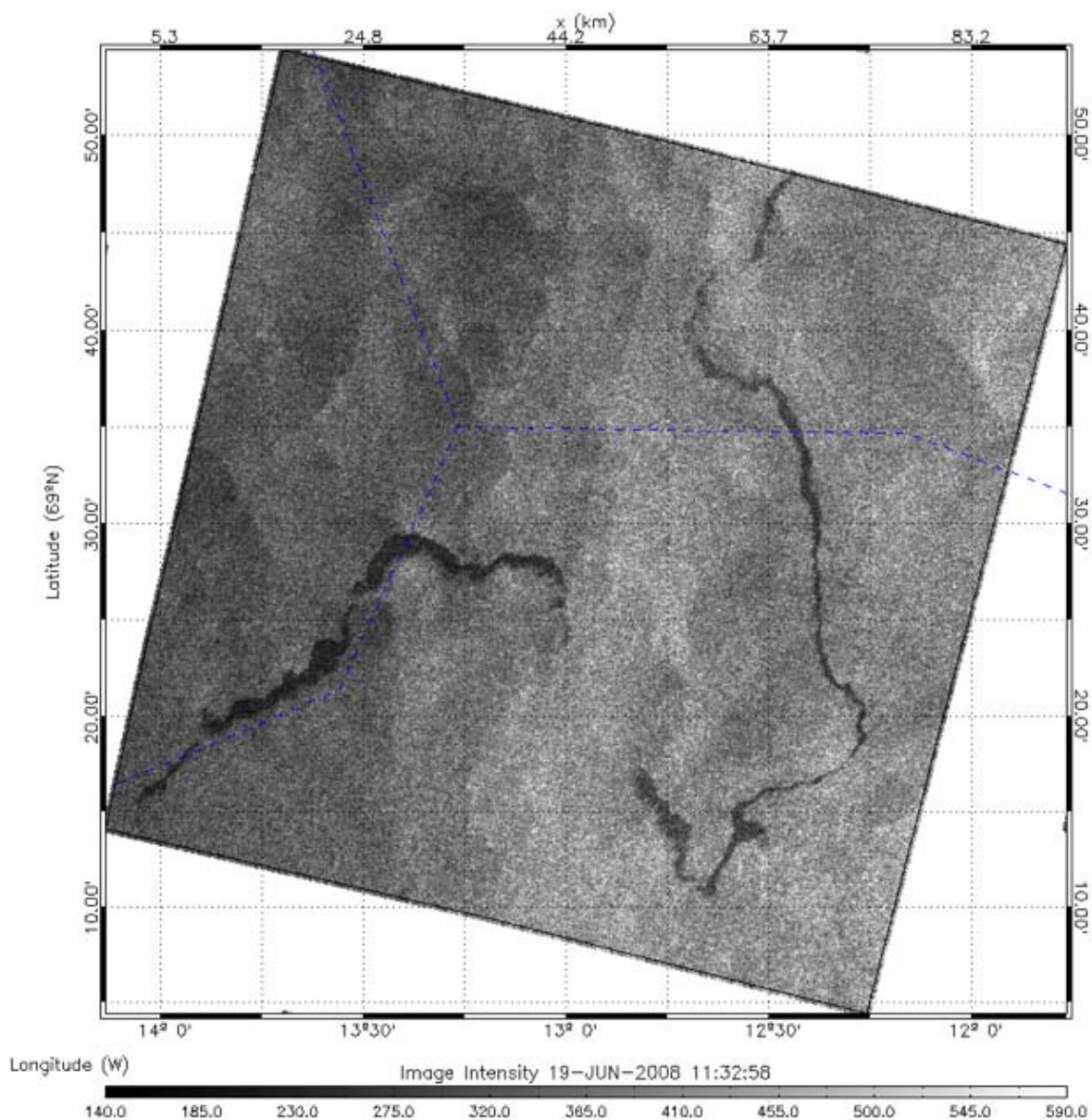


Figure 3-4. ASAR image from the Norwegian Sea on 19 June 2008. The wind speed in the image is 6 – 8 m/s, which is favourable for oil spill detection.

3.3.2 Head of Kinsale, Ireland

In February 2009 about 300 tonnes of oil were been spilled from a ship off the southern coast of Ireland. The incident, which took place in the vicinity of Russian naval vessels about 50 miles south of Fastnet, is believed to have occurred as a result of a refuelling operation. The spill is very well-defined in the ASAR image obtained on 14 February (Figure 3-5). By use of SARTool the imaging parameters of the spill were extracted and shown on Table 3-2.

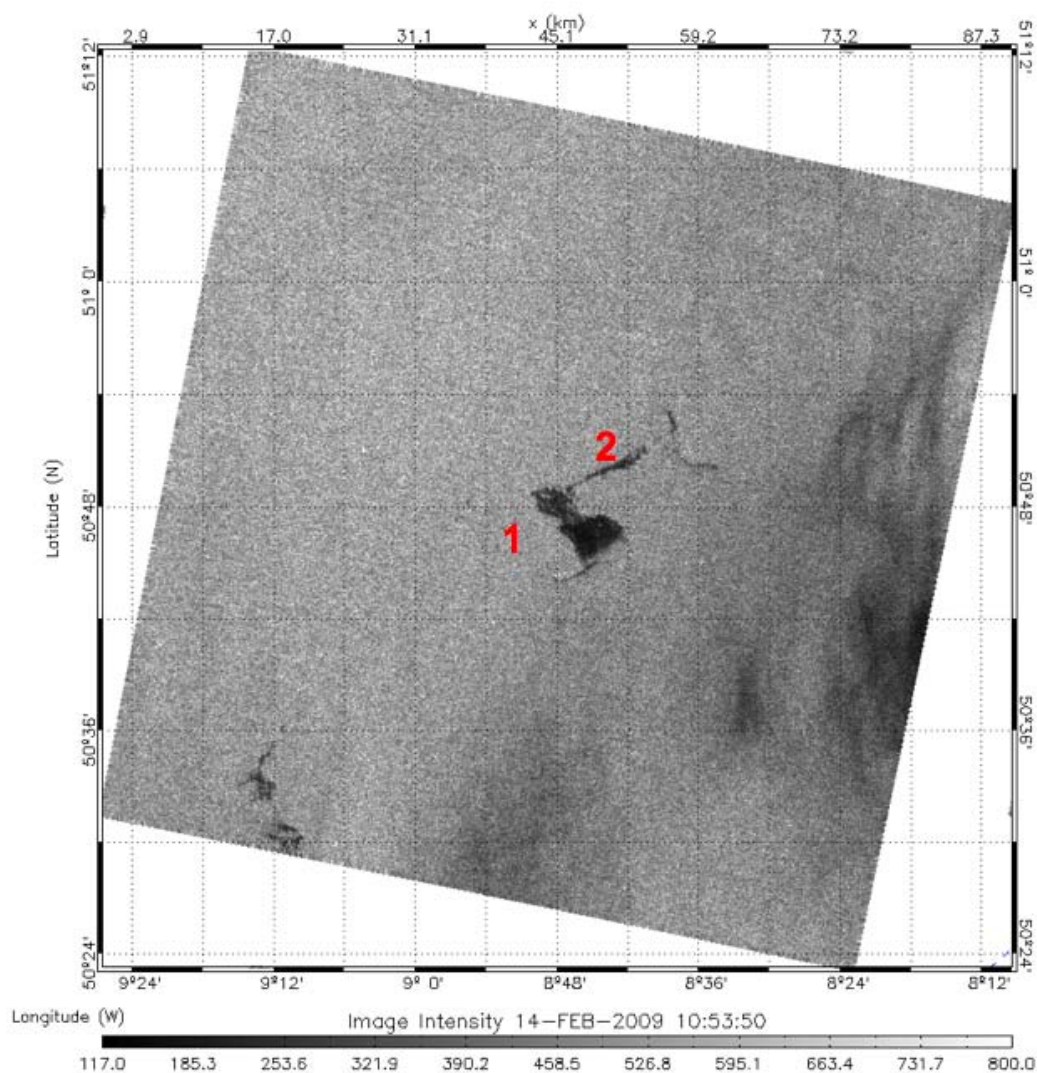


Figure 3-5. ASAR image from the Ireland Sea showing the oil spill, probably released by Russian naval ships before 14 February 2009 when the image was obtained. The wind speed was 3- 6 m/s.

Table 3-2 Parameters of the oil spill presented in Fig3-5

ID	Wind	Length	Perimeter	Area	Complexity	Spread	Slenderness
1	4.67 m/s	9.81 km	30.15 km	28.62 km	2.53	500.34	303.61
2	4.67 m/s	5.34 km	12.99 km	3.50 km	3.83	71.13	66.46

4. BLACK SEA: SAR MONITORING OF OIL SPILLS

The second analysed data set for the Black Sea was based on ENVISAT ASAR images acquired by NERSC, including 113 widewath, 122 image mode, and 23 alternating polarisation images. All images were processed with SARTool provided by BOOST Technologies. Auxiliary data including optical and AVHRR images from MHI receiving station were used to study the sea surface dynamic in the ASAR scenes. Analysis of SST maps and wind characteristics from QuikScat and SAR images retrieved with SARTool helped to separate oil spills manifestations in ASAR images from 'look-alikes'. Example of 'look-alike' in dynamic area is shown in Fig.4-1. The variability in sea surface temperature can generate features in the SAR images that are similar to slicks due to transformation of atmosphere boundary layer overlying a thermal front or presence of convergence zones (Kudryavtsev, 1999; Kudryavtsev et al., 2005). Depressed NRCS in ASAR ENVISAT from 12 May 2007 shown in Fig.4-1 is result of smoothing sea surface in current convergence zones in the West part of the Black Sea.

The Black Sea region is characterized by growing offshore oil production, tanker traffic and pipelines, with increased risk for oil pollution. The oil slick behind the ship shown as the bright object is illustrated in Fig.4-2 where ASAR image from 9 August 2007 is shown. The largest spill identified with ENVISAT ASAR from 15 July 2007 is illustrated in Fig.4-3. This oil spill was located to the North of Turkey coast and had area 98 km² and length about 40 km.

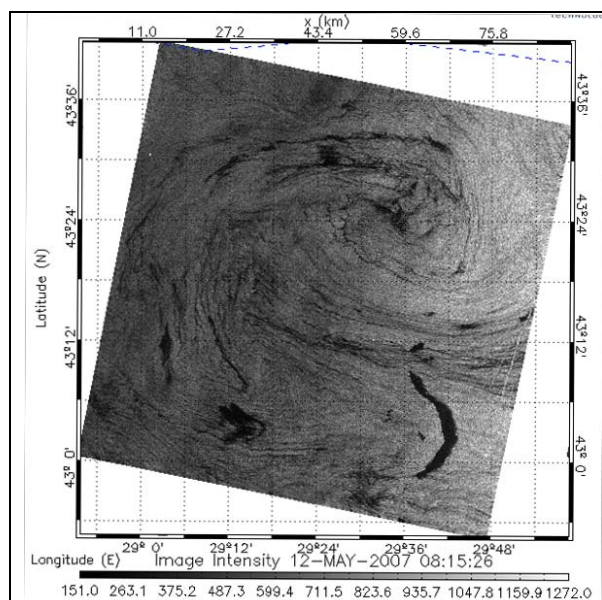


Figure 4-1. ASAR image from 12 may 2007 in the western Black Sea

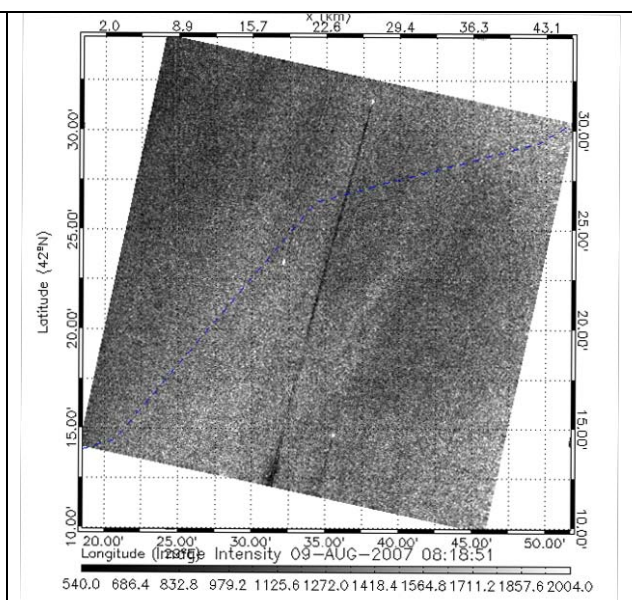


Figure 4-2 ASAR image from 09 August 2007, showing a straight line of oil spill from a ship

The examples of surface slicks examined demonstrate the problem to identify and discriminate oils spills from natural slicks in SAR images. Generally, radar contrasts caused by films and ‘look-alikes’ can be similar to each other. Also geometrical differences in the shape and size of oil spills and ‘look-alikes’ in SAR images can be similar (e.g. Calabresi et al., 1999). However, there are also more well-defined examples where it is relatively easy to determine that a slick must be caused by oil spills. The total number of recognized oil spill events in all the 367 analyzed SAR images is 258.

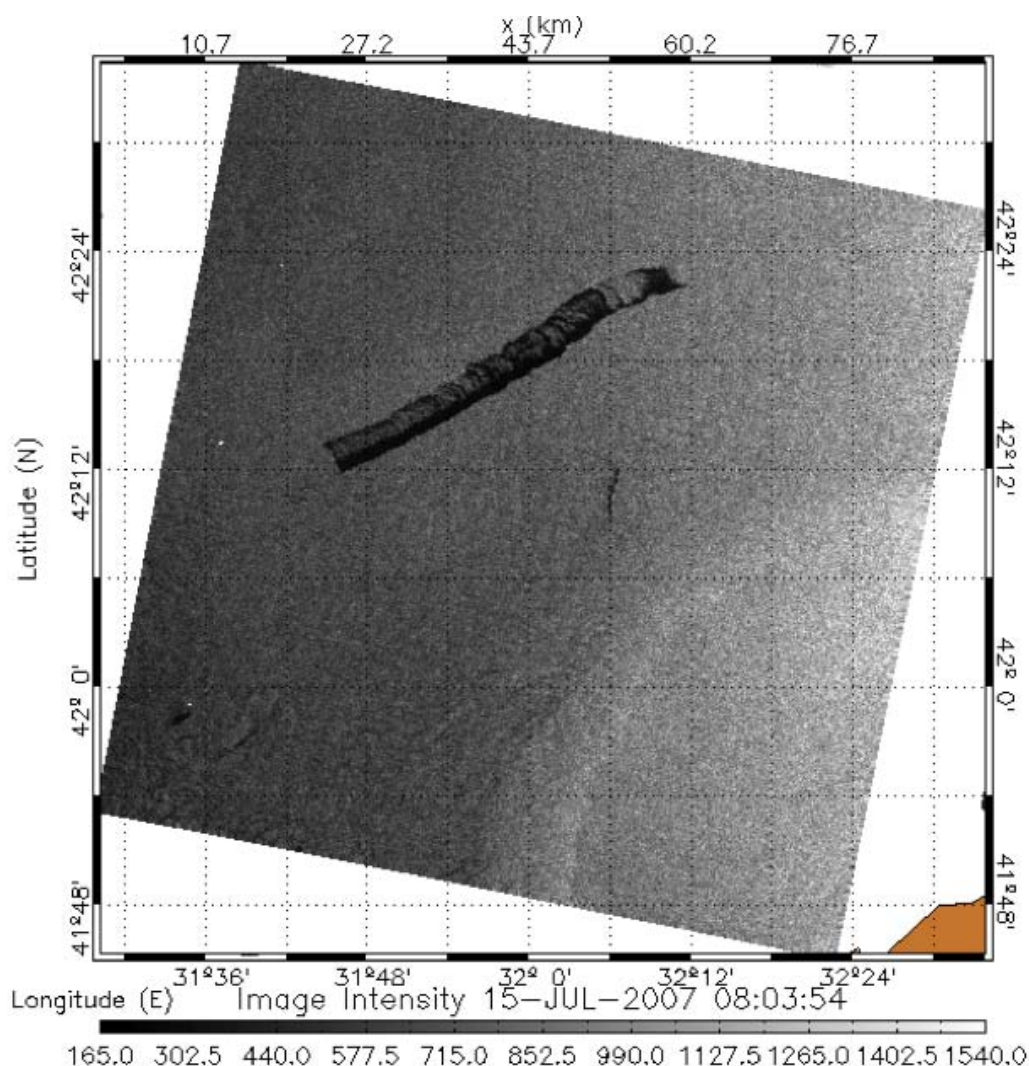


Figure 4-3. The largest oil spill found in the Black Sea was found in the ASAR image of 15 July 2007 north of the coast of Turkey. The length of the oil spill area is about 40 km.

Statistical distributions of oil spill sizes including length, area and NRCS contrasts are shown in Fig.4-4. The majority of oil spills recognized using ASAR ENVISAT occurred under weak and moderate winds from 1 m/s to 6 m/s. Distributions of oil spill sizes show that the most probably spill lengths are less than 7-8 km (fig.4-4a) with areas less than 7 km² (Fig.4-4b). The majority of NRCS contrasts illustrated in Fig.4-4c have values from 1.1 to 1.8.

Results of SAR monitoring of the Black Sea from May 2007 to February 2008 within MONRUK project is presented in Fig.4.5 where recognized oil spill locations are marked by symbols (+). The spatial distribution of the spills showed most frequent occurrence along the main tanker routes, near offshore oil platform positions, and in the large ports. Spatial distribution of oil spills in Fig.4-5 is in a good agreement with results of SAR monitoring carried out within ESA-IAF project OSCSAR under the programme “GMES Networking with Russian and Ukraine 2004-2005” demonstrated in Fig.4-6 (Malinovsky et al., 2007). These maps show that the main pollution areas are along the sailing routes from Odessa to Istanbul and from Novorossiisk to Istanbul.

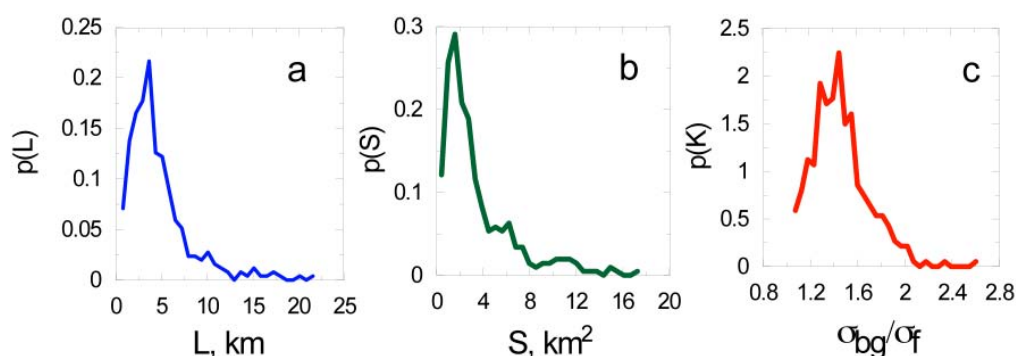


Figure 4-4. Histogram distribution of recognized oil spills: a – length, b – square, c – normalized radar cross section contrast in slick areas

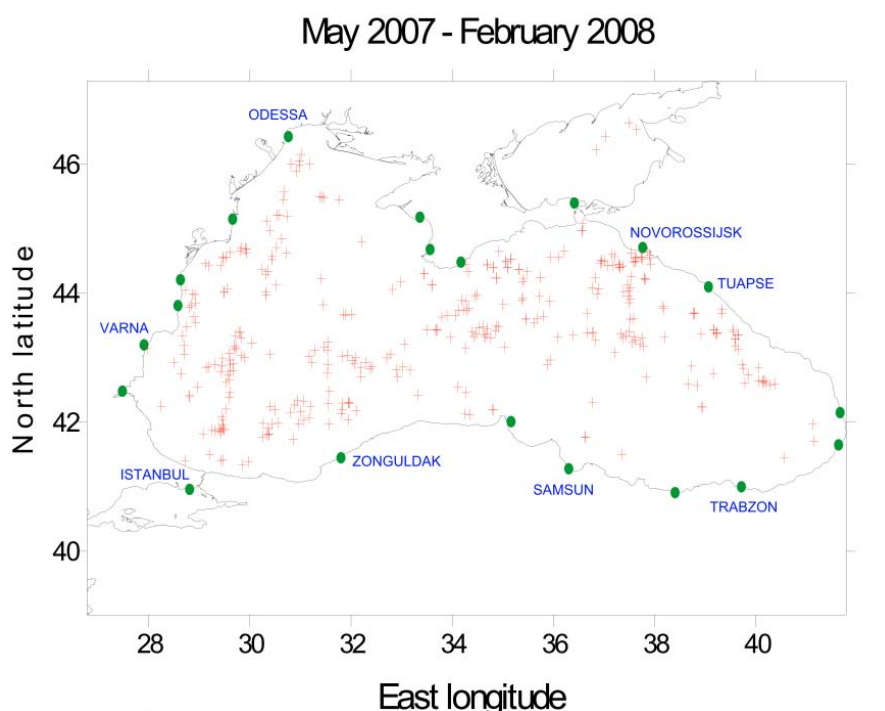


Figure 4-5. Spatial distribution of observed oil spills in the Black Sea during the MONRUK project

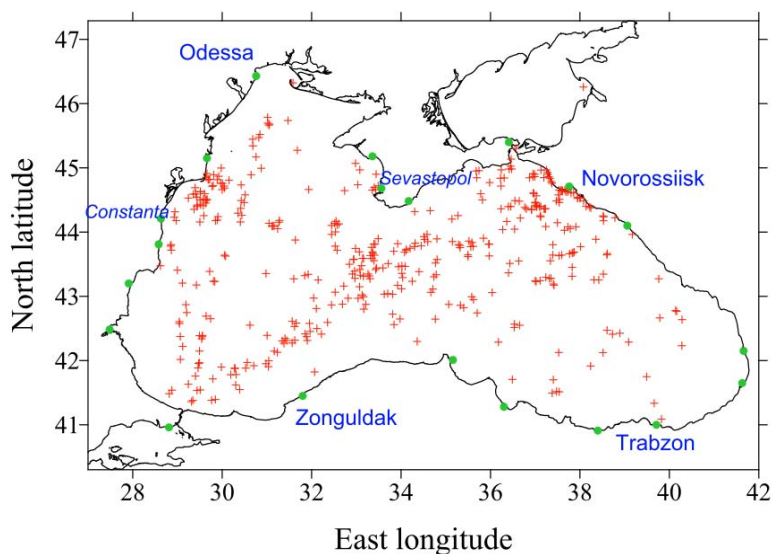


Figure 4-6. Distribution of oil spills observed in SAR images during the period 2002 – 2005 as part of the ESA/IAF OSCSAR project (Malinovsky et al., 2007).

5. CASPIAN SEA: SAR MONITORING OF OIL SPILLS

During 2007 and 2008 two summer monitoring studies have been carried out in the Caspian Sea using ASAR Wide Swath images that were analyzed by means of SARTool. Previous studies in the OSCSAR project have shown that the oil pollution in the Caspian Sea is concentrated in two areas:

- the oil producing area near Apsheron;
- the southwest part of Caspian sea water area.

It was shown that the volume of oil pollution varies significantly from day to day and that some of oil spills could be caused by leakage from pipelines and seeps from the seafloor associated with lithosphere processes (Feoktistov et al., 2006).

5.1 Monitoring studies in summer 2007

The SAR data from 2007 showed that most of oil pollution was concentrated in the same areas, as in the previous studies, the Apsheron are and the southwestern Caspian Sea. In many cases several slicks were found in clusters with considerable linear dimensions (Feoktistov et al., 2007; Novikova et al., 2008; Feoktistov et al., 2008).

5.1.1 Oil producing area near Apsheron

In the oil producing area near Apsheron observations of large oil slicks could be connected to oil leakage from old oil pipelines in a zone of active lithospheric processes, especially earth quakes. An examples, the results SAR image analysis from 04 and 30 July 2007 are shown in Figure 5-1 and 5-2. Oil leaks from oil industry infrastructure are clearly visible in full resolution subsets of the wideswath ASAR images. In Figure 5-2 an abnormal high level of oil pollution with many large oil slicks were observed near to Apsheron. Unfortunately, because of low wind speed oil spills identification was complicated, and identification was simply impossible on a significant part of the image.

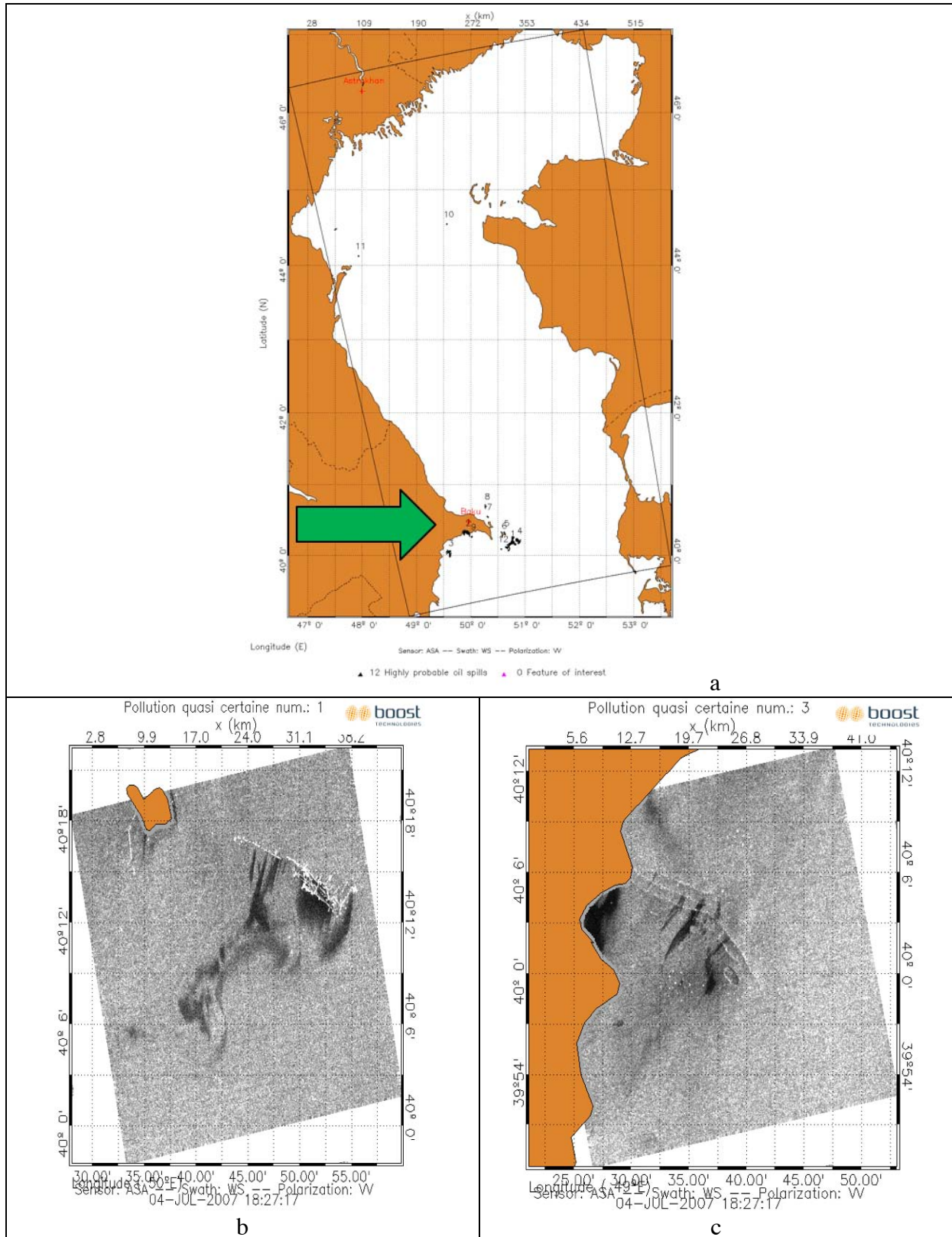


Figure 5-1 (a) Overview map of oil slicks location of 12 high probability oil spills identified by SARTool in the ASAR image from 04 July, 2007; (b) full-resolution subimage showing pollution area no. 1 shown in the overview map; (c) the same for area no. 3.

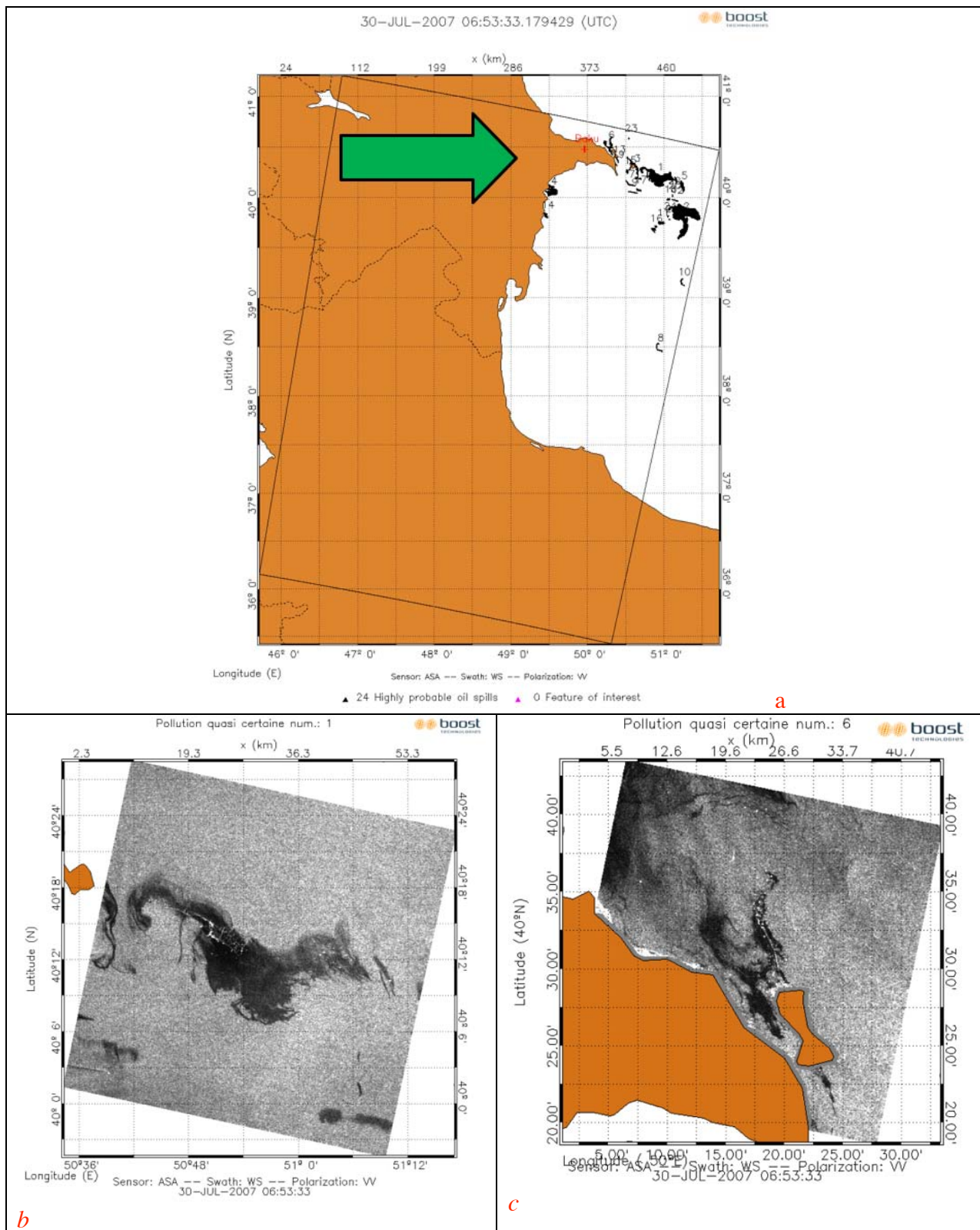


Figure 5-2 (a) Overview map of oil slicks locations identified by SARTool in the Wideswath ASAR image from 30 July, 2007; (b) full-resolution subimage showing pollution area no. 1 shown in the overview map; (c) the same for area no. 6.

5.1.2 Southwestern part of Caspian sea water area

In the southwest part of the Caspian Sea, hydrocarbon leakage from griffons (natural hydrocarbon containers under a sea-bottom) has been observed in previous studies as oil slicks in ASAR images (Figure 5-3). Analysis of the SAR data from 2007 has confirmed that many of the oil spills are caused by leakage from seepage areas on the seafloor. As an example the case of very high level of sea surface oil pollution is submitted on Figure 5-4 for WS ASAR/ENVISAT image from July, 7, 2007. The size and spreading of the oil slicks depends on (1) hydrocarbon leakage quantity and speed from seepage areas, (2) wind speed and (3) current speed.

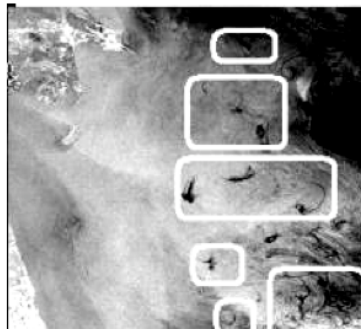


Figure 5-3 ASAR image (quicklook) of the southwest part of Caspian sea where several oil spills were observed on 05 July 2003.

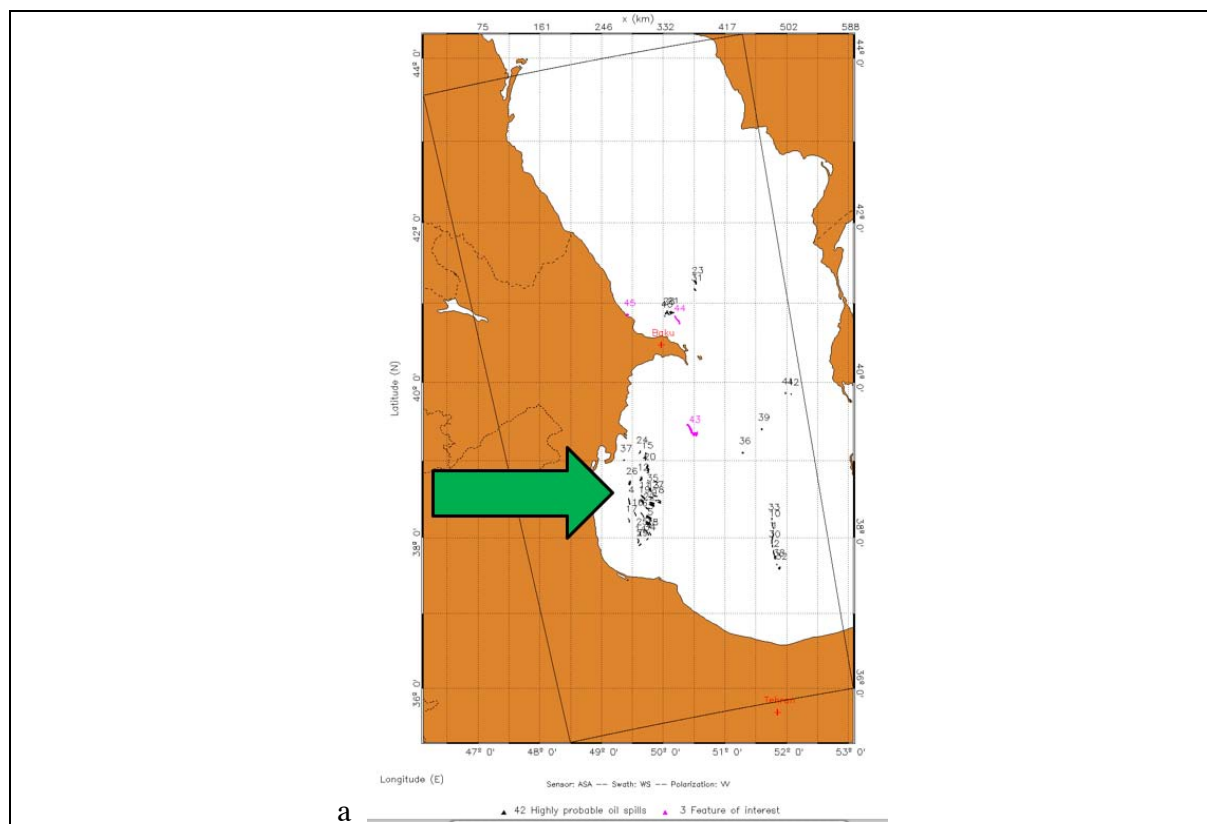
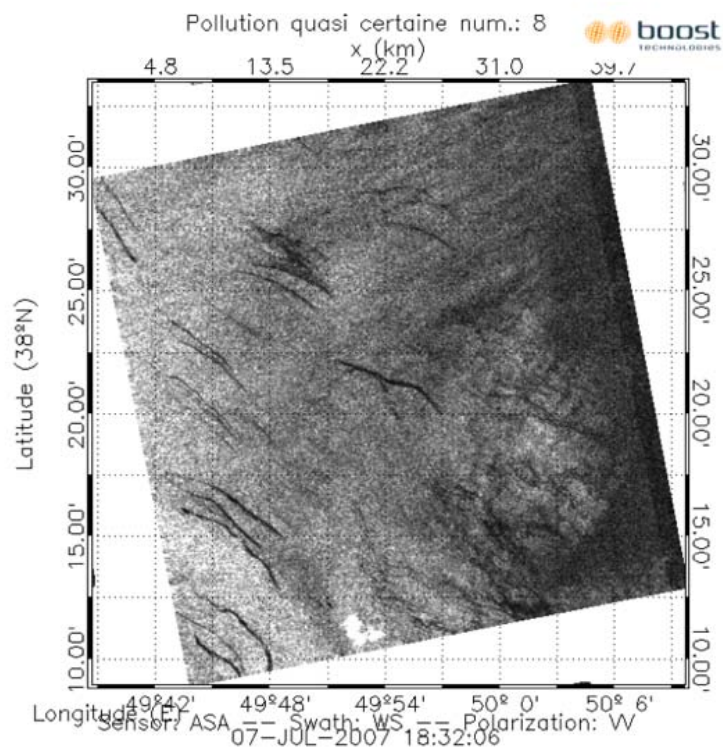
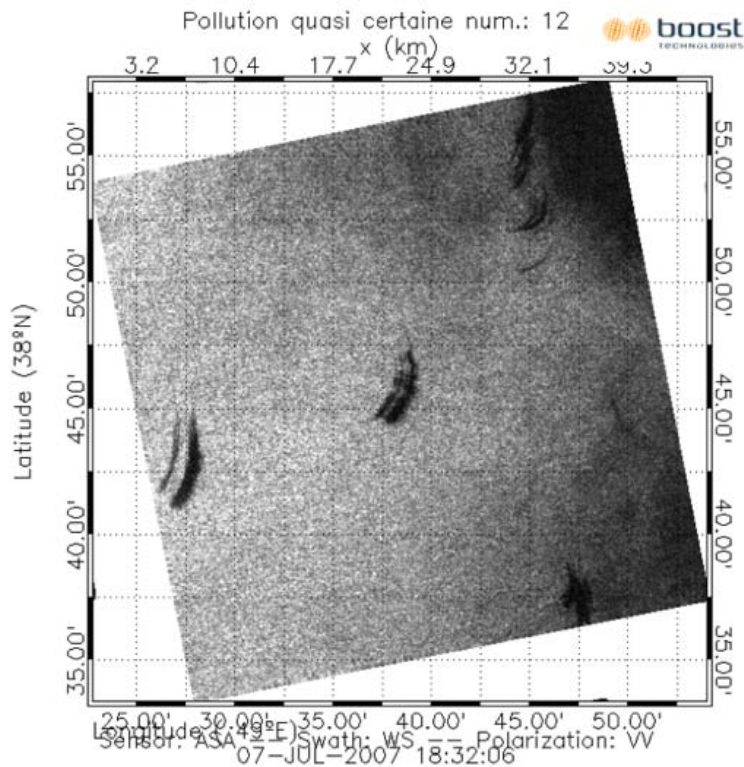


Figure 5-4 (a) Overview map of oil slicks locations identified by SARTool in the Wideswath ASAR image from 07 July, 2007;



b



c

Figure 5-4 (b) Full-resolution subimage showing pollution area no. 8 shown in the overview map; (c) the same for area no. 12

5.2 Monitoring studies in summer 2008

After the analysis of the 2007 data, the density of oil slicks was found to be very high in the Apsheron area and in southwestern Caspian Sea. All spills observed in these areas were compiled in contour maps using SARTool Program. During analysis of the 2008 data each oil spill polygon detected by SARTool was used to define cluster, with identification of date and time, dimensions, center of cluster coordinates, total of oil slicks in this cluster. As an example the results of the SAR image analysis on 11 August 2008 are shown in Figure 5-5.

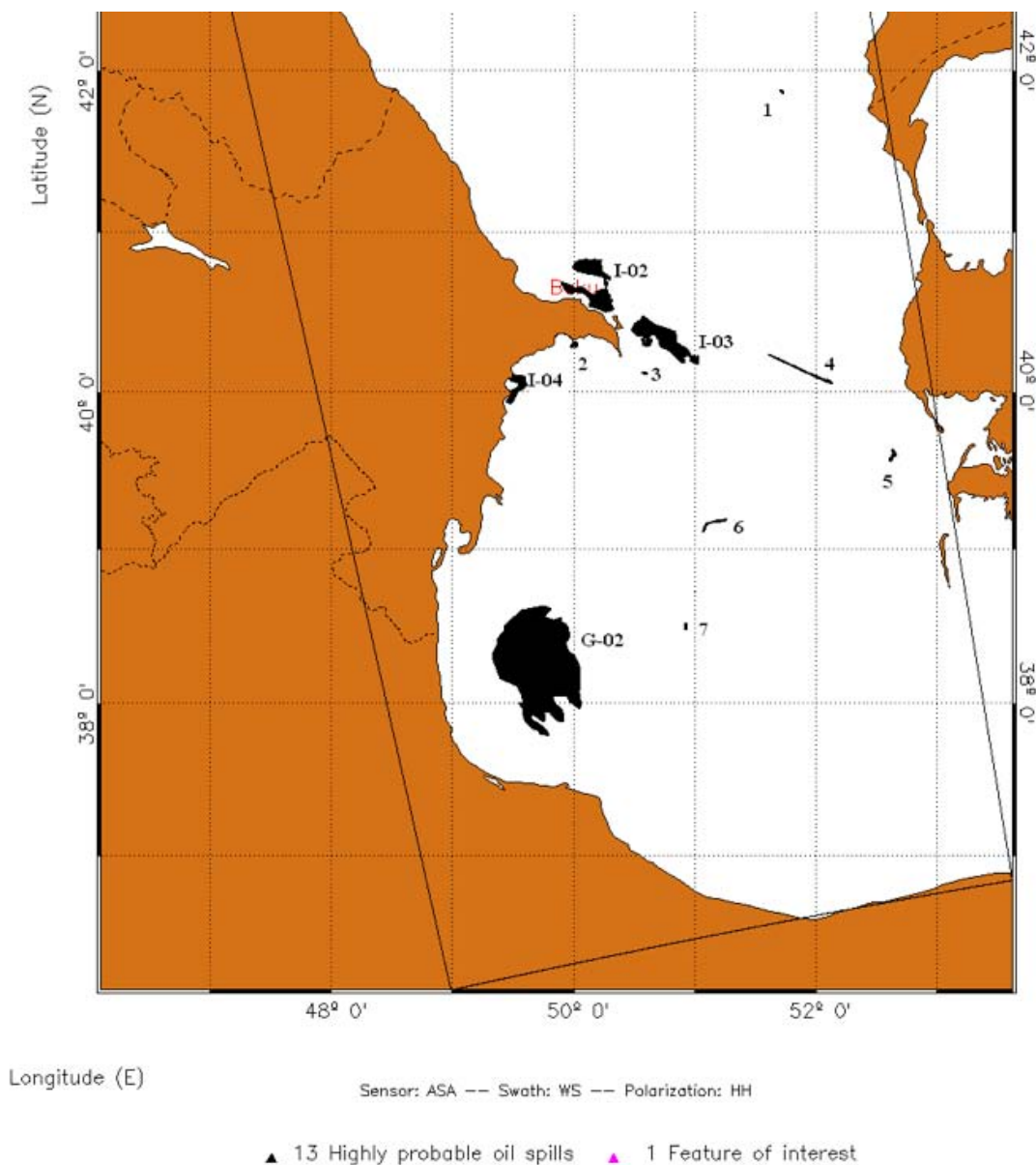


Figure 5.5 (a) Map of oil slick clusters observed in the ASAR image of 11 August 2008: I-02, I-03, I-04 - 3 are in the oil producing area near Apsheron; G-02 is a cluster in the southwestern part of Caspian Sea

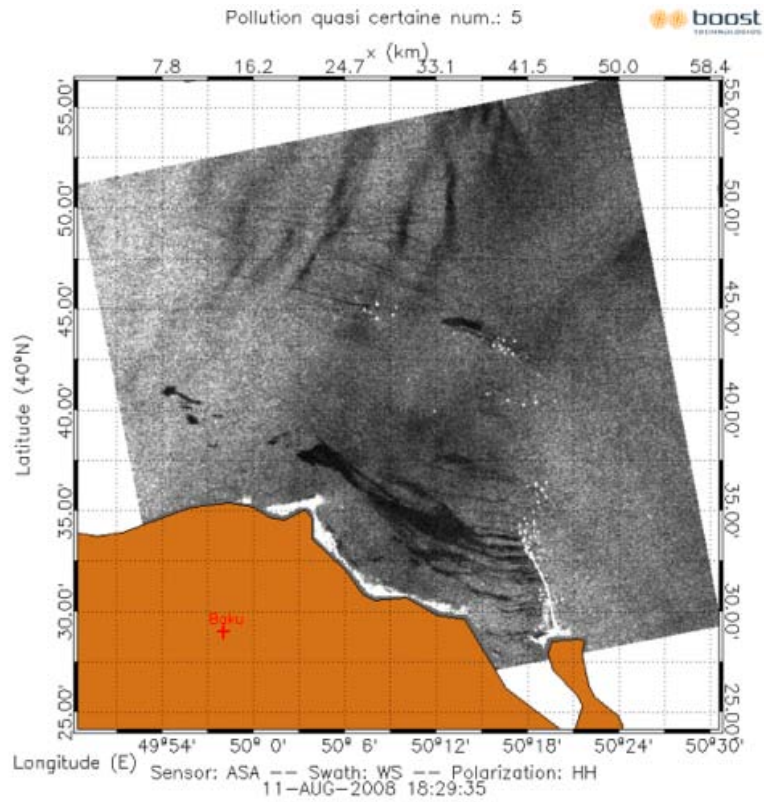


Figure 5.5 (b) ASAR image used to define oil spill cluster I-02 on 11 August 2008.

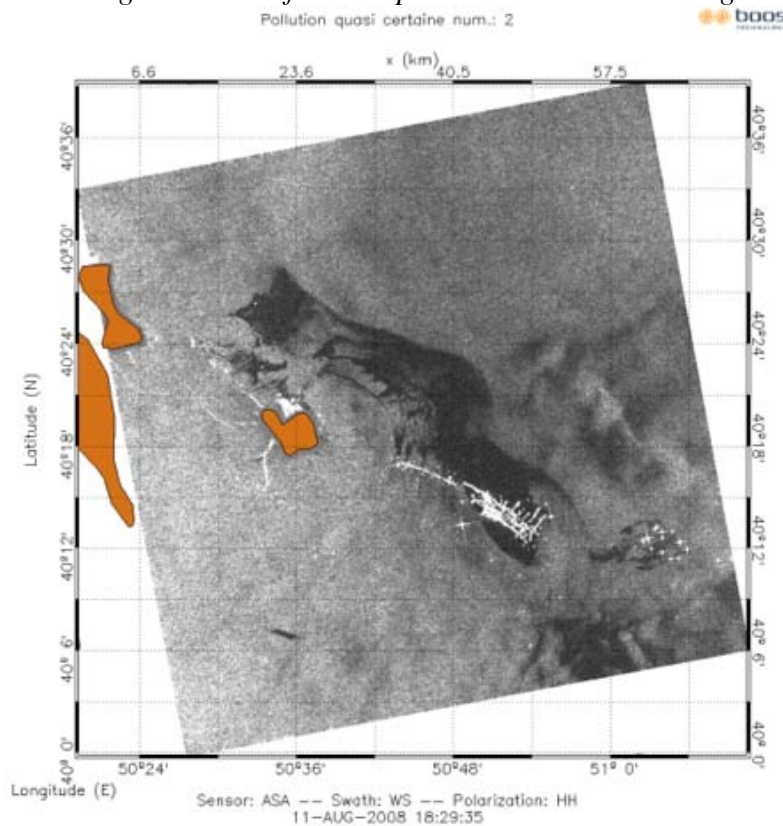


Figure 5.5 (c) ASAR image used to define oil spill cluster I-03 on 11 August 2008.



Figure 5.5 (d) ASAR image used to define oil spill cluster G-02 on 11 August 2008.

5.3 Results

A total of 47 ASAR images were analyzed for the Caspian Sea in 2008. This supplements the processing of 34 ASAR images in 2007. The main results of the SAR analysis is that there are intensive oil spill activities in two areas, the Apsheron area offshore of Baku in Aserbadjan, and in the southwestern Caspian Sea. The most probable processes that can explain these oil spill observations: leakage from offshore oil production installations including pipelines and oil seeps from the seafloor due to leakage from oil reservoir. This is an area of frequent earthquakes, causing such leakages to occur frequently. No in situ observations of the oil spills have been available for verification of the SAR observations. However, the systematic occurrence of spill signature in the SAR images, suggest that the observations are due to oil spills and oil seepage rather than biogenic films.

6. RETRIEVAL OF SURFACE VELOCITY USING SAR DOPPLER SIGNAL

Envisat's ASAR instrument measures backscattered radar echoes in amplitude and in phase, providing Doppler signals used in the processing for enhanced image resolution. Over the ocean, the Doppler signal differs from a predicted signal which is based on the a priori known motion of the satellite and the Earth rotation. Recently (Chapron et al., 2005) demonstrated that this Doppler signal difference is a measure of the Line-Of-Sight Velocity (LOSV) of the moving ocean surface. It is thus induced by the combined action of near surface wind speed, wave motion and surface current, and offers estimate of the corresponding surface component of this velocity in the range direction as the incidence angle is known. It complements the Normalised Radar Cross Section (NRCS) measurements and offer better quantitative interpretation of the relationship between the usual complex roughness pattern and upper ocean dynamic conditions.

The key to retrieve surface velocities in the SAR range direction is in the estimation of a Doppler centroid frequency anomaly which is converted to a surface velocity by a simple Doppler equation. The Doppler centroid is defined as the absolute frequency of the return-signal in the centre of the radar beam, and to find the anomaly we use the difference between a signal estimate and the independent geometric estimate of the Doppler centroid frequencies based on measurements of the sensor's foot-print, satellite attitude, and an Earth model.

6.1 Systematic Doppler Monitoring of sea areas

Since December 2008 the NERSC satellite data web server has provided SAR Wide Swath Mode Doppler figures over areas in the Kara Sea, the Black Sea, the Caspian Sea, and an area around Okhotsk. As there is no major currents in these areas that are in favourable orientation with respect to the SAR range direction, it is assumed that the sea Doppler anomalies are dominated by the orbital motion of wind waves. A qualitative measure of this assumption is illustrated in Fig. 6-1, where the Doppler surface velocities are shown to the left of wind calculated by CMOD-4. The eddy signature of wind over the Black Sea is evident in both images, and at the bottom (Mediterranean Sea) it can be seen that the Doppler gives a fairly better idea of the wind directions which in CMOD-4 are taken from an external model (NCEP). Fig. 6-2 provides another example of wind induced Doppler.

To extract further information about the sea state, the plan is to improve the wind estimation by using a Bayesian algorithm that will take advantage of both the Doppler velocities (with an a priori assumption that the signal is only caused by wind), and the Normalised Radar Cross Section (NRCS) estimate by CMOD-4 with wind direction from a model wind (NCEP). The output wind may then be used to generate a theoretical wind Doppler by the use of a radar imaging model (Kudryavtsev et al., 2005; Johannessen et al., 2005), and remove this wind Doppler to be left with surface current signatures.

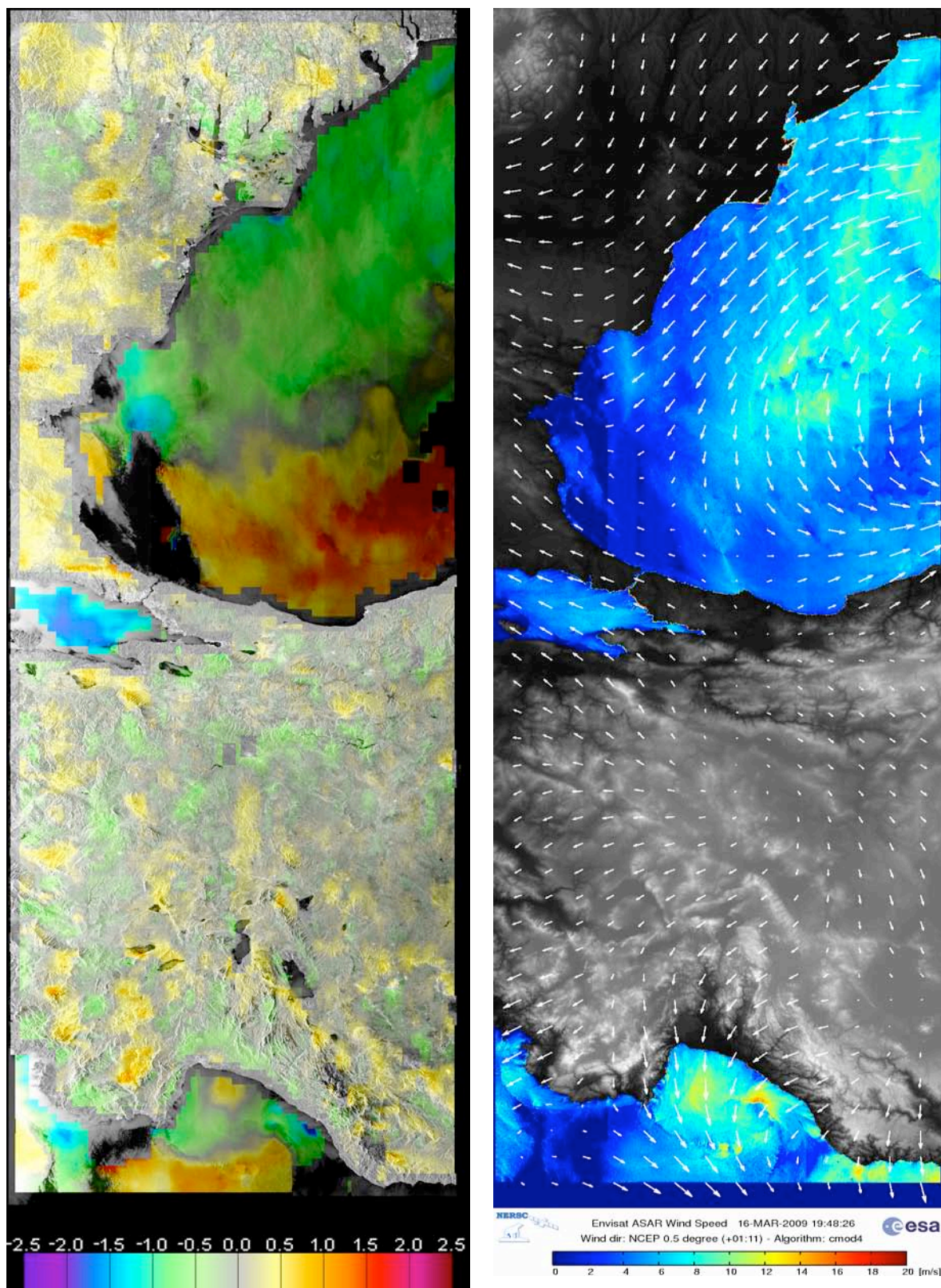


Figure 6-1 Directions of Doppler velocities over the Black Sea (positive toward East) show

good agreement with CMOD-4 wind. Green colour means velocity towards west.

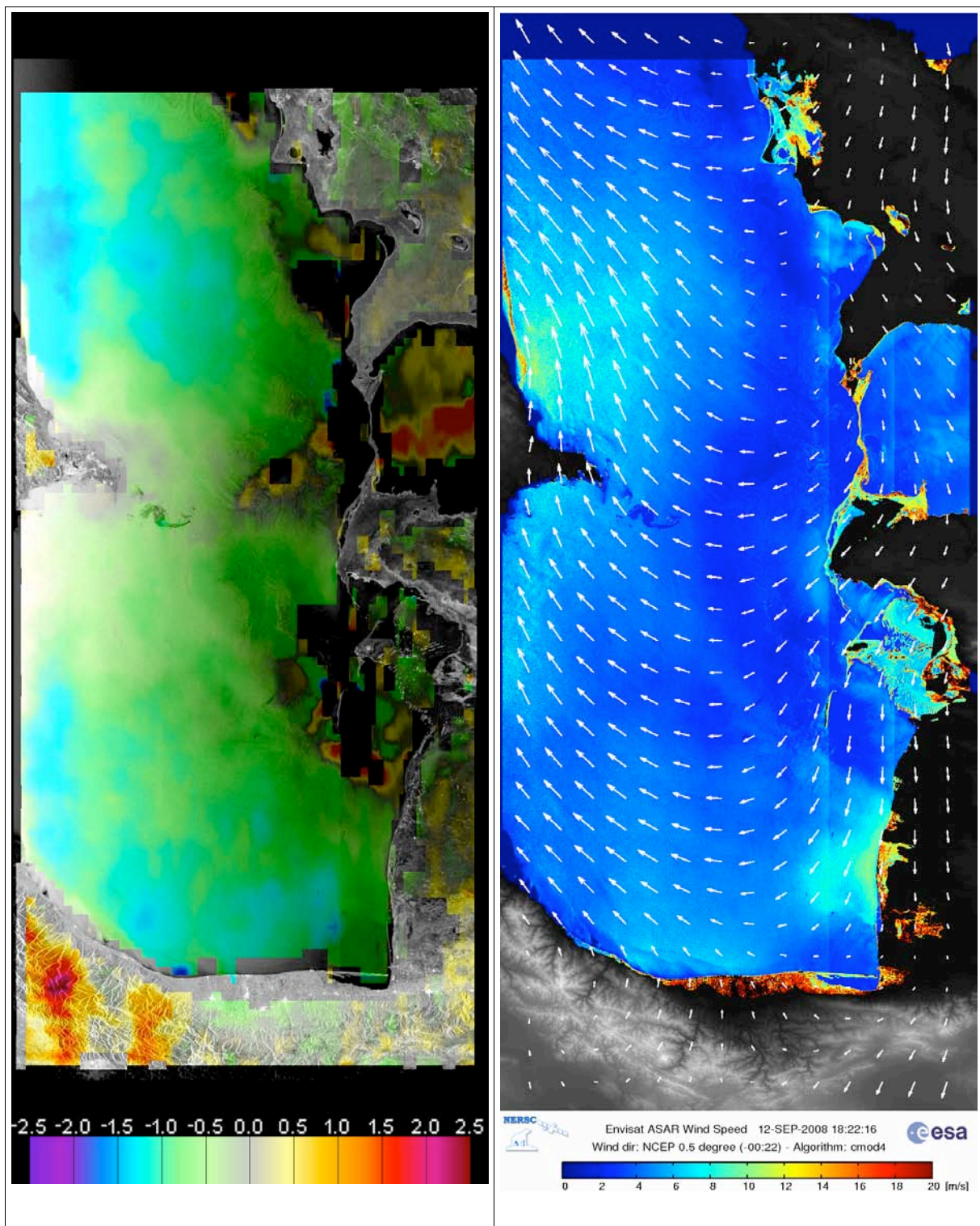


Figure 6-2 Directions of Doppler velocities over the Caspian Sea (positive toward East) also show good agreement with CMOD-4 wind. Green colour means velocity towards west.

7. CONCLUSIONS

This report presents results of the second analysed ASAR data set for open ocean monitoring over the study areas: Barents, Kara, Black and Caspian Sea. ASAR data were received from the ESA rolling archive, stored at NERSC and NIERSC servers, and then distributed among the project partners. Analysis of ASAR data was focused on investigation of the most important oceanographic phenomena with use of existing and newly developed retrieval algorithms, in particular: with use of SARTool provided by BOOST Technologies, and the Radar Imaging Model (RIM) developed at NIERSC/NERSC. The report has presented a number of examples of analyzed SAR data sets, showing various ocean phenomena summarized in Table 7-1.

Table 7-1 Observed phenomena

Feature	Area	Number of observed features	Number of SAR images analyzed	Derived characteristics
Oil spill	Barents and Kara Seas	22	230	<ul style="list-style-type: none"> - length, perimeter, area; - Normalised Radar Cross Section contrast; - wind conditions; - spill propagation direction; - source of pollution
Oil spill	Black Sea	258	367	
Oil spill	Caspian Sea	12/17	34 (2007)/ 47 (2008)	
Internal Waves	Barents Sea	250	59	<ul style="list-style-type: none"> - sources of generation; - phase velocity and direction; - distance between IW trains; - IW wavelength; - mixed layer depth;
Surface Current features:	Barents and Kara Seas	47	171	<ul style="list-style-type: none"> - current front position; - type of the current feature, eddies and meanders - type of the current shear, convergence or divergence;
Wind Field, (Polar Laws for Barents and Kara seas)	Barents and Kara Seas, Black Sea and Caspian Sea	Wind field is calculated for all SAR images over sea areas collected at NIERSC.	Processing automatically at NIERSC and NERSC servers at request.	Wind velocity and direction. Barents sea, - Polar laws, statistics is not completed.
Doppler velocity field	Barents and Kara Seas, Black Sea and Caspian Sea	Calculated for all SAR images over a sea collected at NERSC after Dec 2008	Processing is done automatically at NERSC server at request	Velocity of scattering facets possessing wind drift and ocean surface current velocity, which can be sorted separately.

SAR monitoring performed over the Barents and Kara seas was mainly focused on study of sub-mesoscale ocean currents and fronts, internal waves and wind field. Motivation of such kind studies caused by important applied significance of each of the investigating phenomena: “instant” location of sub-mesoscal current features (zones of convergence and divergence) and fronts which are indicator of potential accumulation of fish is of crucial importance for fishery; mapping of spatial distribution of internal waves and their energy is important for navy needs; monitoring of wind field with emphasis to polar laws is needed for many industrial activity and navigation. As found meso-scale current features, fronts and internal

waves can routinely be observed by SAR. These oceanic dynamical phenomena were classified, analyzed, mapped and interpreted with combine use of SARTool and RIM model. Supplementation of SAR data with output of operational HIRES Barents Sea current model, as well as IR and optical satellite images significantly facilitates interpretation of observed SAR signatures.

Implementation, training and use of SARtool for oil spills detection and quantification has been an important part of the project, allowing the partners to analyze a large number of image in the study areas. Analysis of SAR data for oil spill detection was done in all areas, showing that the most extensive occurrence of oil spills was found in the Black Sea and Caspian Seas. In these areas, statistical parameters of observed oil spills were calculated. The most extensive study of oil spills was performed over the Black Sea. The spatial distribution of the spills showed that most frequent occurrence of oil spills take place along the main tanker routes, near offshore oil platform positions, and in the large ports. As found the “new” map of oil spills distribution is very similar to that was obtained before within ESA-IAF project OSCSAR. The amount of SAR images analyzed over Caspian sea is much less then over the Black sea (see Table 7-1). However the analysis revealed an important result that the main contribution to oil spills pollutions comes from not only industrial activities such as oil platforms and pipelines, but also from natural leakage from the seafloor.

Detection of the Doppler surface velocity from SAR data is new perspective approach implemented in the project. Doppler velocity field contains both wind drift and surface current. The latter is desire oceanographic parameter, and could be derived from the total velocity if wind dependence of the Doppler velocity is established (analogy to CMOD4). It is anticipated that reconstruction of the surface current from Doppler velocity field will be completed soon. The progress achieved by BOOSTechnologies in this field make this problem feasible.

8. REFERENCES

- Alpers, W and H. E. Espedal, Oils and Surfactants, Synthetic Aperture Radar Marine User's Manual. Eds: Jackson and Apel, NOAA, 2004
- Beal, R., V. Kudryavtsev, D. Thompson, S. Grodsky, D. Tilley, V. Dulov, and H. Graber, The influence of the marine atmospheric boundary layer on ERS-1 synthetic aperture radar imagery of the Gulf Stream. *J. Geophys. Res.*, 102, C3, 5799-5814, 1997
- Calabresi G., Frate F.D., Lichtenegger J., Petrocchi A., Trivero P. (1999). Neural networks for the oil spill detection using ERS-SAR data. *Proceedings of IGARSS '99*, v.1, p. 215 – 217.
- Chapron, B., F. Collard, and F. Ardhum (2005), Direct measurements of ocean surface velocity from space: Interpretation and validation, *J. Geophys. Res.*, 110, C07008, doi:10.1029/2004JC002809
- Espedal, H.A., Oil spill and its look-alikes in ERS SAR Imagery. *Earth Obs. Rem. Sens.*, 16, 813-825, 2001
- Feoktistov A.A., Novikova N.N., Pakhomov L.A., Lyushvin P.V., Zakharov A.I., Martynov S.I., Fedichev O.B., Miroshin A.A. The development of sea surface oil pollution space monitoring system // Proc. of the Third All-Russia open conference. «Modern problems

- of remote sensing of the Earth from space». Moscow: Space Research Institute of the Russian Academy of Science. 2006. V.2. P. 161-167.
- Feoktistov A.A., Novikova N.N., Pakhomov L.A., and Zakharov A.I. Space monitoring of sea surface oil spills // Proceedings of the International Conference “Advances of satellite Oceanography: understanding and monitoring of Asian marginal seas”, 3-6 October, 2007, Vladivostok, Russia. P. 36-38.
- Feoktistov A.A., Novikova N.N., Pakhomov L.A., Zakharov A.I., Denisov P.V. Caspian sea surface monitoring within the framework of international projects DEMOSSS and MONRUK // Theses of the Sixth Anniversary Open All-Russia conference “Modern problems of remote sensing of the Earth from space”. Moscow: Space Research Institute of the Russian Academy of Science. November, 10-14, 2008. P. 87
- Jackson and Apel (editors), Synthetic Aperture Radar Marine User’s Manual, NOAA, 2004
- Johannessen, J.A., V.Kudryavtsev, D.Akimov, T. Eldevik, N. Winther, and B. Chapron, (2005), On Radar Imaging of Current Features; Part 2: Mesoscale Eddy and Current Front detection. Journal of Geophysical Research, 110, C07017, doi:10.1029/2004JC002802, 2005
- Kozlov I. SAR signatures of oceanic internal waves in the Barents Sea // Proceedings of the Second International Workshop on Advances in SAR Oceanography from Envisat and ERS missions, 21-25 January 2008, Frascati, Italy, (ESA SP-656), ESA Publications Division, 2008
- Kudryavtsev V., D.Akimov, J.A.Johannessen, and B. Chapron, (2005), On radar imaging of current features. Part 1: Model and comparison with observations, Journal of Geophysical Research, Vol. 110, C07016, doi:10.1029/2004JC002505, 2005
- Kudryavtsev V.N., Malinovsky V.V., Rodin A.V. (1999). Manifestation of temperature fronts in radar images of the ocean. *Issledovaniya Zemli iz Kosmosa.*, No 6, p. 16 – 26 [in Russian].
- Malinovsky V.V., S. Sandven, A.E. Korinenko (2007). SAR monitoring of oil spills and natural slicks in the Black Sea. *Proc. ENVISAT Symposium*, Montreux, Switzerland, 2007
- Novikova N.N., Pakhomov L.A., Feoktistov A.A., Zakharov A.I. International project DEMOSSS. Development of works on sea surface monitoring, started within the framework of the international projects OSCSAR and ERUNET // Proc. of the Fifth All-Russia open conference. “Modern problems of remote sensing of the Earth from space”. Moscow: Space Research Institute of the Russian Academy of Science. 2008. V.1. P. 155-159.
- Sandven, S., V. N. Kudryavtsev, D. Akimov, T. Hamre, L. Bobylev, V. Lavrenov, V. Stanovoy, S. A. Ermakov, A. Feoktistov, P.V. Lyushvin, V. V. Malinovsky, A. V. Agarkov, and S. Matvienko. OSCSAR – Marine Oil Spill Control, SAR monitoring and model prediction. Final report. NERSC Technical Report no 271, March 2006, 86 pp.

PART 2: SAR DATA ANALYSIS OF SEA ICE

1. INTRODUCTION

Sea ice and iceberg monitoring is one of the most important objectives for satellite SAR missions, such as ERS, ENVISAT, RADARSAT and the future Sentinel missions. In MONRUK SAR sea ice studies was performed in the Barents and Kara seas and Svalbard areas as well as in the Northern Caspian Sea.

The ongoing changes in Arctic climate with increasing temperatures and decreasing sea ice cover have stimulated the interest for oil and gas exploration in several Arctic areas. An overall reduction of the sea ice extent in particular during summer opens up the possibility to access new areas of the Arctic Ocean where hydrocarbon resources can be exploited and transported to the markets. The main Arctic areas where large-scale offshore exploration has started are: Sakhalin in Sea of Okhotsk, North Slope of Alaska, Cook Inlet, Grand Banks of Newfoundland, Barents Sea (Snøhvit field and the upcoming Shtokman field), the Pechora Sea and the northern Caspian Sea. Typical for all these areas is a seasonal sea ice cover and the occurrence of icebergs in some of them that put severe constraints on design and operation of installations and on transport solutions. Even if the sea ice cover is decreasing and is expected to diminish further in the coming decades, the sea ice will still remain a dominant factor in most of the exploration areas in the winter season.

Sea ice concentration, thickness, and pressure are the major direct factors influencing ice forcing on constructions and operations in ice areas. For offshore construction, the drift and thickness of ice are key parameters in calculation of ice loading. Maximum ice thickness is mainly determined by ridges, in particular the ridge keels, which are formed when ice floes are pushed against the shore and piled on top of each other. In shallow waters, where depths are less than 20 m, ice keels can become grounded and ridges can build up to more than 10 m as a result of the drifting ice floes. In addition to the general ice conditions (spatial ice type distribution, drift, concentration), it is very important to have specific data on ice thickness and ridge parameters in local regions where ice operations are planned. Oil companies usually need to collect region-specific data on sea ice parameters as part of the design phase studies for operations in Arctic areas. For offshore operations, there are two main situations for offshore operations that require different strategies regarding the specific ice conditions. The first situation is in shallow waters (5 – 20 m) where constructions are built on the seafloor and designed to withstand the forces of the drifting sea ice. The sea ice is often attached to the seafloor and can be stationary for a long time. But stationary ice can start to drift due to strong winds and pile up ice blocks forming *stamukhas*. The other situation is when operations take place in deeper water covered with ice that is freely drifting and also icebergs can occur. Floating constructions and ships can operate if they are designed to withstand the ice forcing. In case of extreme ice conditions, the platforms can be released and towed away.

Icebergs drifting in the ocean are one of the most dangerous threats to offshore operations. Icebergs are commonly found off eastern Canada, around Greenland, in the Barents Sea and several places in the Russian Arctic. On Grand Banks, there is a specific iceberg monitoring and management system to avoid collision between icebergs and platforms. In the Barents Sea area, systematic monitoring of icebergs was conducted by Russian aircraft surveys for many decades, but in the last 15 years there have been no regular iceberg surveys in this area [Sandven, 2008]. In May 2003, surprisingly many icebergs were observed in the Shtokman

area in the eastern Barents Sea. From ship radar observations, 109 iceberg and bergy bits were found in the area between 71 and 75 N and between 40 and 46 E. The largest iceberg was 190 by 430 m in horizontal extent and more than 50 m deep [Zubakin et al., 2004]. Due to this event, the iceberg occurrence probability for the Shtokman area was re-calculated and triggered the oil companies to plan an iceberg monitoring and forecasting system for the area. Since the iceberg distribution can vary strongly from year to year, it is important to have good monitoring and tracking systems for the icebergs. Such systems are not in operation for most parts of the Arctic today. Extreme events can happen from year to year and there is no direct method to predict when and where icebergs occur and how they drift in the ocean.

Enhanced warming in the Arctic is predicted in the next decades according to the climate models, but strong decadal variability must be expected [Johannessen et al., 2004]. This may cause colder periods with more sea ice conditions in some winters compared to the present situation, even if there is a long-term trend of decreasing ice cover. It is difficult to predict the sea cover for the coming winters, because the forecasting models are not capable of providing reliable seasonal and multiyear forecasts of weather and sea ice conditions. This means that design of platforms and other installations for winter operations must take into account extreme values of ice conditions, low temperature, high wind speeds and wave heights and icing.

Satellites have become an essential tool for sea ice monitoring in the Polar Regions, including the Baltic Sea, the Caspian Sea and other regional seas with winter sea ice. Use of Synthetic Aperture Radar (SAR) for monitoring sea ice in the Barents and Kara seas to support ice navigation has been demonstrated in numerous icebreaker expeditions, and the results have been published in a book by Johannessen et al. [2007]. The polar seas are too remote, inhospitable and large to make monitoring by any other means practicable. Ice conditions across polar and sub-polar seas are monitored routinely by national ice services, and these organizations make use of a range of satellite image data in order to generate ice charts with intervals ranging from a day to two weeks, depending on time in the season and location. Since the 1990s, the ice services have relied increasingly heavily on the use of synthetic aperture radar (SAR), which is able to image effectively in all weather and light conditions and can provide images able to resolve such features as ice floes, deformed and undeformed ice, ridges and icebergs. Indeed, nowadays, visible and infra-red imagery serves mainly to assist in the interpretation of SAR imagery. Some commercial organizations have also started ordering satellite image data for ice monitoring, recognizing that the national ice services do not offer ice charting frequently enough, in sufficient detail and with the right information needed for their purposes.

In this report, studies on Ice classification/concentration in the Barents and Kara Seas (chapter 2) has been done by V.Y. Alexandrov, N.Y. Zakhvatkina, and A.O. Yarigina (NIERSC, St. Petersburg), on sea ice analysis in Storfjorden (chapter 3) - by J. Büttner and J. Wåhlin (NERSC Bergen), on iceberg detection in Franz Josef Land (chapter 4) – by M. Babiker (NERSC. Bergen), and on sea ice monitoring in the Caspian Sea (chapter 5) – by A.A. Feoktistov, N.N. Novikova, L.A. Pakhomov, A.I. Zakharov and P.V. Denisov (NTs OMZ, Moscow).

2. ICE CLASSIFICATION/CONCENTRATION IN THE BARENTS AND KARA SEAS

A series of ENVISAT ASAR WS images, covering the western part of the Barents and Kara seas have been analyzed, interpreted and used in algorithm development. For this purpose more than 300 images were downloaded from the rolling archive.

2.1 Expert analysis and interpretation of SAR sea ice images

Analysis of ENVISAT ASAR images allows us to retrieve a number of sea ice parameters. During winter, several stages of ice development can be derived from SAR images, including new ice, young ice, first-year ice and old ice. Separate floes can be detected when their size significantly exceeds the spatial resolution of radar, typically 150 m for ENVISAT ASAR. The deformation of first-year ice can be detected and divided into: level ice, slightly deformed ice, moderate deformed ice and heavily deformed ice. Shore and flaw polynyas can be identified, and their width and area can be measured. The possibility to detect leads in drifting sea ice depends on their width and also the type of ice contained in them. Leads that are 100 m wide or more can be detected in 100-m resolution ScanSAR images. In most cases the fast ice and its boundary can be detected in SAR images. The determination of multi-year ice and its boundary is possible in most cases. From successive SAR images, the ice displacement can be estimated and drift vectors determined and detailed ice drift patterns can be derived. The following sea-ice parameters: ice edge location, sea-ice concentration, large ice floes, stripes of ice in water, ice drift vectors, and areas of convergence/divergence can all be derived from SAR (Sandven *et al.*, 2001).

Ambiguities in SAR images interpretation are caused by the similarity of signatures for different sea-ice types and features. It is difficult to distinguish between thin, medium, and thick first-year ice, and also between second-year and multi-year ice. Detection of dry snow on sea ice is impossible, since it does not significantly influence backscatter in the C-band.

A series of ENVISAT ASAR images in the winter 2008/2009 was used for studies of polynya development near the southeast coast of Novaya Zemlya (Fig. 2.1). Analysis of these images revealed that stable ice cover in the southeastern part of the Barents Sea was formed in the second half of January. At the same time it was possible to detect polynyas. In the ASAR image for January 23 a wide polynya is evident with dark tone (marked by B). This polynya is also evident in the ASAR images for January 24, 26, and 29. Then it was closed and we could not detect it in the ASAR images for February 1, 8, 11, and 18 (not shown here). On February 20 the polynya opened again and in the ASAR images for February 21 a wind-roughened surface has observed with very high backscatter (B in Fig. 2.1b). On February 28 it was covered by young ice. On March 2 the polynya started opened again. On March 8 it became quite wide and is evident from the dark tone in ENVISAT ASAR image (B in Fig. 2.1c). On March 12 the polynya was closed and was detected only in ENVISAT ASAR images for March 24 and 27. On March 28 the polynya was closed and it started forming again on April 13. In ASAR image for April 13 it had high backscatter, which is typical for wind-roughened water surface (B in Fig. 2.1d).

This is an example of how a series of SAR images can be used to study the development of sea ice conditions in the Arctic, especially polynya dynamics.

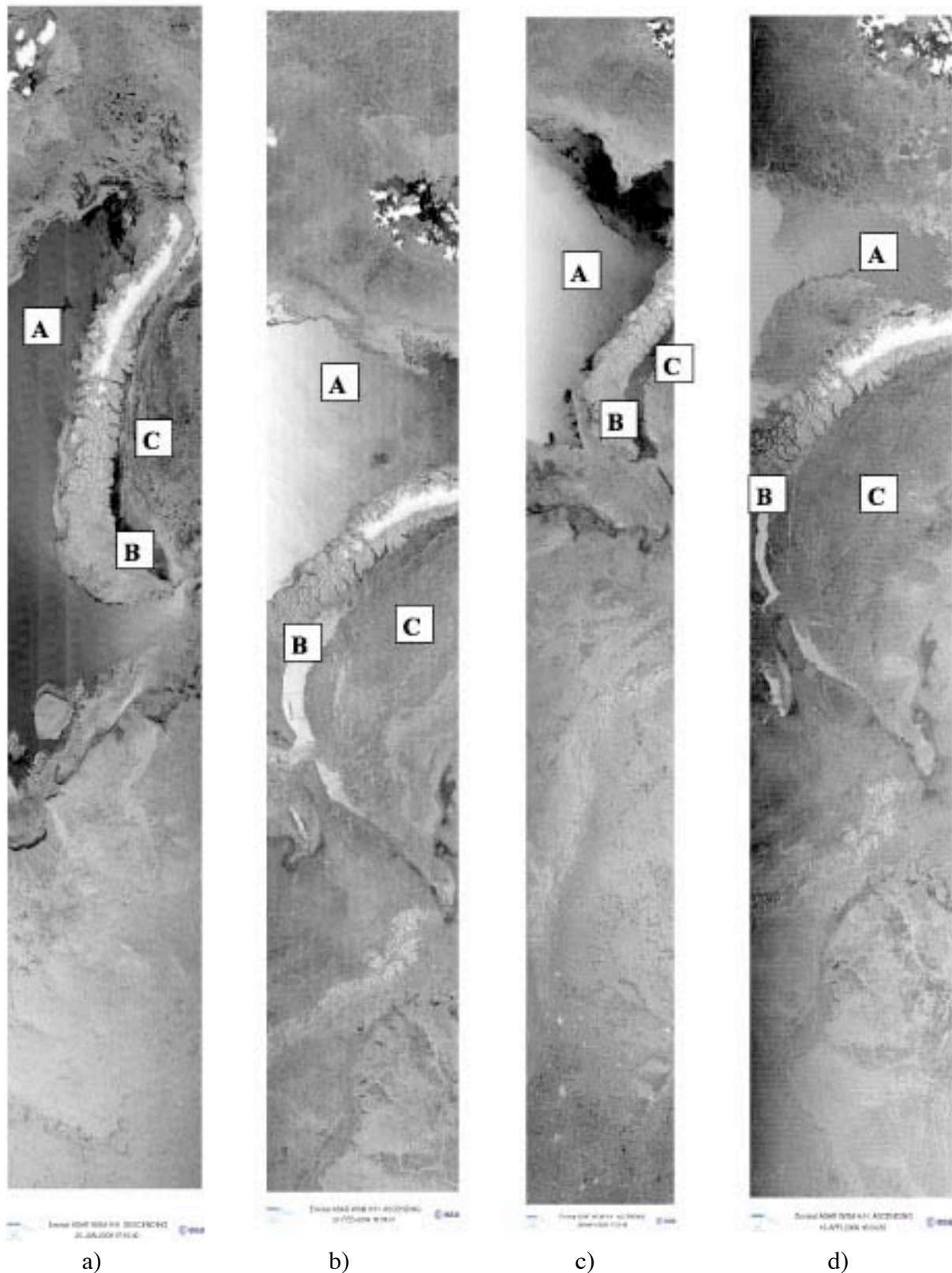


Figure 2.1. Polynya formation near the southeastern coast of Novaya Zemlya from ENVISAT ASAR images: a) 23.01.2009, b) 21.02.2009, c) 08.03.2009, d) 13.04.2009.

A – open water; B – polynya; C- drifting ice in the south-western Kara Sea.

2.2 Pre-processing of SAR images

The angular dependence of sea ice backscatter coefficient (σ^0) causes significant decrease of SAR image brightness as function of increasing incidence angle. To correct for this effect, the angular dependencies of young, first-year and multiyear ice were determined from calibrated ENVISAT ASAR images. The change in backscatter coefficient as function of incidence angle was found to be: 0.82 – 1.05 dB per $^\circ$ for wind-roughened open water, 0.14 – 0.20) dB per $^\circ$ for young ice, 0.18 – 0.42 dB per $^\circ$ for first-year ice, and 0.16 – 0.24 dB per $^\circ$ for multiyear ice.

The following procedures of ENVISAT ASAR image pre-processing were developed in order to improve and simplify their visual interpretation: recalculation of the backscatter coefficient to pre-defined incidence angle and automated processing of SAR mosaics from multiple satellite passes.

The procedure of angular correction of ENVISAT ASAR images, namely recalculation of σ^0 values from calibrated ENVISAT ASAR image to pre-defined incidence angle (25°) includes recalculation of SAR image brightness to σ^0 for current incidence angle, recalculation of this value to σ^0 for 25° incidence angle and recalculation of corrected σ^0 to corrected image brightness. An ENVISAT ASAR image of multiyear sea ice in the Greenland Sea for 15.01.2006 is shown in Fig. 2.2a. The 0.2 dB per $^\circ$ coefficient was used in the calculations. The same image after processing has approximately equal contrast in the near- and far-ranges, which significantly simplifies its interpretation (Fig. 2.2b).

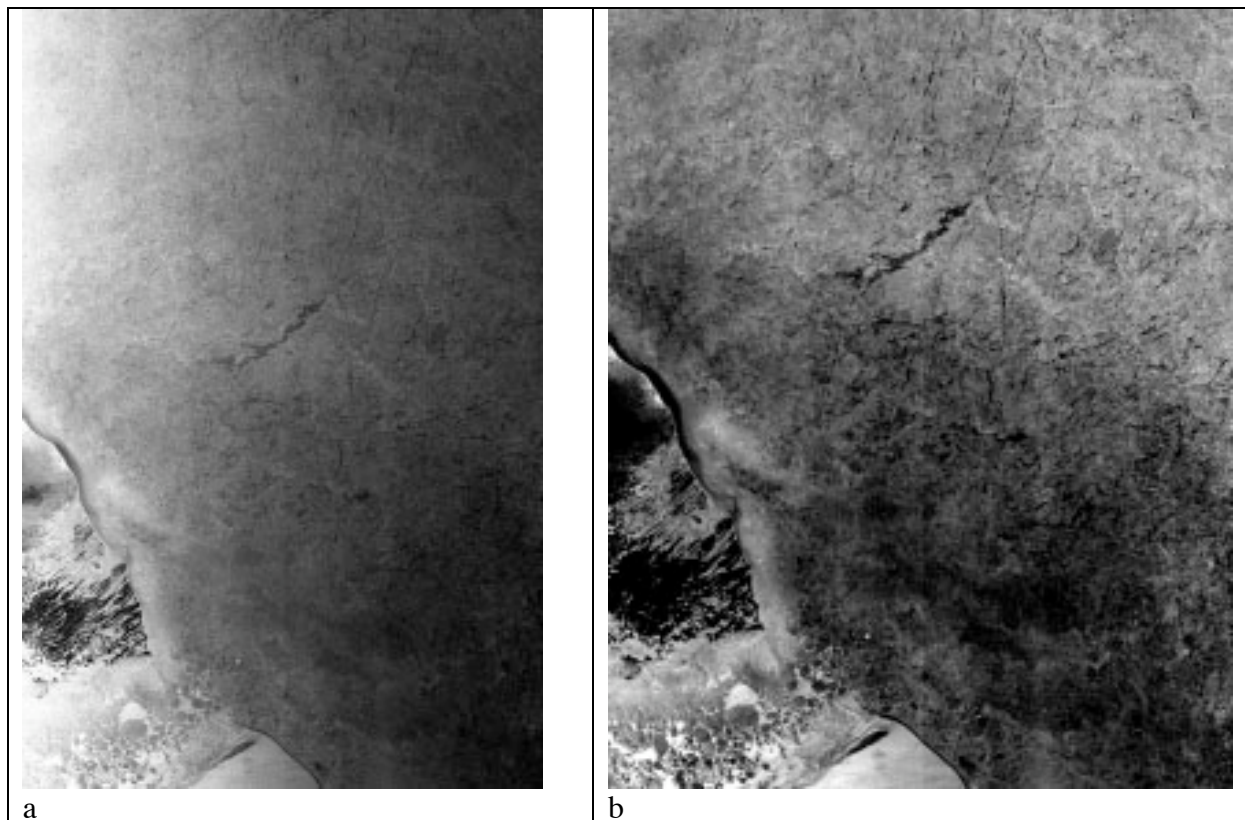


Figure 2.2. Angular correction of calibrated ENVISAT ASAR WS image to 25° incidence angle; a) ENVISAT ASAR WS image for 15.01.2006, covering the Greenland Sea, b) the same image after correction for incidence angle.

The composite ice charts are based on several images received at different satellite passes. These charts usually cover large areas, for example the entire Arctic Ocean or its parts. Preparation of such charts has several uses: 1) the need for a regular (e.g. 5-days) monitoring of the ice conditions, 2) for study of ice conditions over large area, 3) for obtaining initial data for ice forecasting, and 4) for climatic studies.

The procedure of automated processing of SAR mosaics from ENVISAT ASAR stripes from ESA rolling archive includes selection of SAR images, processing of mosaics using ESA "BEST" software including overlaying grid of geographical coordinates, and making annotations (ice types, geographical names etc.) using Adobe Photoshop. An example of such mosaic is presented in Figure 2.3, showing the coverage of ASAR images from ENVISAT during a 10-day period.

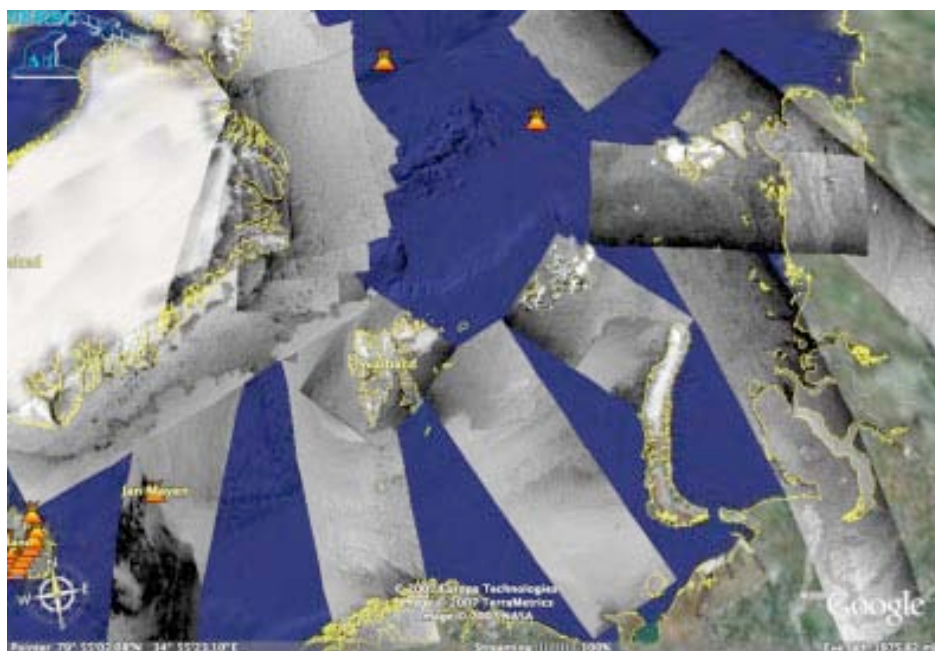


Figure 2.3. Mosaic of ENVISAT ASAR quicklook images of the European sector of the Arctic for a period of 10 days in February 2007. Note that the quicklook images are not corrected for incidence angle.

2.3 SAR ice classification and ice concentration - Neural network approach

2.3.1 Algorithm description

For fast and objective classification of sea ice types from Envisat ASAR images it is necessary to develop automatic processing techniques. In order to perform automatic classification of sea ice types in SAR images we have developed artificial Neural Network (NN) approach using textural characteristics. The NN approach includes a parallel divided

structure of information processing composed of the elementary *units*, which are connected via directed weighted links (*weights*), accumulate experimental data and give it to the processing (Bishop, 1995).

A feed forward NN contain an input layer, an output layer, and at least one hidden layer (Fig. 2.4). The layer of input neurons receives the data either from input files or directly from electronic sensors in real-time applications. The output layer provides information about the classification results. Between these two layers can be many hidden layers. These internal layers contain many of the neurons in various interconnected structures. The inputs and outputs of each of these hidden neurons go to other neurons, and are used in the classification scheme.

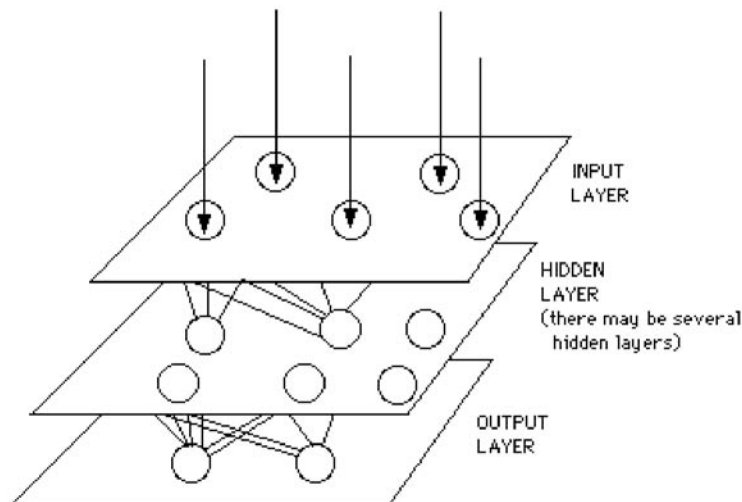


Figure 2.4. A Simple Neural Network Diagram

One of the major advantages of neural nets is their ability to generalize based on a set of classified training data. This means that a trained net could classify data from the same class as the learning data. In real world applications developers normally have only a small part of all possible patterns for the generation of a neural net. To reach the best generalization, the dataset should be split into three parts:

- The training set is used to train a neural net. The error of this dataset is minimized during iterative training.
- The validation set is used to determine the performance of a neural network on images that are not used during training.
- A test set for finally checking the over all performance of a neural network algorithm.

For implementing automated sea ice classification in ASAR images the structure of the NN was optimized. The standard product for ASAR Wide Swath Mode images (WSM) with 150-m resolution and width approximately 400 km were used for processing. Before making NN classification it is important to have similar backscatter coefficient for similar ice (and water) surfaces independent of incident angle (see chapter 2.2). For sea ice backscatter, the data are normalized using calibrated backscatter values normalized to a fixed incidence angle. The

ASAR images were calibrated using software developed in NIERSC that include incidence angle correction. The output image may have either a linear or dB scale (Fig. 2.2b).

For realization of the Neural Network approach we use Stuttgart Neural Network Simulator (SNNS), developed at the Institute for Parallel and Distributed High Performance Systems at the University of Stuttgart. Two principles can be applied: one is to use calibrated backscatter values for each individual pixel, and the other is to use textural information in the image. The first principle requires knowledge about the relationship between SAR backscatter value and ice/surface characteristics. Such relations have been established through a series of validation experiments, including MONRUK studies. Textural classification can be used as a supplement to backscatter levels.

The number of units at the input layer corresponds to the number of image characteristics. As the inputs we used backscatter values and texture of ASAR images. Textural image characteristics were computed based on Grey Level Co-occurrence Matrix (GLCM). GLCM describes the frequency of one gray tone (backscatter values) appearing in a specified spatial linear relationship with another gray tone, within the investigation area. Seven textural parameters are considered to be most relevant using GLCM: *energy*, *correlation*, *inertia* (or *contrast*), *entropy*, *homogeneity*, *inverse difference moment*, *cluster prominence*, and also 3rd and 4th *statistical moments*. Passing through the network the input vector is reorganized into the resulting vector in the NN output. The number of units at the output layer corresponds to the number of the qualified sea ice type classes.

The neural networks have been trained with supervision. The learning method tries to minimize the current errors of all processing elements. This global error reduction is created over the time by continuously modifying the input weights until acceptable network accuracy is reached. As learning classes we use the following ice classes: first year ice, rough first year ice, and multiyear ice. As a result it is supposed to find the following ice classes: first year ice (FY), young ice and multiyear ice (MY). NN was used for classification of series of ENVISAT ASAR images after training. The results of ASAR image classification are presented below.

2.3.2 Examples of sea ice classification

We have applied and tested the above NN sea ice classification algorithm to analysis of sea ice conditions in Central Arctic (North Pole - 35 (NP-35) area). Fig. 2.5 demonstrates results of classification of ASAR image for January 18, 2008. During the NN training first-year ice areas with a degree of deformation less than 2 (Russian scale) were interpreted as “level first-year ice”, and more than 3 – to deformed first-year ice. The classification results show a large amount of deformed first-year ice (blue colour), which corresponds to thick first-year ice, according to visual analysis. Several zones of level first-year ice were classified erroneously as fractures. In order to distinguish between “calm open water/nilas” and “level first-year ice” classes a new NN was trained. According to preliminary estimates the multiyear ice and “calm open water/nilas” were then classified correctly. Significant part of the image was identified as area of strongly deformed first-year ice and areas of level and thin first-year ice were classified as “level first-year ice” class. Therefore it was decided to use two NNs: first, to distinguish between level and deformed ice, and then to classify multiyear ice and “calm open water/nilas”.

As another example we have applied and tested this algorithm to analysis of sea ice conditions in Central Arctic (North Pole - 35 (NP-35) area – red triangle). Fig. 2.6 demonstrates results of classification of ASAR image for February 04, 2008. During the NN training first-year ice areas with a degree of deformation less than 2 (Russian scale) were interpreted as “level first-year ice”, and more than 3 – to deformed first-year ice. The classification results shows a large amount of deformed first-year ice (blue color), which corresponds to thick first-year ice, according to visual analysis. Significant part of the image was identified as area of strongly deformed first-year ice and areas of very level and thin first-year ice were classified as “level first-year ice” class. Several zones of multiyear ice were classified erroneously as level first-year ice. According to the visual analysis a zone of multiyear ice is quite huge (very light color on lower ASAR image), but on the NN classification result image (upper) it is mixed with strongly deformed first-year ice.

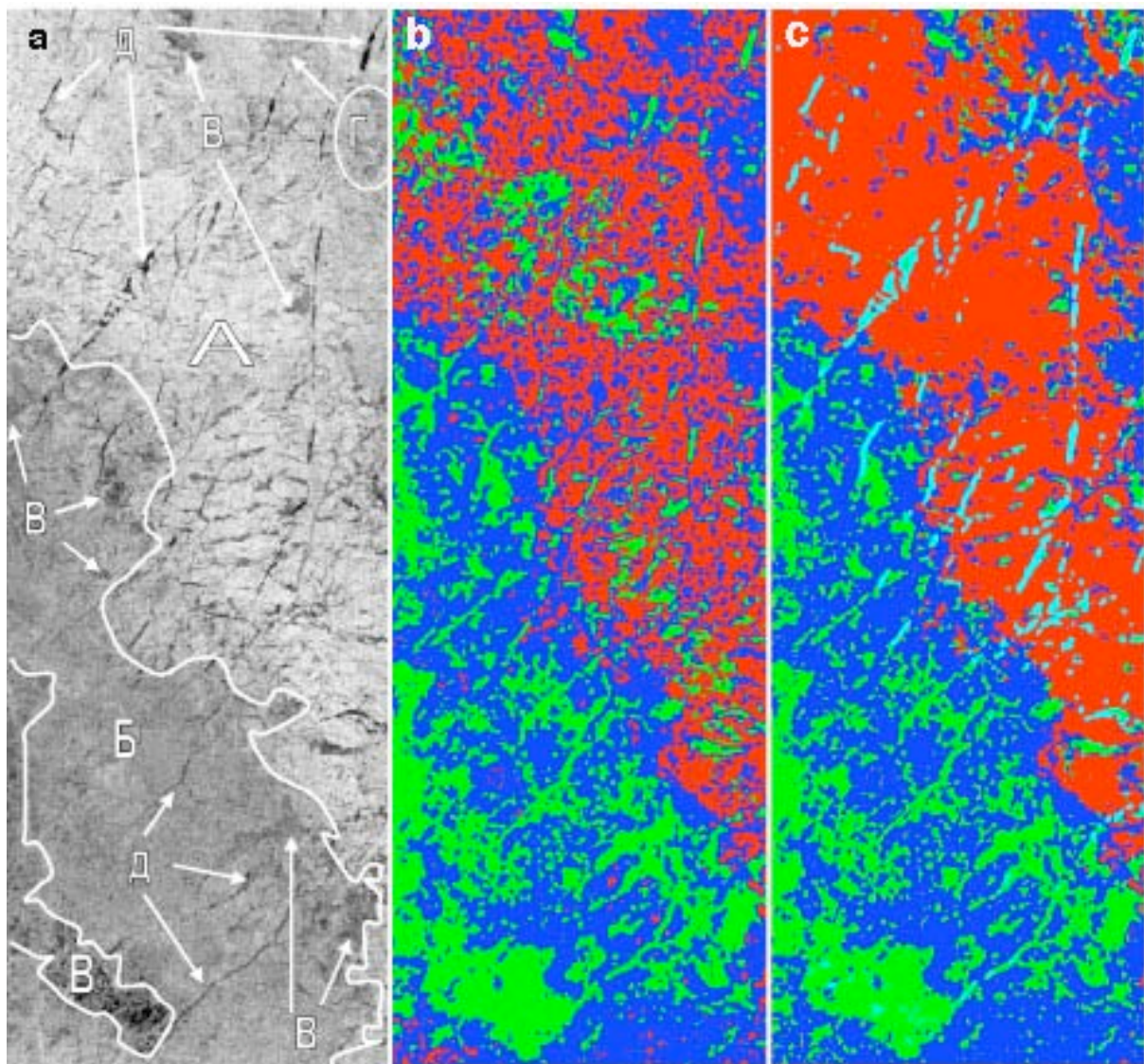


Figure 2.5. a). Envisat ASAR backscatter image for 23.04.2007 b) Classified image after first step, c) Classified image after two sequential steps of NN. Colors of classified images: Red – MY-ice, blue – FY deformed ice, green – level FY-ice; light blue – calm open water/nilas.

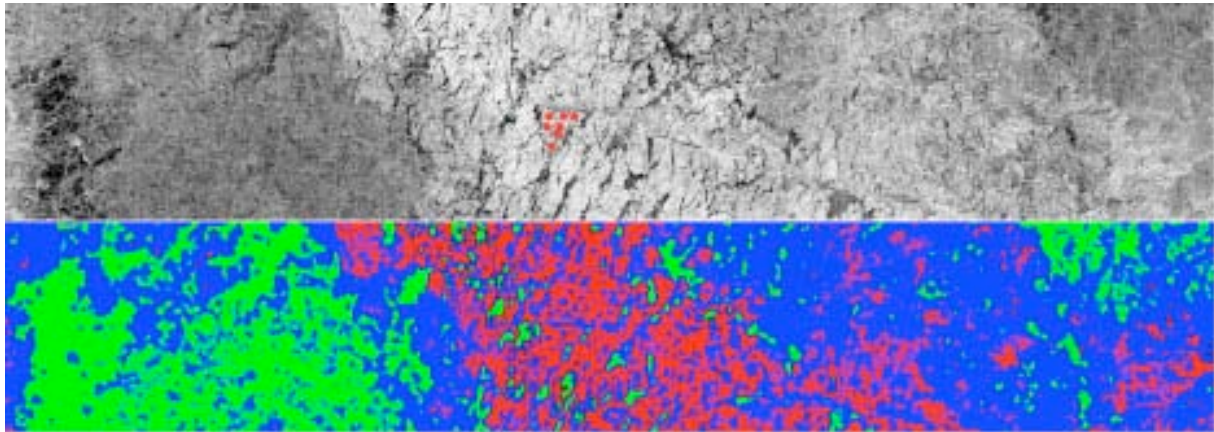


Figure 2.6. ENVISAT ASAR image, 04 February 2008, Central Arctic, (red points on gray tone image shows location of NP-35). Colors of classified image (lowest): green – FY level ice, blue – FY deformed ice, red – MY ice.

2.3.3 Status of the NN algorithm

During the project the NN algorithm of sea ice classification, including a stage of pre-processing, have been developed and tested on a few examples of SAR ice images. The stage of pre-processing includes ASAR image calibration and recalculation of sea ice backscatter to pre-defined incidence angle. The algorithm of automated sea ice classification uses pixel-based approach. The image features used in the classification are sea ice backscatter and textural characteristics. Test of the algorithm show reasonable results in classification of sea ice types: multiyear, level and deformed first-year and nilas. In order to use this algorithm in operative mode it is necessary to test it for different ice types in different Arctic regions. Future work will also include elaboration of region-based approach to classification, using parameters of segment form in classification, as well as using multipolarization images.

2.4 SAR ice classification/MY-ice concentration - Bayesian approach

2.4.1 Algorithm description

A second algorithm of sea ice classification uses the Bayesian approach, interactive delineation of zones of different partial concentration of multiyear ice and calculation of multiyear ice concentration within the boundaries of delineated polygons. Bayesian classification make decision for the ice type with a maximum a posteriori probability $p(\omega_j/x_i)$, which is calculated as:

$$p(\omega_j / x_i) = p(x_i / \omega_j) \times p(\omega_j) / p(x_i),$$

$$p(x_i) = \sum_{j=1}^N p(x_i / \omega_j) \times p(\omega_j), \text{ where}$$

$p(\omega_j)$ – apriori probability, $p(x_i/\omega_j)$ – conditional frequency distribution of value x_i for class ω_j .

In order to implement the Bayesian classification it is necessary to estimate the conditional probabilities of sigma-0 for different ice types and their a priori probabilities. Conditional probabilities were calculated from calibrated ENVISAT ASAR images. The partial concentration of MY-ice in the Central Arctic amounts to 90% (Johannessen et al., 2006). The following a priori probabilities were selected for MY-ice, level and deformed FY-ice: $p(\omega_{my})=0.9$; $p(\omega_{fy})=0.05$, $p(\omega_{fd})=0.05$.

The algorithm implementation includes the following steps:

- SAR image calibration, its angular correction, and masking land areas (see chapter 2.2),
- Pixel-by-pixel classification by means of calculating $p(\omega_j/x_i)$ for multiyear, level and deformed FY-ice, finding its maximum value, and labeling pixel as ice class, corresponding to this maximum value,
- Interactive delineation of visually homogenous areas and calculation of partial concentrations of MY-ice, level and deformed FY-ice for delineated areas.

2.4.2 Examples of sea ice classification using Bayesian algorithm

Examples of algorithm assessment are presented in Fig. 2.7 and 2.8.

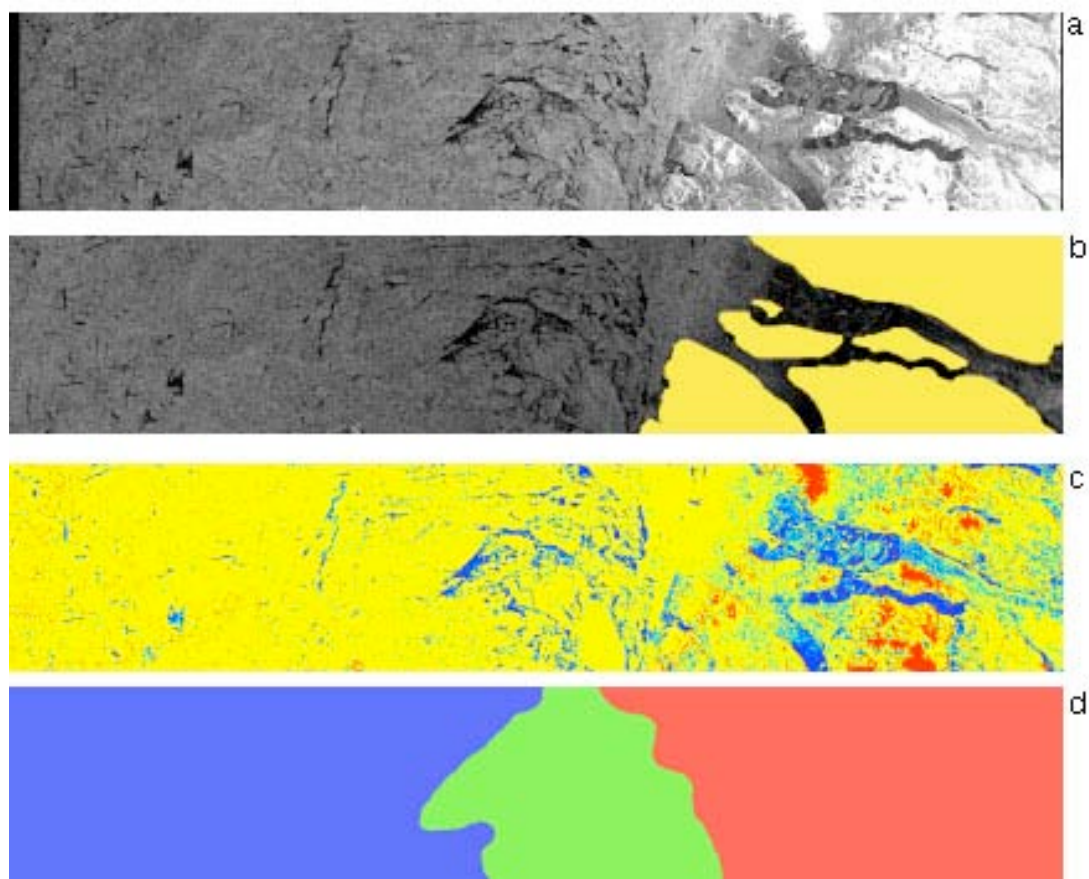


Figure 2.7. Retrieval of multiyear ice concentration in the Central Arctic based on Bayesian classification of ENVISAT ASAR images. Three areas in this image were delineated by expert. Within the delineated areas the partial concentrations of the multiyear, level first-year and deformed first-year ice are the following: blue - $C_{fy}=0.016$, $C_{fyd}=0.02$, $C_{my}=0.95$; green - $C_{fy}=0.12$, $C_{fyd}=0.07$, $C_{my}=0.81$; red - $C_{fy}=0.21$, $C_{fyd}=0.15$, $C_{my}=0.62$.

The original ENVISAT ASAR image is shown in Fig. 2.7.a. the calibrated image after implementation of angular correction and masking land areas is shown in Fig. 2.7.b. The results of its Bayesian pixel-by-pixel classification are shown in Fig. 2.7c, where yellow corresponds to multiyear ice, blue – to FY-ice, light blue – to deformed FY-ice, and red is unclassified. Fig. 2.7d shows three areas, delineated by expert, for which partial concentrations of MY-ice (C_{my}), level FY-ice (C_{fy}), and deformed FY-ice (C_{fyd}) are calculated.

The image in Fig. 2.8 is homogenous and partial concentrations of these ice types were calculated for the whole image. The results of automatic classification and multiyear ice concentration retrieval correspond to visual expert estimates. The results of classification and calculation of partial ice concentration of the multiyear, level first-year and deformed first-year ice correspond rather well to expert estimates and the difference between estimates does not exceed several per cent.

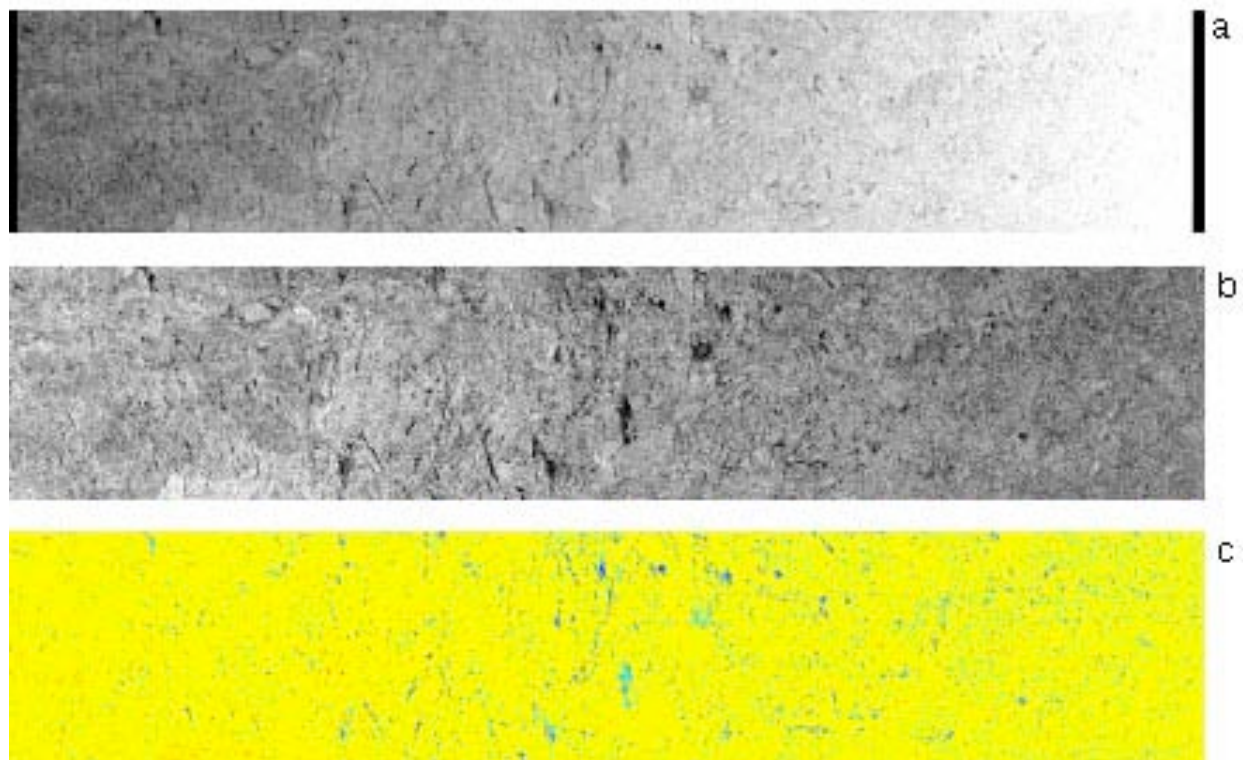


Figure 2.8. Retrieval of multiyear ice concentration in the Central Arctic based on Bayesian classification of ENVISAT ASAR image: a: uncorrected image, b: corrected for incidence angle, c: classification result, where yellow is multiyear ice, level first-year ice is green/blue, and deformed first-year ice is red. The partial concentrations of the multiyear, level first-year and deformed first-year ice are the following: $C_{my}=0.9437$; $C_{fy}=0.013$; $C_{fyd}=0.0416$.

2.4.3 Status of the algorithm

The Bayesian algorithm of automated sea ice classification uses pixel-based approach. The algorithm was tested in the Central Arctic, where MY-ice dominates. It shows reasonable results, which correspond to expert estimates. For estimation of MY-ice partial concentration

different areas are delineated in the image in interactive mode, and then MY-ice concentration is calculated for each area. Using region-based approach allows better segmentation of different ice features, such as leads and areas of FY/young ice. After that classification of delineated segments can be done. Improvement can be achieved by using parameters of segment form in the classification. Using this algorithm in operative works need further validation and improvement.

2.5 Ice drift retrieval

2.5.1 Algorithms description

The algorithms of ice drift retrieval from SAR images are under investigation. SAR images of sea ice captures two important characteristics of ice floe advection and differential non-rigid motion. Under these conditions retrieval of sea ice motion can be split on two stages:

- Estimation of large-scale rigid motion and, specifically in this case, the overall translation or/and rotation of features between SAR image pairs.
- Estimation of local translational component of the piece-wise continuous movement of granules or plates and affine motion includes the linear, non-translational components of motion.

At present time, cross-correlation based approach is used at NERSC for estimation of first type of motion, since this technique is capable of measuring very large shifts of many tens of pixels (Johannessen et al., 2007). The software for this approach was installed at NIERSC and algorithm was tested using a number of ENVISAT ASAR image pairs. Initial version of cross-correlation algorithm uses the binary search procedure in order to minimize computation time. Using this procedure assumes that the cross-correlation coefficient between two blocks in successive satellite images monotonically decreases with increasing distance in some area near the selected object (Fig. 2.9a). Comparison of automatically-derived ice drift vectors with manually derived vectors revealed several errors in ice drift retrieval. The program for visualization of correlation coefficient between blocks of pixels was written in order to analyze the algorithm performance. Analysis of obtained scatterplots revealed several peaks in spatial distribution of cross-correlation coefficient (Fig. 2.9b). Therefore the binary search procedure for finding maximum cross-correlation coefficient does is not appropriate for SAR images.

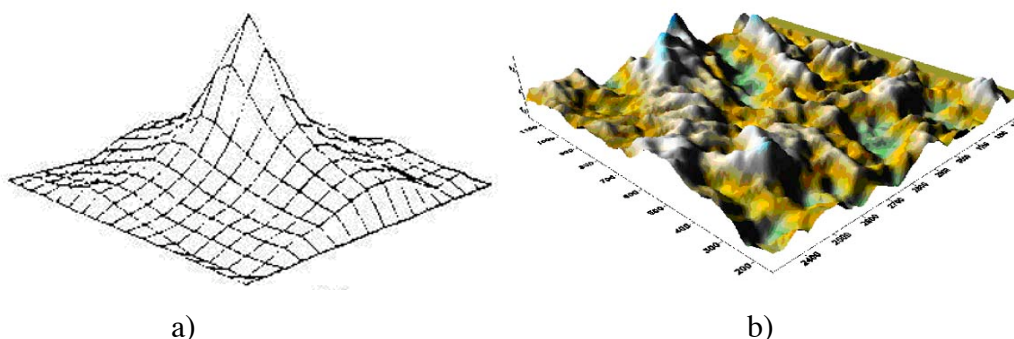


Figure 2.9. Cross-correlation coefficient of image blocks in the surroundings of selected object: a – assumed variations; b – real variations, calculated from ENVISAT ASAR image.

Due to this we limited search area as a maximum ice displacement for the period between image acquisitions taking into consideration maximum possible ice drift velocity.

2.5.2 Examples of ice drift retrieval

The results of ice drift retrieval using the cross-correlation algorithm on two SAR images in the northeastern Barents Sea is shown in Fig. 2.10. The ice drift vectors are overlaid on the pair of ENVISAT ASAR images as white arrows where the dots represent the end of the vectors. The ice motion is to the west and there are a few erroneous vectors pointing in other directions. The vectors are calculated on a fixed, predefined grid. A validation of the algorithms can be done by comparing the vectors from the algorithm with vectors obtained by manual analysis and vectors obtained from other algorithms and input data. An example of validation data is shown in Fig. 2.11, taken from the same area and same period as Fig. 2.10. A qualitative comparison shows reasonable agreement between the algorithm results and the validation data, but there is need to validate the algorithm in many more cases to assess the performance under different ice conditions.

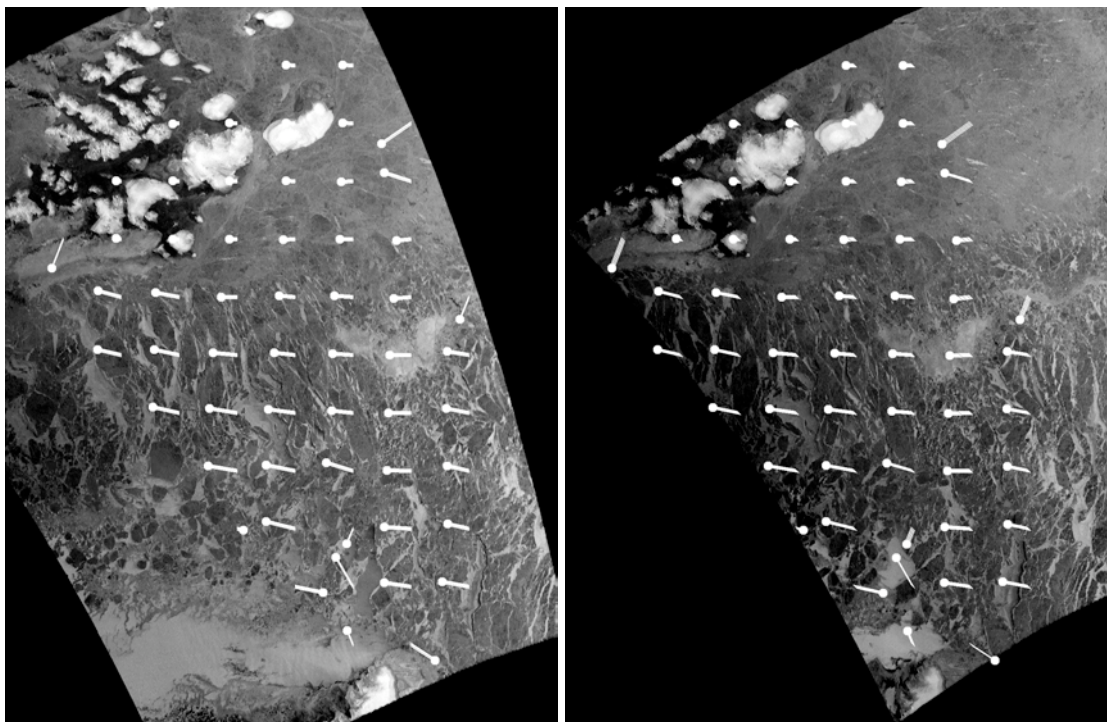


Figure 2.10. Ice drift vectors from ENVISAT ASAR images for March 31 and April 1, 2006 in the northeastern Barents Sea, using the cross-correlation method. The vectors represent the ice displacement between the first and the second image. The vectors are plotted by the start and end positions (marked by dots).

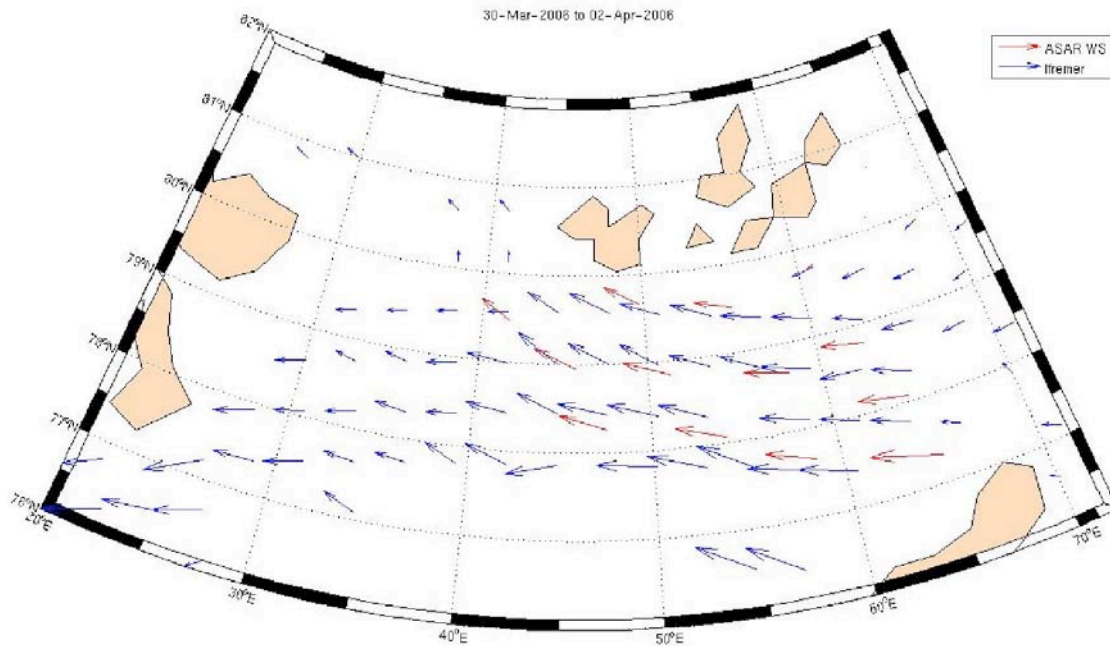


Figure 2.11. Ice drift retrieval from ENVISAT ASAR images using manual analysis (red vectors) and ice drift from scatterometer data provided by Ifremer (blue vectors) from 30 March to 02 April 2006.

2.5.3 Status of the algorithm

The algorithm is based on the assumption that the motion within a defined block is uniform, and vector field obtained from this algorithm present motion on scale larger than the block size. The algorithms performs well if used for images with well-defined ice features and for displacement smaller than the block size. There is considerable ambiguities in areas where the ice features are less well-defined, such as in the marginal ice zone. The vectors produced by the algorithm need to be filtered and quality controlled before they can be considered to be accurate. There is ongoing work at NERSC and NIERSC to develop other algorithms for ice drift retrieval from SAR images.

3. SEA ICE ANALYSIS IN STORFJORDEN

Storfjorden southeast of Spitsbergen (76-79N, 16-26E) is an area normally covered with sea ice in wintertime. However, due to prevailing conditions of winds from N/NE this ice is blown south creating a polynya which can vary quite a lot in size. Since the water in the polynya is unprotected from the cold atmosphere, new ice swiftly forms and is transported away with the winds. This makes Storfjorden is also interesting area for testing ice classification tools, since all ice types from open water and frazil ice to meter thick first year ice normally are present in and near the polynya.

3.1 *Time series of SAR and optical images*

To study the polynya through entire winters, over several seasons SAR images from ENVISAT was downloaded from the NERSC SAR archive, calibrated and projected into a polar stereographic projection. SAR images have two advantages; one is that they are not dependent of daylight, so they can follow the freezing process in December to February. The radar can “see” through clouds and clear weather or daylight is therefore not necessary to get useful data. One disadvantage is that a SAR sensor only sees differences in roughness, so an open water polynya with calm water is not possible to distinguish from the same polynya with e.g. 10 cm of smooth nilas. Optical satellite images can however easily distinguish these types, as shown in Figure 3-1. Satellite images from MODIS on the Terra and Aqua satellites are therefore also downloaded from when daylight and cloud conditions allows them to map Storfjorden from late February until most ice has melted in late June.

Studies of the data set showed that in 2007 a stable ice cover formed in mid February. A very large polynya formed between the 7th and 19th of March. It was frozen again on the 22nd. In general over the season from January to June a southward ice movement is present, with a polynya forming on the west coast of Edgeøya and the mouth of the strait between Spitsbergen and Barentsøya. This polynya refreezes and the new ice is transported southwards. In 2008 the ice cover in Storfjorden formed earlier, already in early of January. The prevailing conditions were the same as in 2007 with a southward movement of ice, resulting in polynyas in the same areas with refreezing and southward transport of the new formed ice.

Ice drift vectors were acquired manually for a period in March 2007. However, due to the thin ice in Storfjorden and deformation due to the normally present southward transport of ice. The SAR signatures of sea ice in Storfjorden can be very fuzzy without clearly observable ice features. It can therefore be very difficult to retrieve ice motion from SAR data, both by use of automated algorithms and manual analysis. When there are several consecutive days of cloudfree conditions, it is also possible to obtain ice drift vectors from MODIS images. Example of this is shown in Fig. 3-2.

3.2 *Combined analysis of SAR, optical and IR data*

Since SAR data alone can give ambiguous information about the ice types and open water in a polynya area, it can be advantageous to merge SAR with optical and IR data. The optical data, for example provided by MODIS, gives information about the surface albedo. In areas of variable ice thickness the albedo varies significantly between open water (very low

albedo), thin ice and thick ice with snow cover (very high albedo). In addition the from the near-infrared channel gives data on surface temperature, which also varies significantly between open water and ice of varying thickness. Figure 3-3 shows an example of merging of SAR and IR images in Storfjorden area.

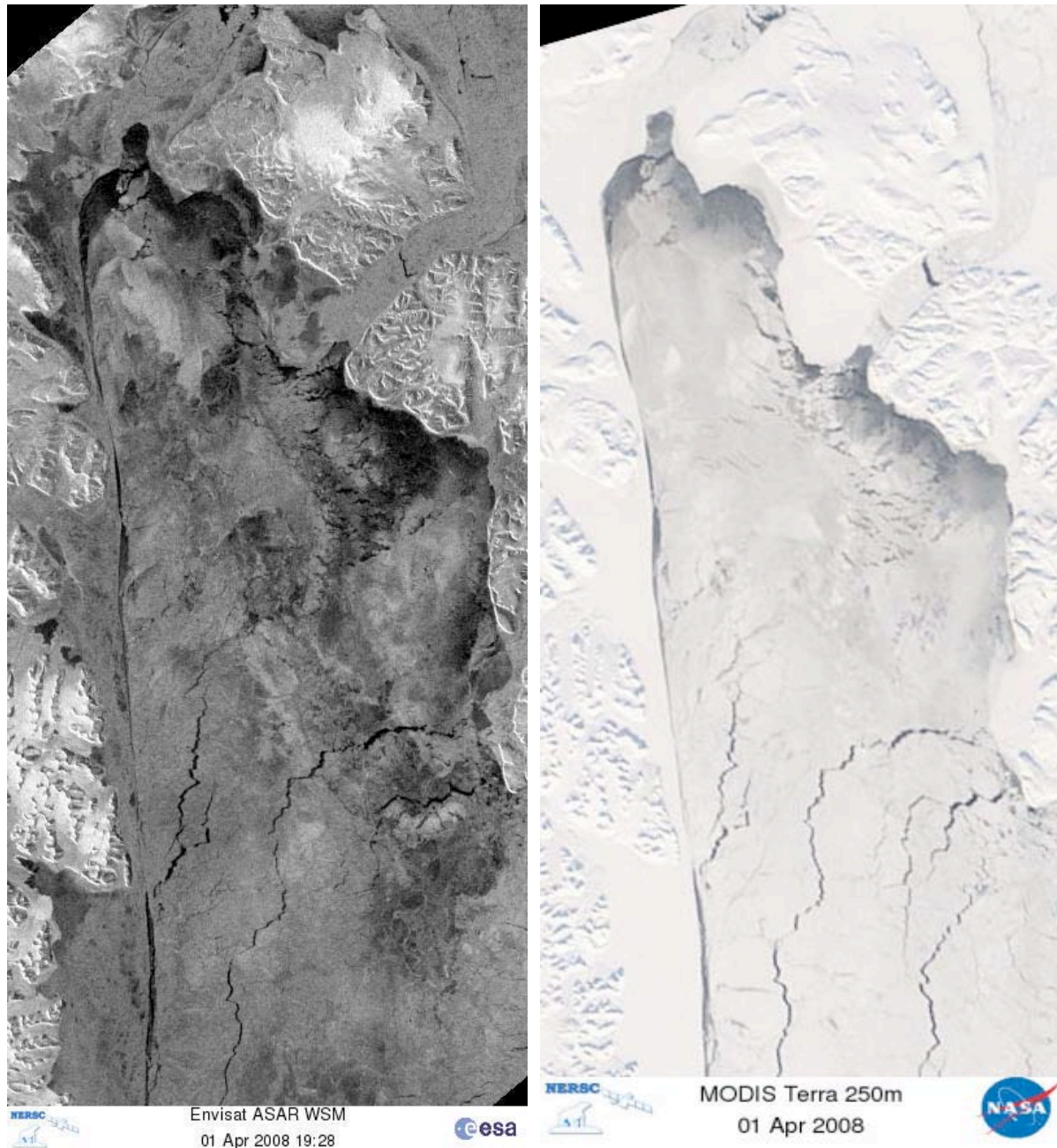


Figure 3.2: Storfjorden on the 1st of April 2008 seen from the ENVISAT ASAR (left) and the Terra MODIS (right). On the MODIS image it is clear that polynya consists of thin, young ice with some small leads with open water, identified as darker signature than the thicker, snow-covered ice. Both images identifies the polynya by dark signature. The SAR image has much more variable signatures where low backscatter can represent both thin ice (nilas) and undeformed firstyear ice.

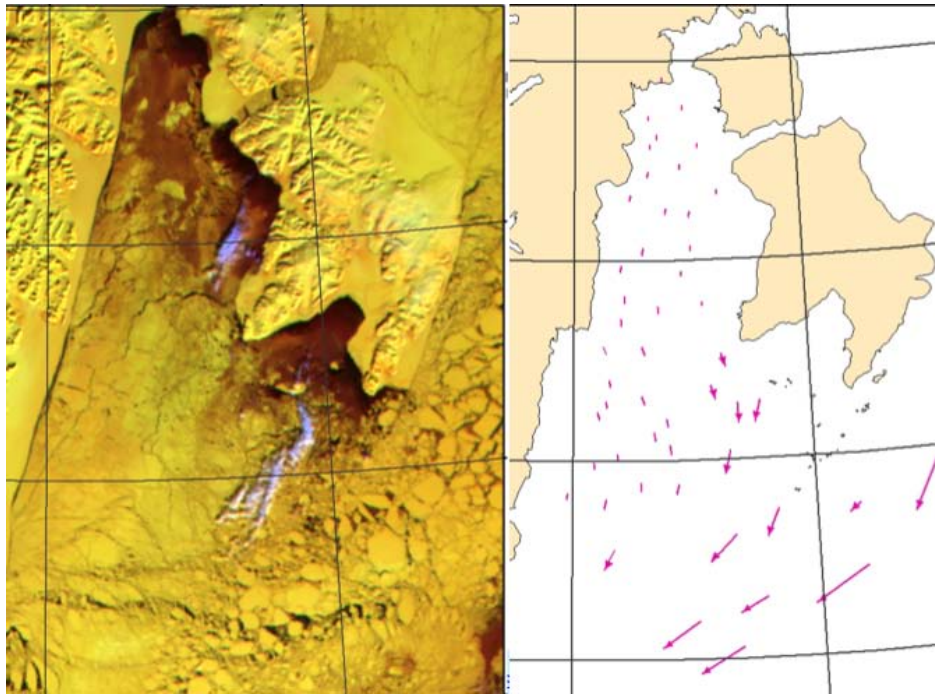


Figure 3-2. The left figure is a three channel composite of a MODIS sub-image covering the Storfjorden area on 01 April 2008. By combining channel 2, 4 and 7, clouds become visible as blue, ice is yellow, and open water is dark. The right figure shows ice displacement vectors between 01 and 04 April 2008, derived from two MODIS images using manual analysis. The ice drift within Storfjorden is very small, while outside the fjord there is significant southwestward icedrift associated with the East Spitzbergen Current.

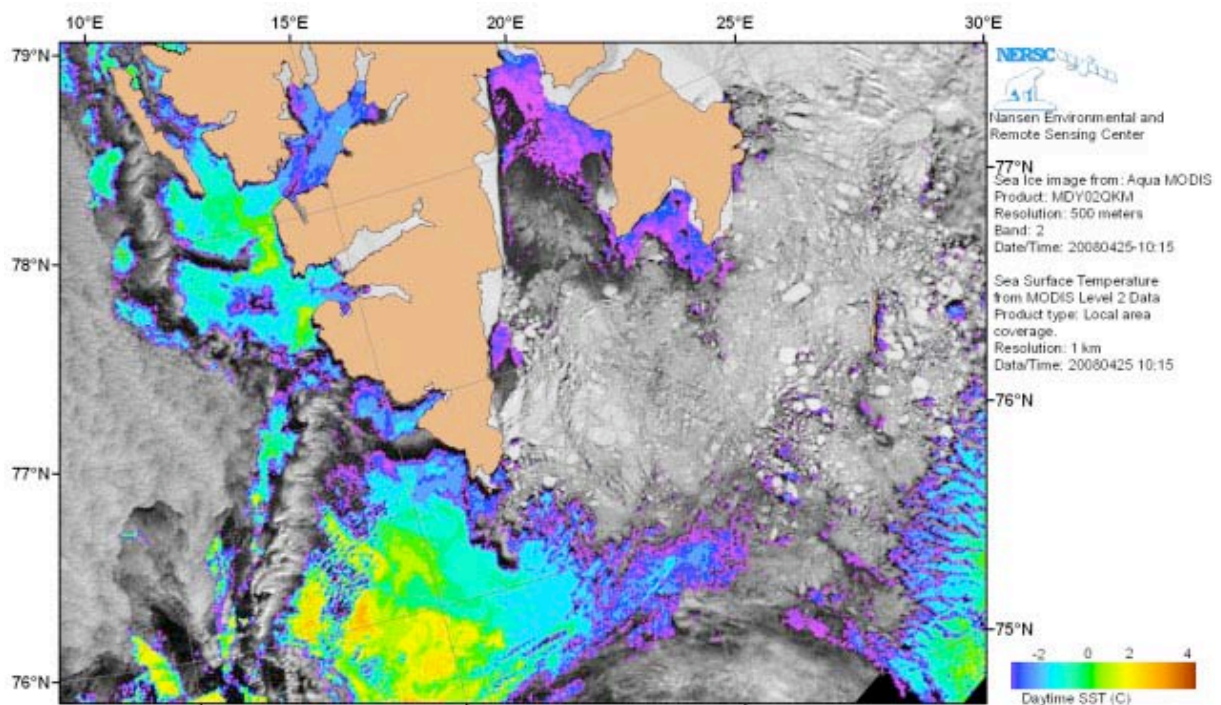


Figure 3-3. Merged SAR image (greyscale) with SST from MODIS (colours) from 25 April 2008. The part of the SST map not covered by cloud or landmask is superimposed on the SAR image. Thin ice has temperature slightly below freezing (blue-violet).

3.3 Sea ice thickness

Sea ice thickness is one of the main ice parameters, and improved observations of ice thickness is from satellites is needed both in climate studies and to support ice navigation and operation in ice areas. The fact that sea ice insulates the warm ocean from the cold atmosphere can be used to calculate ice thickness using the energy conservation equation, using sea surface temperature from satellites and other input data. This is used in the following to estimate ice thickness in Storfjorden, using the approach of Yu and Lindsay (2003), Drucker et al. (2003).

$$(1 - \alpha_s)F_r - I_0 - F_1^{up} + F_1^{dn} + F_s + F_e + F_c = 0$$

(1) (2) (3) (4) (5) (6) (7)

where

- (1) Net solar radiation at the surface, where F_r is in coming shortwave solar radiation and α_s is surface albedo. F_r is estimated using empirical relation for clear-sky conditions (Shine and Henderson-Sellers, 1985)
- (2) Solar radiation passing through the ice interior: $I_0 = i_0(1-\alpha_s)F_r$
- (3) Upward longwave radiation is $\epsilon\sigma T_s^4$ where ϵ is longwave emissivity of ice or snow surface, σ is Stefan-Boltzmann constant and T_s is surface temperature derived from AVHRR data
- (4) Downward longwave radiation is represented by several empirical relations which require surface air temperature, partial pressure of water vapour near surface and cloudiness. We use a mean AVHRR for surface air temperature
- (5) Turbulent sensible surface heat flux: $F_s = \rho_a c_p C_s u (T_a - T_s)$, where c_p is specific heat of air, C_s is bulk transfer coefficients for heat
- (6) Latent heat flux: $F_e = \rho_a L C_e u (e_{sa} - e_{s0})$, where L is latent of vaporization, C_e is bulk transfer coefficients for evaporation, e_{sa} saturation vapour pressure, and e_{s0} saturation vapour pressure at the surface. The surface wind speed u at 2 m above the ice/snow surface is $u = 0.34Ug$, where Ug is geostrophic wind from 12-hourly pressure fields from IABP.
- (7) Conductive heat flux: $F_c = \gamma(T_f - T_s)$ where γ is the thermal conductance of the ice/snow slab, T_f is the freezing temperature of sea water. Through several more steps salinity and ice thickness are included. Finally, the equation is solved for ice thickness.

Data has been analysed for the period March – April 2008, when a series of cloudfree days occurred in Storfjorden, allow analysis of several MODIS SST data sets.

An example of ice thickness retrieval is presented in Fig. 3-4 where the ice thickness data is merged with an ASAR image from ENVISAT. This image shows that the thickness derived from MODIS IR data catches larger leads and larger ice floes. The varying ice thickness in the polynya is presented in a very realistic way, where the thinnest ice near the coast of Edgeøya and Barnetsøya and the thickness increases further south in Storfjorden. Ice thicker than 0.7 m is not shown because it is assumed that the algorithms is not applicable for thicker ice.

Validation of the thickness retrievals can be done by other thickness measurements, obtained from drilling holes or use of airborne surveys with electromagnetic induction instrument. As can be seen in Figure 3-4, MODIS data can help in distinguishing thin and thick ice in a SAR image and could possibly be an additional tool for ice classification. However due its many restrictions, the method can only be used on cold clear weather days when the sun angle is

high. The data can nevertheless be very useful to calculate ice thickness in the winter time (February – April) in areas where other thickness data are scarcely available.

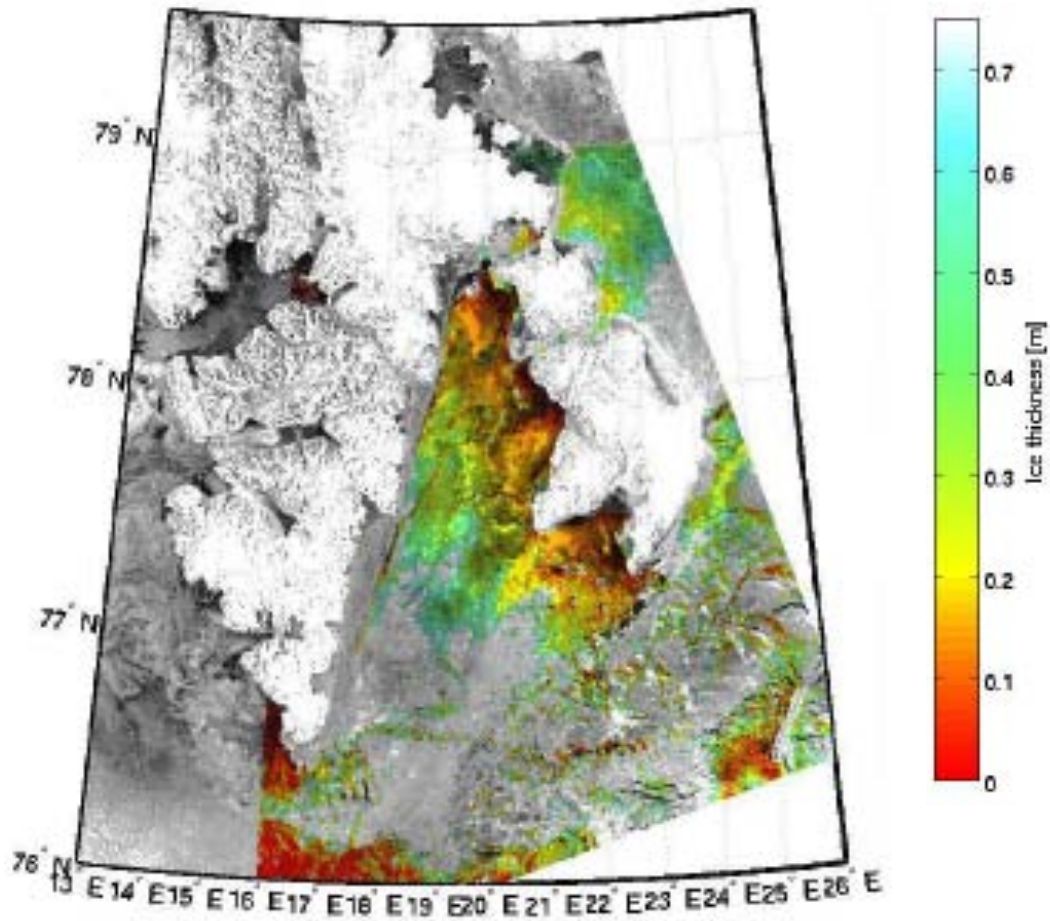


Figure 3-4. Ice thickness in Storfjorden derived from MODIS SST data on 01 April 2008. The colour indicates the area where thickness is retrieved, and the greyscale indicate the area covered by SAR image.

4. ICEBERG DETECTION IN FRANZ JOSEPH LAND

4.1 Introduction

In recent years the icebergs in the Barents Sea have become increasingly important because of changes in the cryosphere and the risk they impose on offshore operations and sea transportation. The icebergs in the Barents Sea originate from three main areas: Svalbard (in particular Nordaustlandet), Franz Josef Land and Novaya Zemlya (Fig. 4-1). The probability of finding icebergs is highest in Franz Josef Land area, with a mean annual probability occurrence above 80 %. The majority of the icebergs produced in these areas are small, typically 20 m (small icebergs, bergy bits and growlers) as shown in Fig. 4-2, while tabular icebergs, glacier bergs and other types at scales of 100 m or more represent a minority [Zubakin et al., 2004].

Aircraft surveys have been the main monitoring method for several decades, but during the 1990s the frequency of air survey has declined. Other observation methods include ship and polar station observations, but these have also declined in the last decade. Satellite observations have not been used regularly, but several research projects have demonstrated the possibilities to detect icebergs from satellite images. Satellites can mainly observe the largest icebergs, typically 100 m or more in horizontal extent, and under specific wind and sea ice conditions. Several studies have been conducted on detection of small-scale Arctic icebergs from satellite SAR data in eastern Canada, off the southern coasts of Greenland and in the northern Barents Sea. These studies present various techniques and algorithms to detect objects in SAR images that are most likely icebergs drifting in partly ice-covered and partly open water conditions.



Figure 4-1. Icebergs in the European sector of the Arctic are produced by calving from glaciers in Greenland, Svalbard, Franz Josef Land, Novaya Zemlya and Severnaya Zemlya

Iceberg observations in high resolution optical images are not hampered by the speckle noise which is characteristic for the SAR images. Observations in optical images are therefore more reliable for icebergs of size of 100 m or less. The limitation of optical images is cloud cover and darkness, allowing good quality observations only occasionally.

Iceberg signatures in SAR images are characterized by bright signature (high radar reflection from the iceberg) compared to a darker background of water or sea ice. The possibility to detect icebergs therefore depends on the iceberg properties (size, height, shape) as well as by the background (sea ice or open water). SAR backscatter from icebergs is caused by two main mechanisms: (1) backscatter from the top surface(s), and (2) backscatter from ocean surface and the sidewalls of an iceberg in case there is a well-defined wall facing the radar beam (denoted “double-bouncing”). Icebergs are detected in three different backgrounds, each requires a specific strategy for observation: (1) Icebergs located in open water will appear as bright spots against dark background in both optical and SAR images. During high wind speed the contrast between open water and icebergs is reduced in the SAR images. (2) Icebergs in drifting ice create open leads due to the different drift speed to surrounding sea ice. When grounded, icebergs can create long tracks in the drifting ice. It can be difficult to distinguish icebergs from the background ice both for optical and SAR images. (3) Icebergs in fast ice near calving areas can be readily observed in high-resolution optical as well as in SAR images due to their high backscatter compared to the level fast ice, if image resolution is sufficient. Icebergs can be stationary in the fast ice for a long time, making it possible to identify the same icebergs over several months. The present study will address the detection of icebergs in a fast ice situation.



Figure 4-2. Picture of an iceberg drifting in open ocean north of Svalbard. The iceberg is about 20 m long and 5 m above the sea level

4.2 Data and methods

Iceberg detection capabilities have been studied in a previous project (Sandven et al., 2006) using ENVISAT ASAR alternating polarisation images (AP), RADARSAT ScanSAR Narrow (SN) mode image and optical images from Landsat and Terra ASTER. The main objective was to demonstrate how synergetic use of SAR and optical images can improve the observation of icebergs in the Barents Sea region.

In this report we have evaluated the capabilities of Terra SAR-X image and ENVISAT ASAR alternating polarisation images for iceberg detection. Comparison between SAR and optical images has also been done. The first example is from June 2008 where a TerraSAR-X and an ENVISAT image were investigated for iceberg detection. The images are from the southern part of the Franz Josef Land archipelago (Figure 4.3). The specification of the images is given in Table 4.1.

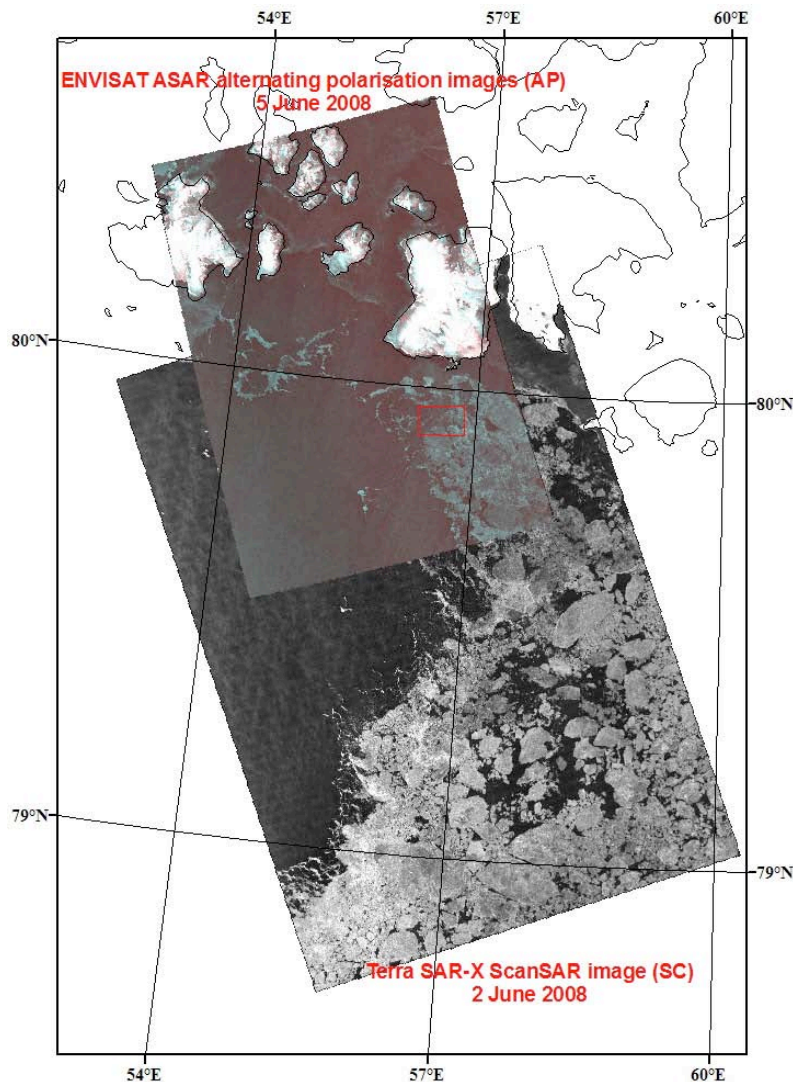


Figure 4-3 A map shows the ENVISAT ASAR (APP), acquired on 05 June 2008 and the Terra SAR-X image, acquired on June 2, 2008, in the Franz Josef Land area. The area in the red rectangle is zoomed-in and presented in Fig.4-4.

Table 4.1 Specification of SAR images used for iceberg detection

Satellite sensor	Image mode	Pixel size	Image size/ Swath width	Date/time
Terra SAR-X	ScanSAR (SC)	8.25m	106 X 150 km	June 02, 2008
ENVISAT ASAR	Alternating polarisation (HH- and HV polarisation)	12.5 m	73 X 106 km	June 05, 2008

The analysis of the images for detection of icebergs is based on identification of bright objects with well defined borders, but detection capability depends on the backscatter of the surrounding sea ice or open water. In this example the background is open water for the Terra SAR image (X-band) and sea ice for the ASAR image (C-band).

4.3 Data analysis

An area where the two images overlaps was selected for detailed analysis. A number of icebergs were identified in both images as bright spots against dark background (Figure 4.4). The changes in iceberg numbers and locations have been checked for both images. The same icebergs were detected in both images that were obtained with three day interval; suggesting that the icebergs in this area are grounded and therefore stationary. Comparison of the two images shows that the Terra SAR-X image is more suited in detection than the ASAR (AP) image in this situation. The reason can be higher resolution of the Terra SAR image, lower speckle noise and the fact that there was more sea ice present in the ENVISAT image. The HH polarization in the ASAR image was found to be better than the HV polarization for iceberg detection.

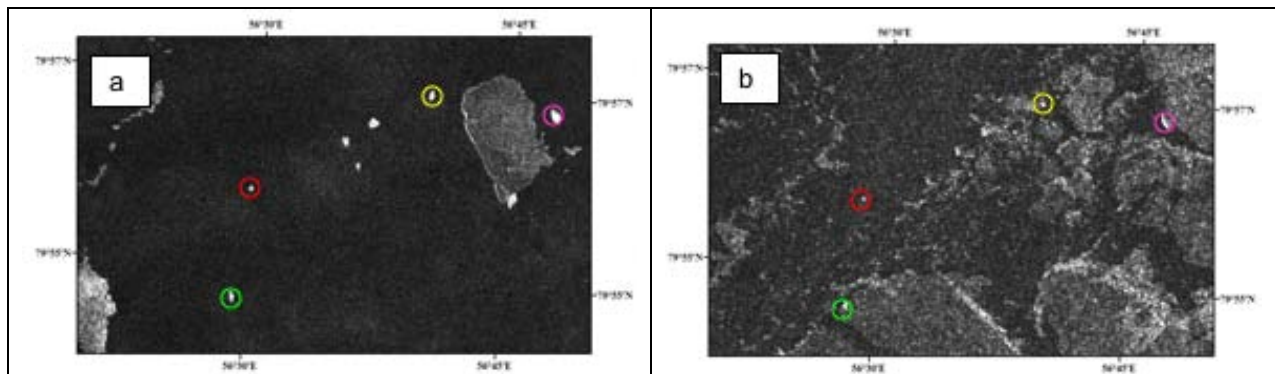


Figure 4.4 (a) subset of the Terra SAR-X image showing several icebergs marked by a coloured circle; (b) subset from the ENVISAT ASAR image covering the same area as in (a) where the same icebergs were identified.

4.4 Iceberg detection from Terra SAR-X

In this part we tested computer based iceberg detection; the method is based on image segmentation. The preliminary results are satisfactory for open water and fast ice, but for iceberg in sea ice more investigations are needed. Based on the same method the area and pixels values can be extracted for each iceberg (Table 4.2).

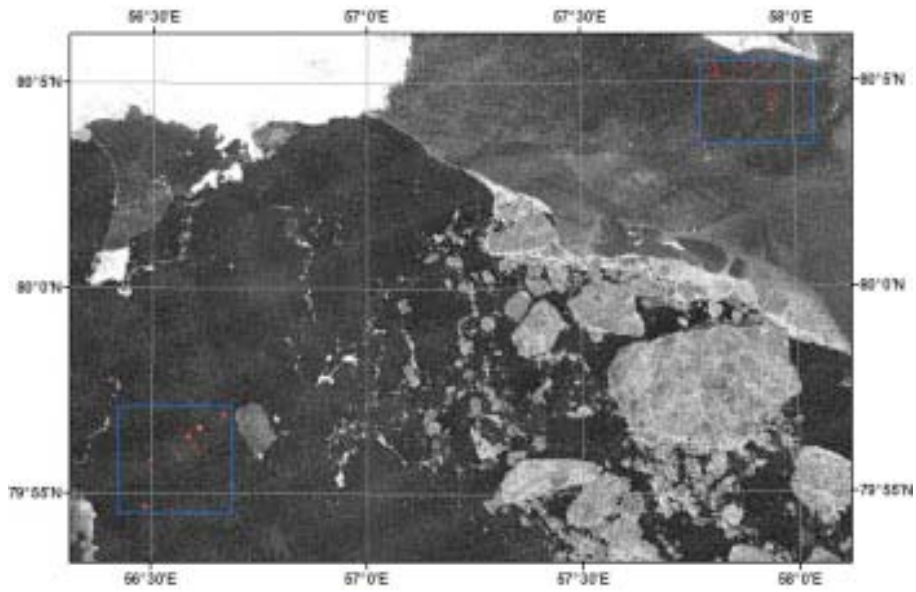


Figure 4-5 Part of the Terra SAR-X image showing an island (bright signature) and fast ice in the upper part and open water and drifting ice in the lower part. The blue rectangles show 2 areas where computer based identification was applied and presented in Fig 4-6.

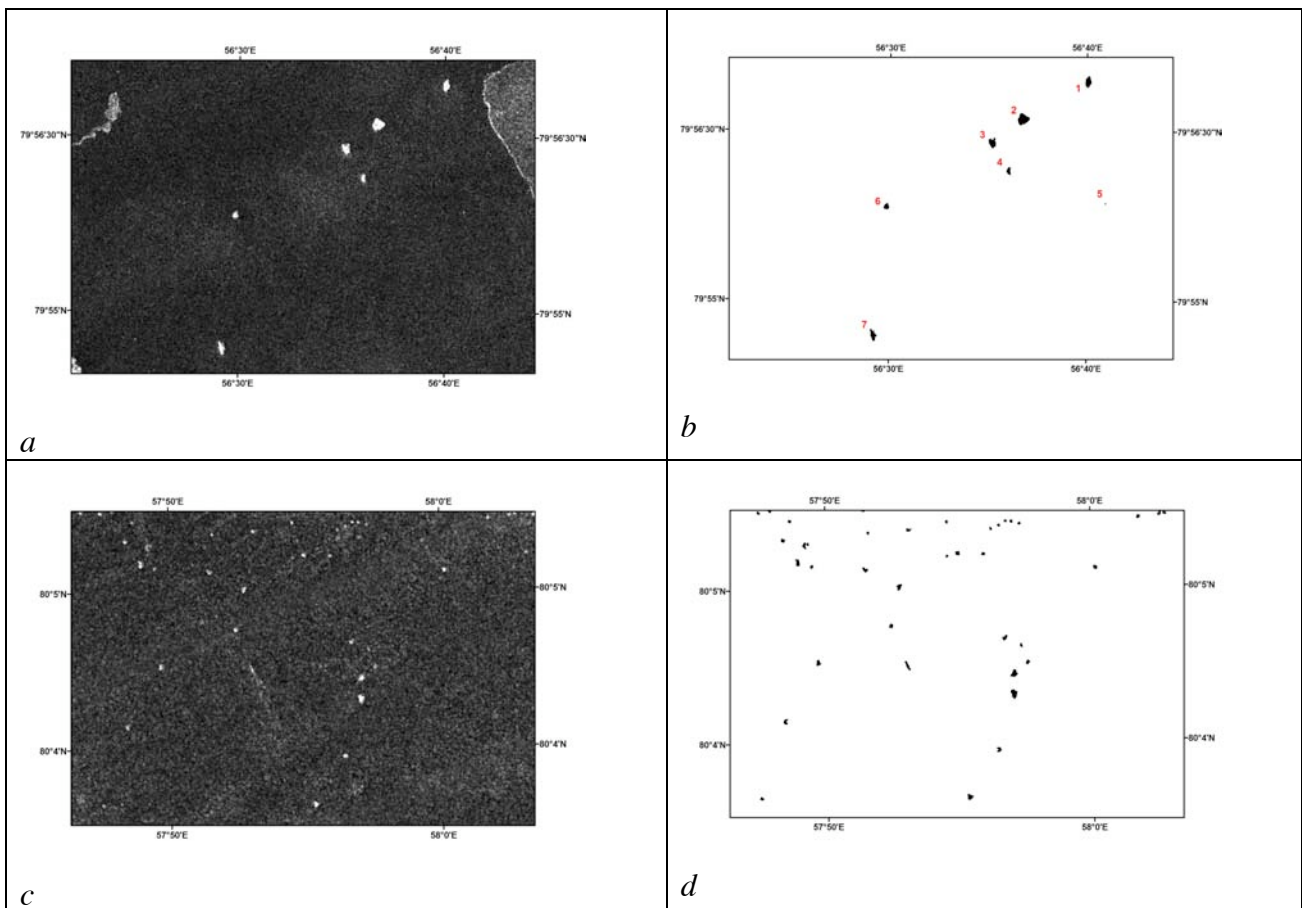


Figure 4-6. (a) Sub-image from open water with icebergs shown as bright spots against dark background. (b) Segmentation of (a) used to identify the icebergs. (c) Sub-image from fastice. (d) Segmentation of (c) to identify the icebergs. The icebergs in (b) were denoted with number and the characteristics are summarized in Table 4.2.

Table 4.2 Characteristics of the icebergs presented in figure 4.4., detected in Terra SAR-X image

Iceberg Number	Area (km ²)	MEAN pixel value (DN)	MAXIMUM (DN)	MINIMUM (DN)
1	0,0126	148,986	435	37
2	0,0242	130,673	354	23
3	0,0131	125,437	400	37
4	0,0058	114,850	230	48
5	0,0003	73,000	108	27
6	0,0061	92,528	154	44
7	0,0110	149,864	445	39

Comparison of SAR and optical images has been done for a number of small icebergs and growlers near the boundary of outlet glacier in Franz Josef Land (Fig. 4-7). Several icebergs are clearly evident in both the Landsat and Monitor-E optical images. Three bright spots, corresponding to icebergs, can be detected in the SAR image, which has a resolution of 75 m. The size of these icebergs were determined from 8-m resolution "Monitor-E" images, showing that no. 1 is 185 m, no. 2 is 130 m and no. 3 is 90 m. In area 4, there is a homogenous bright signature in the ASAR image and it is not possible to distinguish many icebergs located closely together. The optical images are better than SAR to resolve individual icebergs when the size is 100 m or less.

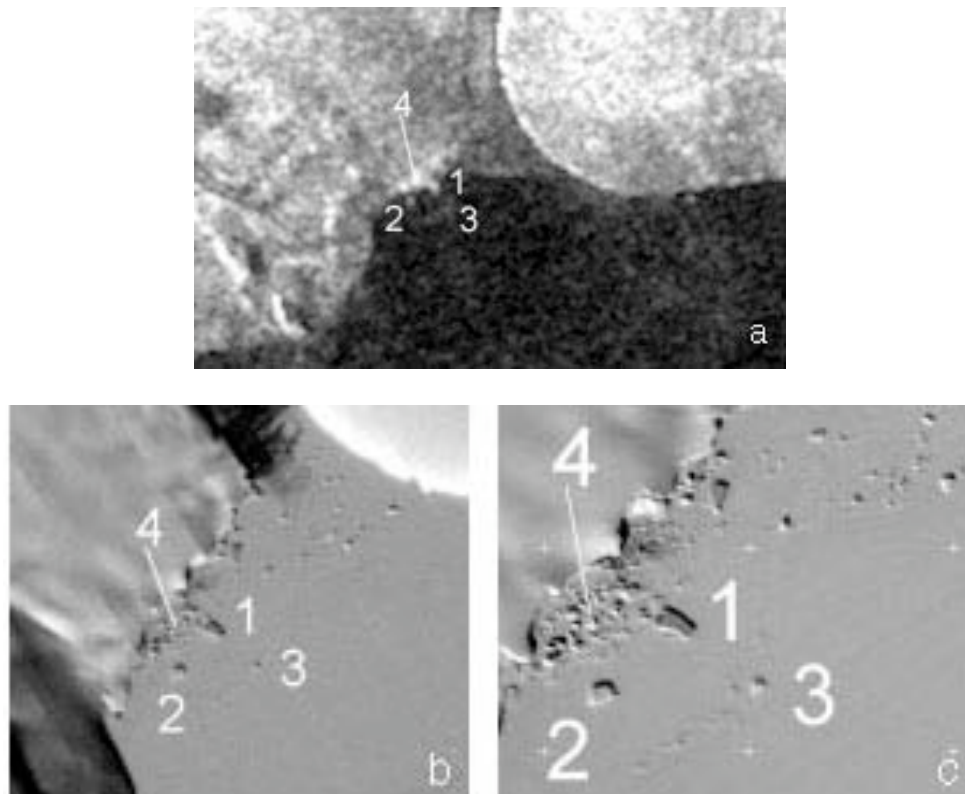


Figure 4-7. a) ENVISAT ASAR sub-image for April 5, 2006 of Franz Josef Land, b) Landsat sub-image for April 14, 2006 of the same area, c) "Monitor-E" sub-image for April 7, 2006 of the same area. Icebergs no. 1, 2 and 3 can be identified in all images, while the cluster of smaller icebergs in 4 appear as a homogeneous bright area in the SAR image.

Validation of SAR iceberg observation can be done both with high-resolution optical satellite images and by visual observations from helicopter or icebreakers. Fig. 4-8 a shows example of icebergs detected in drifting ice in a SAR image near Franz Josef Land, and Fig. 4-8b shows a photograph taken from a helicopter where the size of the detected icebergs can be estimated.

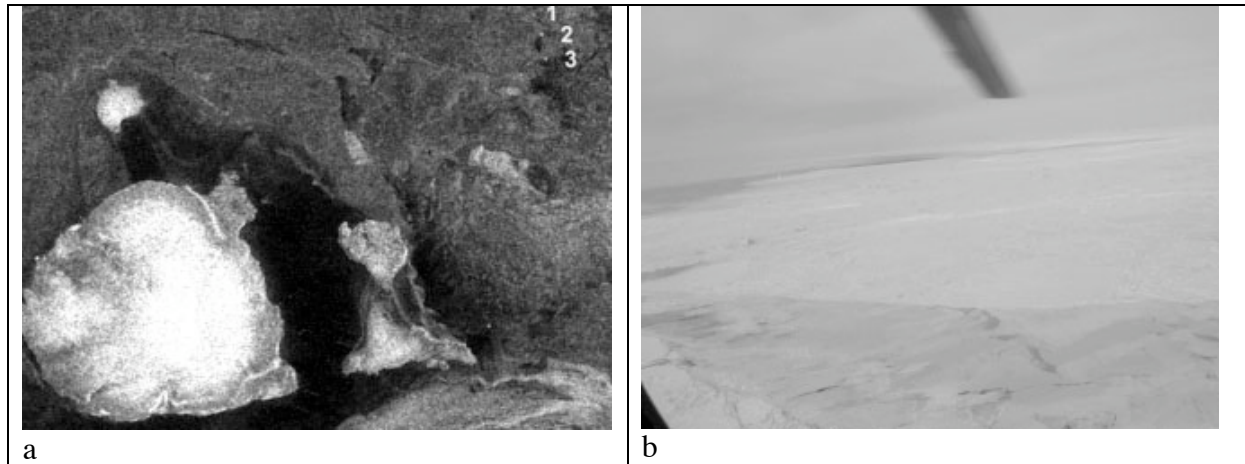


Figure 4-8. a) ENVISAT ASAR WS sub-image (March 31, 2006) of the area in Franz Josef Land. Three icebergs observed from a helicopter flight, which were detected in the SAR image, are marked by 1, 2, and 3. Their sizes are 100 x 250 m, 80 x 150 m, and 30 x 60 m (visual estimate); b) iceberg photograph taken from helicopter.

5. SEA ICE MONITORING IN THE CASPIAN SEA

The Caspian Sea is ice-covered in the northern part in the winter months, and this is an area where offshore development is going on. AGIPKCO is a major operator in this region and uses SAR data for sea ice monitoring. In MONRUK sea ice monitoring started in winter of 2007, and was continued in February-March of 2008. It is necessary to note, that dynamics of the ice cover development in the Northern Caspian Sea in 2007 and 2008 was completely different. Winter of 2007 in the northern Caspian Sea was abnormally warm, while winter of 2008 was abnormally cold. In early January of 2008 the northern Caspian Sea ice cover was formed completely.

This report described the sea ice analysis in February-March 2008 when 38 WS ASAR/ENVISAT images were downloaded from the NIERSC ftp-server via internet to NTsOMZ. In addition to SAR data, NTsOMZ used their MODIS and AVHRR data reception and archiving system to collect optical and IR images in the Caspian Sea. Near-real-time subsets from MODIS Rapid Response System were acquired for simple visual analysis. A set of maps, including sea surface and air temperature, currents, wind and sea ice cover maps were received via internet from Hydrometeorological Centre of Russia and SRC PLANETA sites. Air temperature data from Astrakhan meteo station were also used. The SAR images were analysed by interpreting the images directly and by using the SARTool software.

5.1 Interpretation of ENVISAT ASAR images

Visual interpretation of ENVISAT ASAR images by experts was done where characteristic ice types and ice concentration was annotated in the image. An example of such interpretation is presented in Figure 5-1.

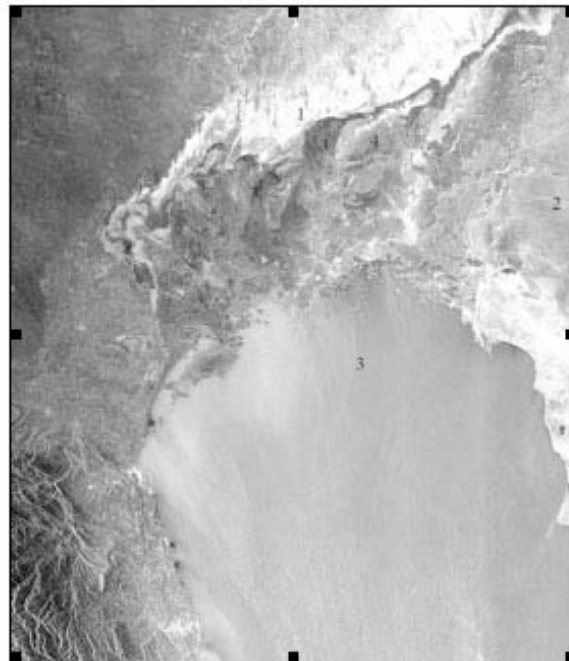


Figure 5.1. Interpretation of sea ice in an ASAR Wide Swath image of Northern Caspian Sea in February 2008: 1 – fast ice; 2 – sea ice concentration 10/10; 3 - sea surface; 4 - ice concentration 8-9/10.

A total of 8 images were interpreted and distributed to users as described in the monitoring and user interaction report (D33-2 and D5.2).

5.2 Detailed analysis of sea ice in the SAR image from 16 January 2006

A SAR image from 16 January 2006 covering the sea ice in the Northern Caspian Sea was analysed in detail and presented as an annotated ice map, as shown in Fig. 5-2.

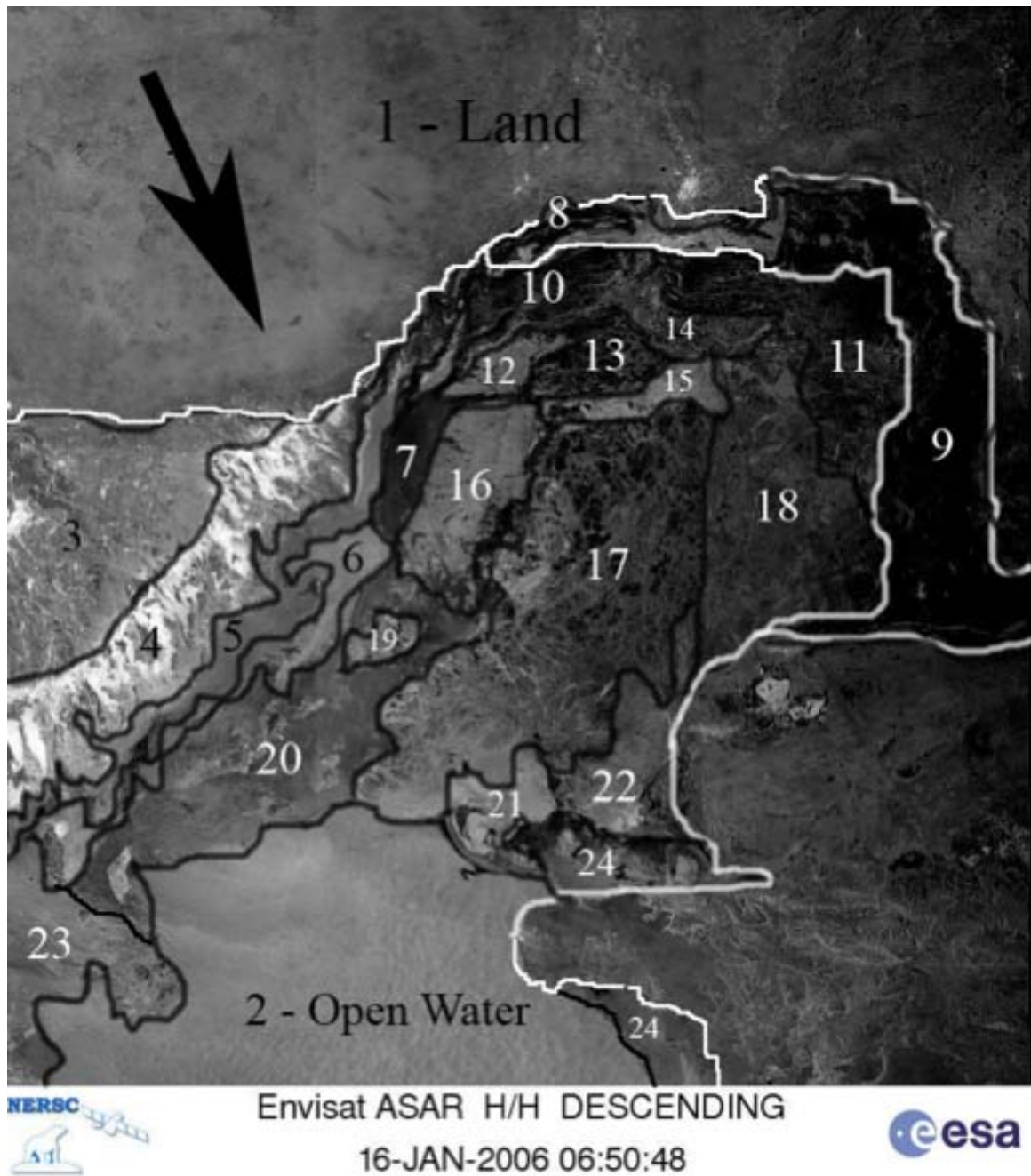


Figure 5-2. Annotated SAR image of sea ice in the Caspian Sea. The arrow shows the wind direction before the image was obtained.

The ice is divided into a number of polygons, each of which is characterized by specific ice conditions as described below.

Area 4: the central and eastern part of Volga seaside delta, covered by high aquatic plants, areas of fresh-water ice are formed in the shallow waters (bright white signal) with depths not exceeding 0,2-0,3m.

Areas 5, 6, 12, 16 and 19: a zone of fast ice, that was formed on re-freshened waters, different part of this zone are differed by roughness, snow coverage, as well by rafting, thickness of this ice is 15 cm and above (grey-white ice transient on thin white ice), three days earlier these areas corresponded to indivisible zones 10 – 12, that under influence of north-western winds were broken and divided initially on several zone, but then were moved toward eastern/north-eastern direction (boundaries of fracture of former united ice system 10 – 12 are corresponded their spatial heterogeneity, that was revealed from the ASAR image three days earlier

Area 7: a polynya, covered by dark nilas and slush (north-western winds in winter time in the Northern Caspian Sea be accomplished often by precipitation as wet snow and rain);

Area 8: primary fast ice, level, with little snow coverage, with insertion of hummocks and rafted zone, outer border is following along 1-2-m isobaths, thickness of fast ice - till 30 cm;

Area 9: a zone of steady fast ice along eastern (Kazakh) shores, different parts of this zone are differed by degree of hummocking and ground hummocking (stamukhas), new parts of rafted and ridged ice were formed around the outer border of this zone under influence of north-western wind;

Area 10: a zone thin white ice (7/10) with ridges and stamukhas, it was turned away from primary (basic) fast ice zone, on ASAR image in the gaps could be noticed new types of ice - nilas and slush;

Area 11: relatively level thin (9/10), new ridges and rafted ice could be disclosed in outermost NW and SE parts of this zone;

Areas 13 and 14 – ice breccia of thin white and grey-white ice, concentration of cristall white ice in zone 13 and 14, agreeably, 7/10 and 3/10, both area are situated in the shallow waters with depths 2 - 5 m, potentially threat formation here ridges and stamukhas is existed (ice breccia = ice of different stages of development frozen together)

Area 15: a polynya, covered by slush;

Area 17 and 18: ice breccia of thin white and grey-white ice, concentration white ice in zones, 4/10 and 6/10, both these zones has a fresh fractures covered by slush;

It is interesting to note that the SAR signatures in the Northern Caspian Sea shows many complicated features which are difficult to interpret, especially along the coast. For example, the backscatter in sub-images 9 and 10 shows areas of very shallow water in the estuary of Volga river. Ice analysis near the coast is very complicated in SAR images because the sea

level changes and the coastline is not well defined. It is useful to include other types of satellite data such as MODIS and Landsat, which can help to classify land from water (Fig. 5-3).

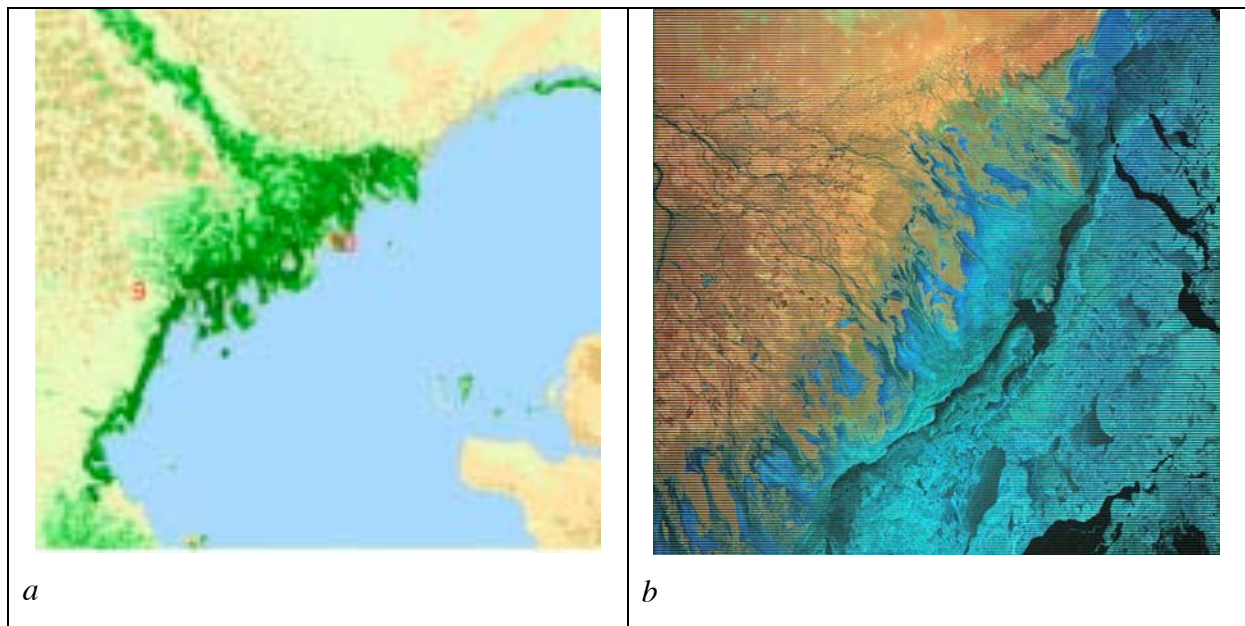


Figure 5-3 (a) MODIS/AQUA NDVI image fragment from 05 July 2007 showing the Volga river estuary; (b) Landsat quicklook image from 27 February 2008 showing sea ice in blue colour, open water in black and land areas in red-yellow. Both images illustrate the complicated coastline in the area.

5.3 Comparison of SAR images and sea ice concentration maps

Interpretation of 17 ASAR images was carried out for sea ice during the melting stage in 2008. Although the ASAR/ images started to lose contrast between ice and water signature, the open sea surface and an ice cover could still be discriminated quite well.

ASAR images were compared with sea ice concentration maps, based on SSM/I data from the Hydrometeorological Centre of Russia. It was shown, that during maximum ice cover development ice concentration maps represented the sea ice edge very well, as shown in Figure 5-4.

The difference between ice concentration values in the Arctic, obtained from passive and active microwave sensors are caused physically by melt ponds: passive microwave systems perceive melt ponds as open sea surface, while active microwave systems perceive melt ponds as sea ice [Comiso and Kwok, 1996; Belchansky and Platonov, 2002]. Synergy analysis of passive and active microwave data, thus, allow to carry out an estimation of melt ponds area and then to specify onset and end of melt. However *correct* passive microwave data processing algorithm should result only in relative ice concentration values decrease (In comparison with values received using active microwave systems). In principle, melt ponds can form on the Caspian Sea ice cover during periods, when temperature increases. Therefore, synergy of passive and active microwave data can be used also in analysis of sea ice conditions in the Caspian Sea.

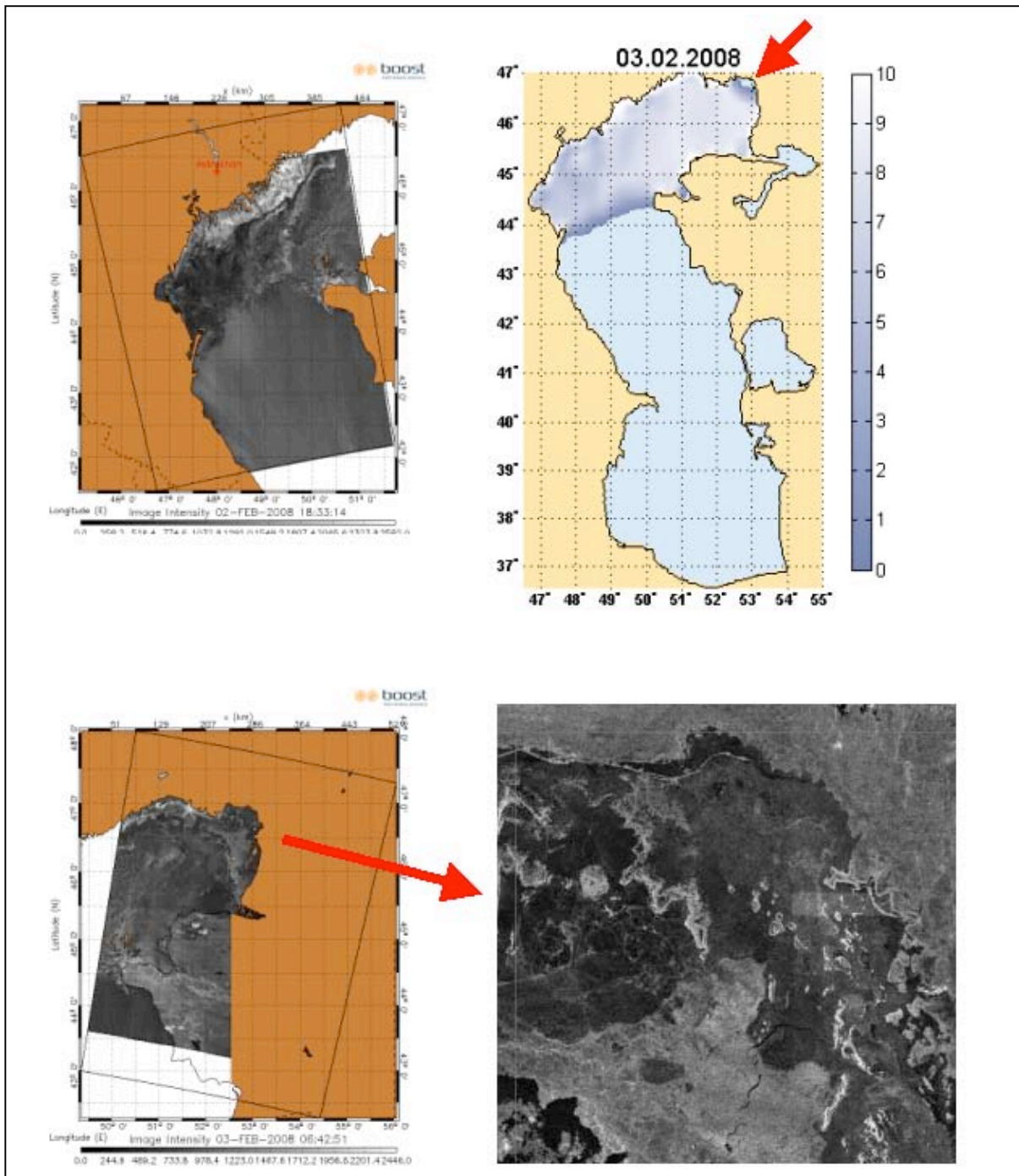


Figure 5.4. At the left above – WS ASAR/ENVISAT image from February 2, 2008. At the left below – WS ASAR/ENVISAT image from February, 3. At the right above - SSM/I sea ice concentration map, February, 3. At the right below - full resolution fragment of WS ASAR/ENVISAT image from February, 3.

6. SUMMARY AND CONCLUSIONS

The report gives presentation of images and analysis of SAR images for sea ice and icebergs in the Barents and Kara Sea area and in the Northern Caspian Sea. The work has included development of automatic techniques of SAR image interpretation, studies of polynya development from SAR images in the Kara Sea and Storfjorden, studies of icebergs detectability from SAR images as well as sea ice monitoring in the northern part of the Caspian Sea. All these studies are aimed at development and implementation of satellite SAR monitoring of the marine environment in Russia, Ukraine and Kazakhstan.

The scientific objectives are development and testing of algorithms for retrieval of sea ice parameters from SAR images, and their application for sea ice monitoring. One of the major sea ice parameters are ice type, ice concentration and ice drift. Significant part of work was devoted to creation of algorithms for retrieval of these ice parameters. In order to meet these objectives the algorithms of ice type identification and ice drift retrieval from successive SAR images were developed. Sea ice classification algorithms are based on neural network and Bayesian approaches. The retrieval of the multiyear ice partial concentration is made in interactive mode after classification. These algorithms were tested in the Central Arctic and show reasonable results. In order to use them in operative mode it is necessary to solve several problems. First, recalculation of sea ice backscatter to pre-defined incidence angle, need to be done. Such algorithm was elaborated and is described in this report. Future work will include its testing in SAR images of different ice types and producing accurate estimates of angular coefficients for various ice types. Elaborated algorithms of automated sea ice classification uses pixel-based approach. Better classification results can be obtained using region-based approach. Its implementation needs elaboration of reliable algorithms for image segmentation, which allows delineation of homogenous areas. Sea ice classification using image brightness and texture characteristics cannot provide results, which are accurate enough for using in operative mode. Significant improvement can be reached by using parameters of segment form in classification, a priori information about prevailing ice types and some other parameters. Ice drift retrieval algorithm is a modification of cross-correlation algorithm with restriction of search area. This algorithm was tested in Fram Strait and in the Barents Sea. Future work will include its testing in various sea ice conditions and improvement.

The *GMES objectives* are aimed at facilitating access to SAR and other satellite data for sea ice monitoring. Conducted studies revealed significant benefits of using SAR for sea ice monitoring in the Barents and Kara seas and in the Caspian Sea. It was clearly shown that the major sea ice parameters in these regions can be accurately and regularly identified, which is quite important for development of sea ice monitoring. Sea ice monitoring in the Caspian Sea, based on SAR and SSM/I data was implemented in 2007 and 2008. Studies of polynya development were conducted in Svalbard area and in the Kara Sea. It was found that the polynya parameters are accurately determined from SAR images. Monitoring of icebergs in the Barents Sea is an important problem, because they can significantly damage oil and gas platforms in the Arctic shelf. The results of iceberg detectability studies show that high-resolution SAR can be effectively used for this purpose, which is quite important for development of iceberg monitoring system. Service chains for SAR monitoring in the study areas were establish and tested. User-friendly system to access data and information about the sea ice conditions, based on web map server technology, was created and used in the project implementation. Users received information products and provided feedback to the consortium.

7. REFERENCES

- Belchansky G.I., Platonov N.G.* Evaluation and documenting of melt ponds and sea ice albedo according to satellite microwave measurements // *Earth remote sensing from space*. 2002. № 1. P. 51-66.
- Bishop C.M.* Neural networks for pattern recognition. Oxford: Clarendon Press, 1995, 482 p.
- Comiso J.C., Kwok R.* Surface and radiative characteristics of the summer Arctic sea ice cover from multisensor satellite observations // *J. Geoph. Res.* 1996. V. 101, № C12. P. 28397-28416.
- Drucker R., Martin S., and Moritz R.* Observations of ice thickness and frazil ice in the St. Lawrence island polynya from satellite imagery, upward looking sonar, and salinity/temperature moorings. *Journal of Geophysical Research*, 108, 2003.
- Fily M., Rothrock D.A.* Sea ice tracking by nested correlations // *IEEE Transaction on Geoscience and Remote Sensing*. 1987. № 25(5). P. 570-580.
- Johannessen, O. M., L. Bengtsson, M. W. Miles, S. I. Kuzmina, V. A. Semenov, G. Alekseev, V. F. Zakharov, A. P. Nagurnyi, L. P. Bobylev, K. Hasselmann and H. Cattle, 2004. Arctic climate change – observed and modeled temperature and sea ice. *Tellus* 56A 4, 328–341.
- Johannessen O. M., V. Yu Alexandrov, I. Ye. Frolov, S. Sandven, M. Miles, L. H. Pettersson, L. P. Bobylev, K. Kloster, V. G. Smirnov, E. U. Mironov and N. G. Babich. *Polar Seas Oceanography, Remote Sensing of Sea ice in the Northern Sea Route: Studies and Applications*. Praxis Springer, 2007, 472 pp.
- Sandven S., Dalen O., Lundhaug M., Kloster K., Alexandrov V.Y., Zaitsev L.V.* Sea Ice Investigations in the Laptev Sea Area in Late Summer using SAR data // *Canad. J. Remote Sensing*. 2001. № 26(5). P. 502-516.
- Sandven, S. Sea ice monitoring in European Arctic Seas using a multisensor approach. Chapter in the book “*Remote Sensing of the European Seas*” (Eds. Barale and Gade) *Springer Science and Business Media B. V.*, 2008, pp. 487 – 498.
- Yu Y. and Lindsay R.W.* Comparison of thin ice thickness distributions derived from Radarsat geophysical processor system and advance very high resolution radiometer data sets. *Journal of Geophysical Research*, 108, 2003.
- Zubakin, G. K., A. K. Naumov and I. V. Buzin. Estimates of ice and icebergs spreading in the Barents Sea. Paper no. 2004-JSC-381, 8 pp, 2004.